Doctoral Dissertation (Shinshu University)

Influence of sea level fluctuations on depositional environment during last 1000 years and characteristics of modern storm deposits in southwestern Ganges–Brahmaputra–Meghna delta, Bangladesh

バングラデシュ，ガンジス-ブラマプトラ-メグナデルタ南西部における最近1000年間の海水準変動の堆積環境への影響と近年の嵐による堆積物の特徴

HAQUE MD MASIDUL

Mountain and Environmental Science Division
Department of Science and Technology
Shinshu University

March 2022

A dissertation submitted to Graduate School of Medicine, Science and Technology, Department of Science and Technology, Shinshu University in partial fulfillment of the requirements for the degree of Doctor of Philosophy in Science

(Doctoral Program in Mountain and Environmental Science Division)

Influence of sea level fluctuations on depositional environment during last 1000 years and characteristics of modern storm deposits in southwestern Ganges–Brahmaputra–Meghna delta, Bangladesh

バングラデシュ，ガンジス-ブラマプトラ-メグナデルタ南西部における最近1000年間の海水準変動の堆積環境への影響と近年の嵐による堆積物の特徴

HAQUE MD MASIDUL

March 2022

Abstract

The impacts of the rising global temperature, compaction of thick sediments, as well as hazards associated with relative sea level (RSL) in the low elevated deltaic zone of Bengal Basin, make the region vulnerable to subsidence, coastal erosion, and storms. Hence, the projection of sea level and way of sediment supply are very important to understand the paleoenvironment and sedimentation process in this area. Long-term sea level change and information of global temperature cannot be obtained by using short instrumental records or direct observation. Therefore, the variation of geological evidence may provide valuable data that can be used to assess the depositional environment, sedimentation and coastal morphology for the southwestern Ganges–Brahmaputra–Meghna (GBM) delta of the Bengal Basin that was influenced by sea level change.

This dissertation interprets the result of the effect of RSL on the vertical and lateral variation of depositional environment in the late Holocene, the consequence of the recent trend of sea level rise and storms on coastal morphology and sedimentation, and characteristics of storm overwash deposits in the southwestern GBM delta of Bangladesh. This dissertation is structured in three parts as follows:

The first part deals with the analyses of sedimentary facies, geochemical proxies that include total organic carbon, total nitrogen and $\delta^{13}C$ values, and diatom assemblages of deposits to reconstruct paleoenvironments that were influenced by RSL over time. Samples of eight litho-sections collected from the upper and lower delta plain by using a gauge sampler were analyzed for this study. The lateral and vertical changes of depositional environments and radiocarbon age of selected samples provide the effect of sea level on the sedimentation process in the last 1000 years of Holocene. During 850−1300 AD, the sea level was higher than the present level where tide-influenced bioturbated mud was deposited at landward of the upper delta plain area. During 1300−1850 AD, the sea level started to drop, and organic rich bluish gray mud, mangrove peaty mud and terrestrial influenced yellowish gray mud were deposited successively at seaward of the lower delta plain area. The terrace was formed at landward due to lowering of the base level at the same time. After 1850 AD, the sea level started to rise which consequently created a new area of inundation and also increased sedimentation over the area. The sediment of terrestrial flood deposited over the erosional surface at landward and tidal sediment gradually onlap on it from seaward.

The second part of this dissertation presents the effect of recent trend of sea level rise, storm surge and sediment supply characteristics on coastal morphology and sedimentation along the southwestern GBM delta coast of Bangladesh. Satellite images for 43 years (1977–2020) and geological cores from the Haringhata coastal region were analyzed to explain the geological development of the area. The analyses of satellite images showed that the southern coastline lost its landmass permanently, consequently the eastern and western coastline advanced. The deeper part of the successions is composed mainly by mud and deposited in a marine influenced environment. The storm overwash silty sand overlies the mud. The coastal dynamics and sedimentation at the river mouth along the coast combined effects of increased marine influences due to sea level rise and decreased sediment supply from upstream. Rising sea level has influenced the change of the coastal morphology that shifted sediment accommodation space landward.

Characteristics, provenance, and depositional process of modern storm overwash deposits are examined in the third part that has been identified at the Kuakata coast of the GBM delta. Lithology, geochemical proxies, and diatom analyses were carried out to characterize the deposits. Three sedimentary units up to 70 cm thick have been identified within the successions. Massive or parallel laminated bluish gray mud that is deposited in a tide-influenced environment underlies the storm overwash deposits. Unimodal white to light gray sand unit found at the base of the storm deposits overlies the mud with sharp to erosional contact. The mean grain size and thickness of this sand unit decrease landward with increasing sorting value, where grain size distribution of sand is comparable with modern beach sand. The unimodal sand that dominated the base of the storm deposits grades into bimodal olive-gray sandy silt in the upper part of the storm overwash deposits. The grain size distribution implies that the sand was carried from the modern beach and the mud likely sourced from the suspended, nearshore deposits of the bay and the adjacent river. Storm overwash sand and sandy silt deposits contain both freshwater and marine-brackish diatoms. These sediments have likely been deposited by the storm surge from the bay and simultaneously overbank flooding due to heavy rainfall during cyclones. The low-lying GBM delta coast gets the influences of high-water levels from the bay and the adjacent river during the deposition of storm deposits.

Keywords: sedimentary facies, geochemical proxies, diatom assemblages, radiocarbon dating, satellite image, morphology, sediment supply, storm deposits, sea level, GBM delta.

Table of contents

List of figures

List of tables

List of publications

Published papers from the thesis

Research papers

- **Haque, M.M.** and Hoyanagi, K., 2021. Influences of sea level on depositional environment during the last 1000 years in the southwestern Bengal delta, Bangladesh., *The Holocene*, **Vol. 31(6)**, pp. 915−925.
- **Haque, M.M.**, Yamada, M. Uchiyama, S. and Hoyanagi, K., 2021. Depositional setup and characteristics of the storm deposit by the 2007 Cyclone Sidr on Kuakata Coast, Bangladesh., *Marine Geology*, **Vol. 442, 106652**.
- **Haque, M.M.**, Ghosh, M.K. and Hoyanagi, K., 2021. Coastal development in southwestern Bangladesh: understanding the interplay between storms and sea level rise., *Progress in Physical Geography*, Doi: 10.1177/03091333211046189 (online first).

Conference Papers

- **Haque, M.M.,** Yamada, M. and Hoyanagi, K. 2021. Depositional setup and characteristics of storm deposits following the 2007 Cyclone Sidr on Kuakata coast of Bangladesh, Annual meeting of Sedimentological Society of Japan (Online).
- **Haque, M.M.** and Hoyanagi, K. 2019. The elemental (TS, TOC, C/N) geochemistry of recent sediment of the southern Bangladesh for understanding the interaction between seawater and freshwater, 126th Academic Conference of the Geological Society of Japan, Yamaguchi, Japan.

Additional research papers

- **Haque, M.M.** and Roy, M.K., 2021. Geology and sedimentary environment of the Surma Group of rocks, Bandarban anticline, Bandarban, Bangladesh., *Journal of Nepal Geological Society*, **Vol. 62**, pp. 88−106.
- **Haque, M.M.** and Roy M. K. 2020. Sandstone-Shale Geochemistry of Miocene Surma Group in Bandarban Anticline, SE Bangladesh: Implications for Provenance, Weathering, and Tectonic Setting., *Earth Sciences*. **Vol. 9** (1), pp. 38−51.

CHAPTER 1

Introduction

Climate change and fluctuation of sea level have influenced the depositional environment and sedimentation process in the low elevated coastal zone of the world. The complex hydrodynamic and geomorphic settings controlled the coastline dynamics and depositional environment. Shifting of the coastline is an indicator of marine and terrestrial influences. The changes are well preserved in sediments of low elevated coastal areas. The instrumental records of sea level are well-documented for the last 2−3 centuries. So, geological evidence serves as an important archive for assessing the dynamics of sea level and climate change throughout the Earth's history. This provides a better understanding of changes in the depositional environment due to fluctuation of sea level, which could be helpful to understand the future delta development process in the area.

The Ganges-Brahmaputra-Meghna (GBM) rivers coalescing in the Bengal Basin and form one of the world's largest delta systems with numerous sub deltas. The delta is situated mainly in Bangladesh and partially in West Bengal of India, covering approximately 1×10^5 km^2 of low elevated deltaic flood plain that have around 380 km long delta front (Figure 1.1; Allison, 1998; Mukherjee et al., 2009; Umitsu, 1993). The delta surface is susceptible to both the long-term natural (tectonic subsidence or upliftment, compaction of sediment, and sedimentation) and anthropogenic activities (drainage, embankment construction, and sediment extraction), which lead to fluctuation of relative sea level (Auerbach et al., 2015; Brown and Nicholls, 2015; Grall et al., 2018; Hanebuth et al., 2013; Hoque and Alam, 1997; Syvitski et al., 2009). The sea level influences sedimentation (depending on the fluvial sediment supply rate and ability of delta to keep that sediment) and delta development processes that, in turn, affect coastal morphology (Darby et al., 2016; Dunn et al., 2018; Stvitski and Kettner, 2011). The net erosion of the southwestern delta coast is of ~170 km^2 in the last 37 years (1973–2010) due to sea level rise, insufficient sediment delivery and coastal erosion during storm surges; and an average annual erosion could be up to 20 mm/year (1989–2009) particularly during extreme events (Figure 1.1; Allison, 1998; Brown and Nicholls, 2015; Rahman et al., 2011).

The coastal area of the GBM delta was formed during the last 11,000 years and has since prograded as a series of clinoforms in the Bay of Bengal (Kuehl et al., 2005; Mikhailov and Dotsenko, 2007). The delta was built by sediment discharge from the GBM river system. Clay mineral composition and radiocarbon evidence reveal that the southwestern delta was formed by sediments carried by the Ganges River system (Allison and Kepple, 2001; Heroy et al., 2003) (Figure 1.1). The GBM delta coast is affected by wind, waves, and storms such as tropical cyclones, although the Sundarbans mangrove forest significantly mitigates these effects (Food and Agriculture Organization [FAO], 2007) (Figure 1.1). Susceptibility of the deltaic environment to physical change also depends on upstream water and sediment discharge, and recirculation of these sediment within the delta system (Rahman et al., 2018). Shifting of the coastline is, therefore, an indicator of marine and terrestrial influences and the sedimentary records of these changes are well preserved, particularly in the low elevation coastal areas.

The dissertation is aimed to interpret the change of depositional environment and its relation with sea level change in the low-lying southwestern GBM delta during the late Holocene. It also helps to understand the effect of present sea level rise and fluvial influences on the delta development processes and characterize the modern storm overwash deposits over the area.

1.1. Regional geology and geomorphology

Bangladesh has two entirely different tectonic settings: to the north lies the stable platform that comprises the foothills and alluvial fan of the Himalaya, and to the south is the Bengal Basin of the Indian Ocean (Figures 1.2−1.3). The Bengal Basin is bounded by Precambrian Shillong or Meghalaya plateau and Garo Hills to the north, Rajmohal Hills and the Chhotanagpur Plateau of Indian craton to the west, Neogene sediment of Chittagong-Tripura Fold Belt (CTFB) to the east, and the Bay of Bengal to the South (Acharyya, 2007; Bandyopadhyay, 2019; Hossain et al., 2019; Mukherjee et al., 2009) (Figures 1.2−1.3).

The collision of Indian and Eurasian plates at ~55–52 Ma resulted the formation of the Himalaya during ~27–17 Ma. From the present geographical point of view, the uplifted Himalaya and Paleogene Indo-Burmese Range of Trans Himalaya provide the major sedimentary sources in the Bengal Basin. The GBM river systems drain and carries the eroded sediments and deposit mainly in this basin. Bengal Basin's sediments have been compressed and uplifted after an oblique collision between Indian and Burmese plates during ~14–04 Ma that resulted from Indo-Burmese Range and formed the present configuration of the basin (Beck et al., 1995, Najman et al., 1997, 2012; Roy and Chatterjee, 2015).

The GBM delta of Bengal Basin lies in front of the Himalaya foredeep where deltaic sediment has been protruding since the Miocene from a northeast-trending hinge line (Figure 1.2; Goodbred Jr. and Kuehl, 2000b). The GBM river system carries sediment from different parts of the Himalaya, Trans Himalaya and the upper part of the basin formed one of the largest delta systems. Present-day the GBM river systems deliver more than 1×10^9 ton/year of sediment through the estuary, where 30% accumulates in the subaerial delta, and the rest is discharged through the estuary of submarine delta and Bengal Fan (Goodbred Jr. and Kuehl, 1999; Kuehl et al., 2005; Mouyen et al., 2018; Rahman et al., 2018). The GBM delta is bordered by uplands on all three sides and has a 125 km wide passage that is linked to its northern provenance. The modern evolution of the GBM delta started during the Last Glacial Maximum (~18 ka) when the sea level was around 120 m lower than today and sedimentation has developed in five successive transgression phases during the Holocene (Allison et al., 2003; Grall et al., 2018; Islam and Tooley, 1999, Umitsu, 1993). The Holocene strata having thickness ranges from 10–45 m in the southwestern GBM delta are composed mainly muddy sand and mud facies. These facies have been classified by different lithology and organic matter contained in sediment, which represents the defined depositional environments of the area (Goodbred Jr. and Kuehl, 1999, 2000a, 2000b; Umitsu, 1993). Tectonically, the study area falls in the eastern side of the Bengal Foredeep (Figure 1.2; Alam, 1996; Alam et al., 1990, 2003; Uddin and Lundberg,

1999); and tectonic activities, particularly in the area is the main sources of subsidence in the delta plain with geological time rather than the compaction (Goodbred Jr. and Kuehl, 2000a; Hoque and Alam, 1997). The area is subsiding due to its position at the eastern edge of the northeastward drifting of the Indian Plate as described by Steckler et al., 2008, and the sediments that are carrying from uplifted Himalaya deposited in the subsiding delta basin of the area (Curray, 1994).

The GBM delta of the Bengal Basin is situated mainly in Bangladesh and partially in West Bengal of India. The surface elevation of the Bengal Basin is mostly less than 25 m above of mean sea level but the elevation is higher and ranges between 25 m to 60 m at Pleistocene Barind and Madhupur tract, and Holocene alluvial fans in the Himalaya foot plain (Figure 1.3). The elevation reached up to 1000 m at the CTFB of the Indo-Burmese range in the eastern part of the Bengal Basin. The surface gradient of the basin roughly decreased from northwest to southeast. The elevation of the eastern GBM delta is less than 15 m, with a minimum of below 1 m in the south and southwest of the delta (Bandyopadhyay, 2019; Mukherjee et al., 2009). The subaerial and subaqueous parts of the Bengal Basin's integral depositional system extend from the southern Himalaya to the far reaches of the Bay of Bengal (Curray, 2014). The GBM delta components include a higher-gradient vertically and laterally migrating sand-dominated braid belts fan delta, a lower-gradient comparatively stable fluvio-tidal channels section in the southeast, and a fluvially abandoned tidal section in the southwest. Southwest GBM tidal delta is accreting vertically but declining irreversibly in certain sections (Wilson and Goodbred Jr., 2015) (Figure 1.3). The area has undergone massive changes due to the dynamic process of accretion and erosion of land along the coast. The study area is part of the tidally active southwestern GBM delta plain, and it has a complex network of tidal rivers, their tributaries, and mangrove vegetated islands (Islam, 2001; Islam and Gnauck, 2008).

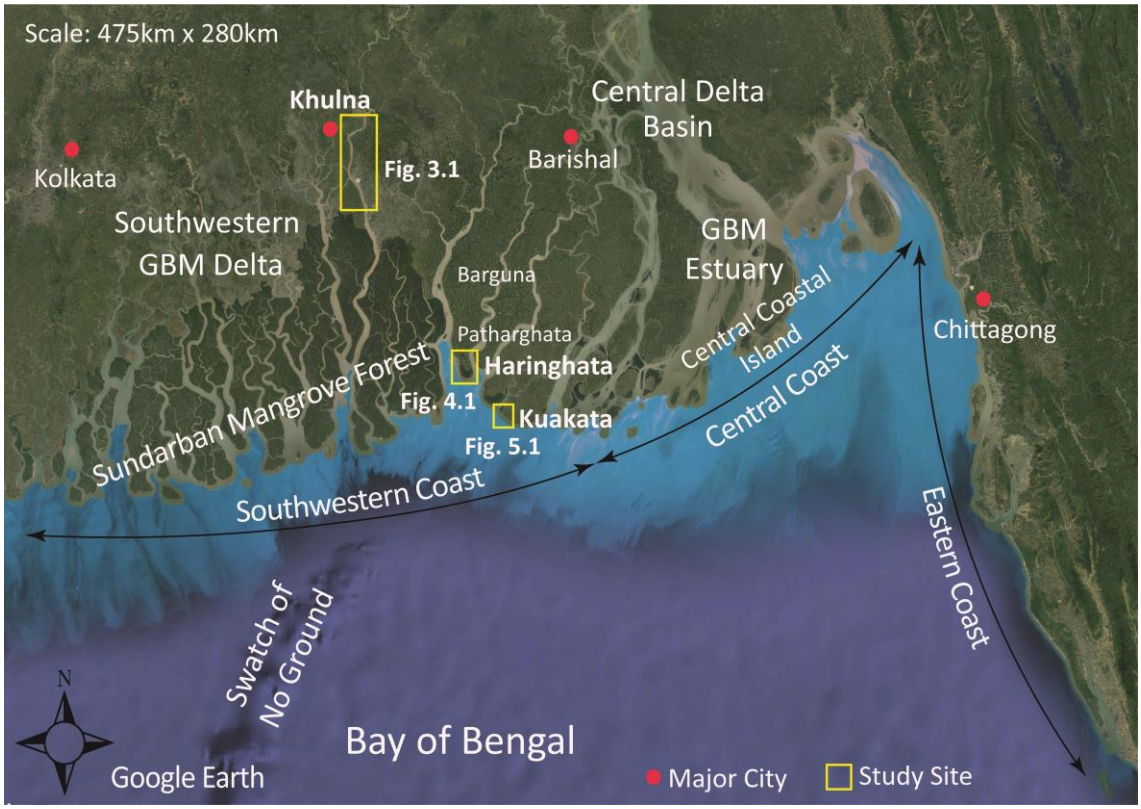

Figure 1.1: Satellite image (Google Earth) of southwestern delta basin (India and Bangladesh) with location of the study sites (modified from Haque and Hoyanagi, 2021, Haque et al., 2021a, 2021b).

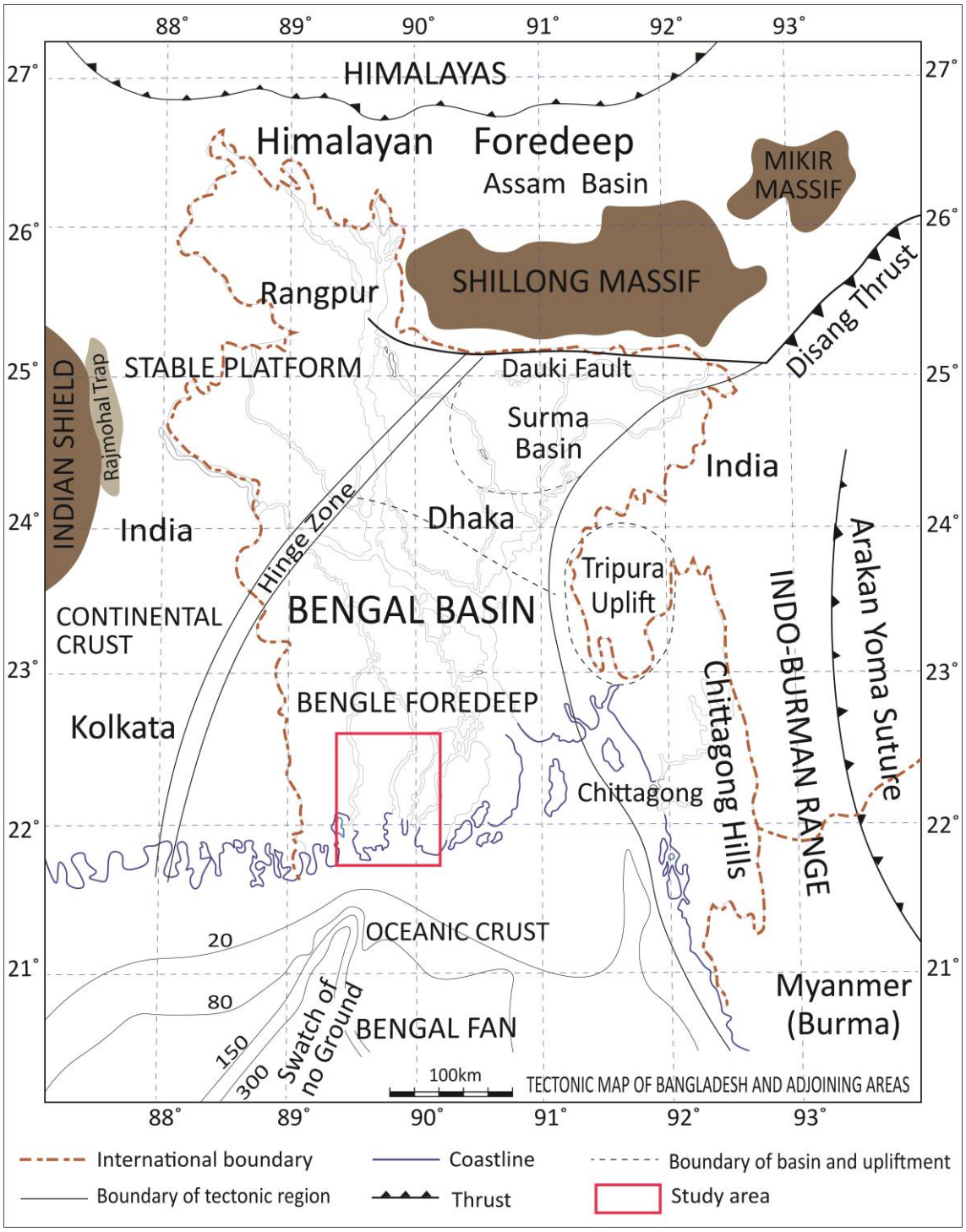

Figure 1.2: Tectonic settings of Bangladesh and its surrounding area showing study area (modified from Alam et al., 1990, 2003; Haque et al., 2021b, Uddin and Lundberg, 1999).

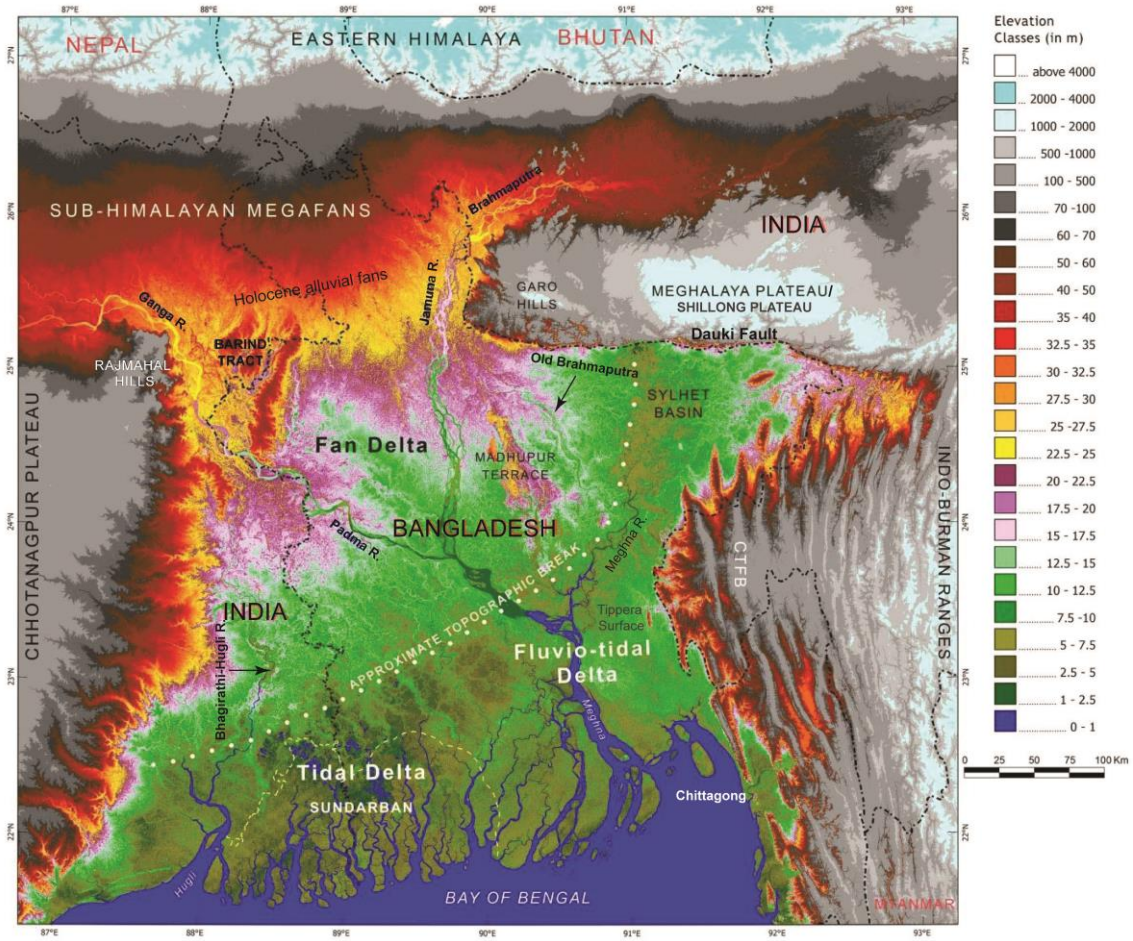

Figure 1.3: Geomorphic map of the Bengal Basin and surrounding areas showing some of the important physiographic units of the basin (SRTM-90 m digital elevation model) (modified from Bandyopadhyay, 2019).

1.2. Climate and cyclone activity

Bangladesh is characterized as a subtropical climate region in the central north and tropical in the south. Bangladesh's southern coast is influenced both by tides and major cyclones with disastrous storm surges (Ali, 1996; Karim and Mimura, 2008; Kudrass et al., 1998). The country has a 710 km long coastline along the Bay of Bengal (Figure 1.4; Ministry of Water Resources [MoWR], 2005). The climates of Bangladesh are divided into the northeast wind or Winter Monsoon from December to February, summer or Pre-Monsoon from March to May, southwest wind or Monsoon from June to September, and Autumn or Post-Monsoon from October and November. Since the study area is facing towards the Bay of Bengal, it receives seasonal monsoonal wind from the southwest Bay of Bengal that causes heavy rainfall from June to September and the northeasterly monsoon causes low rainfall from November to February (Chaturvedi and Sanjay, 2015; Kay et al., 2018). Landsea (2013) described that tropical cyclones usually form if the temperature of the sea surface reaches up to 26.5˚C and is characterized by low pressure, high wind, and precipitation. The Bay of Bengal is favorable to cyclogenesis. The cyclones that form in the Bay of Bengal move northward and northeastward and strike Bangladesh mostly during the Pre-Monsoon (March to May) and Post-Monsoon seasons (October and November) (Figure 1.4; Balaguru et al., 2014; Karim and Mimura, 2008; Kudrass et al., 2018). According to Gray (1985), Hossain et al. (2010), and Knapp et al. (2010), about 14% of tropical cyclones formed in the Bay of Bengal hit the Bangladesh coast, or 1.4% of all tropical cyclones generated in the world. Every year the Bay of Bengal coast faces five to six tropical cyclones, of which two generally reach the severe stage with high and intense precipitation (Singh, 2007).

Figure 1.4: Bathymetry and overview of the Bay of Bengal.

1.3. Background of study

The earliest important works on the Ganges-Brahmaputra river and its delta systems were introduced by Rennel (1809), Fergusson (1863), La Touche (1910), and Bagchi (1944). In 1959, for the very first time, Morgan and McIntire described the physiography and structure modification of Quaternary sediment of Bengal Basin in complete form. Coleman (1969), Rudra (1981), Sesoren (1984) discussed the sedimentation process and landform along the Brahmaputra river and ancient river mouth of Ganga. Umitsu (1985, 1987, 1993) used satellite images and 300 columnar borehole sections to describe the late Quaternary landform evolution and sedimentation of the GBM delta system. Since the 1990s, a large number of research results have been published by many authors on the depositional process (e g., Goodbred Jr. and Kuehl, 1998, 2000a, 2000b; Islam et al., 1999), causes of change in sedimentation and delta formation processes (e g., Allison, 1998; Kuehl et al., 2005; Mikhailov and Dotsenko, 2007; Pickering et al., 2018; Sarkar et al., 2009), and stratigraphy (e g., Allison et al., 2003; Chamberlain et al., 2017; Lindsay et al., 1991) of GBM delta. Goodbred Jr. and Kuehl (2000b) and Allison et al. (2003) have given five-time phases in lateral growth of lower delta plain during the Holocene. The lateral changes of the area is associated with the Ganges and Brahmaputra rivers and the combined flow of the GBM river. The southwestern part of Bangladesh's delta basin is developed through receiving sediment from the Gorai river, tributaries of the Ganga. Presently, the central delta system of the area is progressively formed by the fluvial and marine influences in the GBM river system (Figure 1.1). The sediments from the GBM estuary has significantly contributed sedimentation process at the southwestern lower delta plain of the Bengal Basin (e g., Allison and Kepple, 2001; Goodbred Jr. et al., 2014; Rahman et al., 2018; Sarkar et al., 2009; Wilson and Goodbred Jr., 2016). Holocene channel avulsion (Bristow, 1999; Pickering et al., 2014; Sincavage et al., 2017), subsidence (Alam, 1996; Grall et al., 2018; Hanebuth et al., 2013; Higgins et al., 2014; Karpytchev et al., 2018; Krien et al., 2019), and sea level change (Brammer, 2014; Pethick and Orford, 2013) significantly contributed to the development process of the area.

The geographic position of the GBM delta makes this area vulnerable to sea level rise and climate change. The delta surface is sensitive to both the natural and anthropogenic activities that influenced RSL and coastal morphology (Auerbach et al., 2015; Brown and Nicholls, 2015; Grall et al., 2018). The coastal areas have a high concentration of people but this area is highly vulnerable to subsidence, coastal erosion, and storm surge (Brammer, 2014; Nicholls et al., 2016). Additionally, understanding the change of depositional environment and coastal morphology is very important to recognize the impact of sea level and sediment supply in the low elevated deltaic zone. It would represent the development process of the area. Characterizing the recent storm deposits along the GBM delta coast is also important to identify the paleo-records of cyclone-borne sediments and tsunami deposits in the future study. Despite the availability of a great number of studies, there still are significant knowledge gaps in assessing the influence of sea level and sediment supply on the depositional process, coastal morphology, and characterization of storm deposits in the low-lying southwestern GBM delta of the Bengal Basin. Considering the geomorphology and elevation, the study area is suitable to interpret the terrestrial and marine influences on the depositional environment during the late Holocene. The research also helps to understand the effect of present sea level rise and storms on coastal development and analyze the storm overwash deposits to compare with modern overwash deposits on the global scale.

Satellite images, sedimentary facies, geochemical proxies [total organic carbon (TOC), total nitrogen (TN), stable carbon isotope ratio ($\delta^{13}C$ values)], diatom assemblages, and radiocarbon (^{14}C) dating of the sediments have been considered in this study. These analyses identify the depositional environment, sources of organic matter in deposits, illustrate the coastal dynamics and sedimentation process of the study area. The changes of depositional environment and sedimentation process have also been represented the effect of RSL change of the area. Satellite images, field observations, geological core analyses, and literature review provide an exact picture of the interplay between sea level rise and storms on the coastal development in the low-lying delta coast of the Bengal Basin.

This dissertation consists of the following three separate parts with a minor overlap of common headings. The first part (Chapter 3) deals with the reconstruction of sea level that influenced the depositional environment in the southwestern GBM delta of Bangladesh. Sedimentary facies, geochemical proxies, diatom assemblages, and radiocarbon age have been used to understand the lateral and vertical variation of the sedimentation processes with fluctuation of sea level over time. Chapter 3 represents the changes in the depositional environment and its relation with sea level during the last 1000 years at the upper and lower southwestern GBM delta of Bangladesh. The relative movement of the sea level is also compared on a global scale in this part.

The fluvial and marine influences on the GBM delta play an important role in coastal morphology. In the second part (Chapter 4), satellite images and geological cores analyses have been considered to explain the possible causes involved morphological change and sedimentation process in the southwestern delta coast. The effect of the recent trend of sea level rise during the last 50 years and sediment supply characteristics have influenced coastal development. The interplay between the storms and sea level rise on coastal development have been understood in Chapter 4.

The third part (Chapter 5) examines the characteristics, provenance, and depositional process of the modern storm deposits (2007 Cyclone Sidr) that have been identified on the southern coast of Bangladesh. The modern storm deposits of the southwestern GBM delta give distinctive characters that has been explained in Chapter 5. It will also help to characterize the storm overwash deposits and compare them to modern overwash deposits on a global scale.

Chapter 6 consists of a synthesis of the above chapters which gives an idea about the effect of rising sea level and sediment supply on coastal development in the southwestern GBM delta Bangladesh. It also helps to understand the sedimentation process and its relation with sea level in the low elevated GBM delta during the late Holocene and near future.

CHAPTER 2

Methodology

Geomorphology, surface elevation, and field accessibility have been considered to get suitable locations for this study. Three study locations at southwestern delta were selected to describe the late Holocene sea level change (Khulna region), the effect of present sea level on coastal development (Haringhata), and characterization the storm overwash deposits (Kuakata) (Figure 1.1). The methodologies were applied for the study are as follows.

2.1. Field investigation

A detailed lithofacies have been carried out during sample collection from three study sites (Figure 1.1). A handheld GPS (GARMIN, eTrex Touch 35J) was used to record the sampling point of the study. The samples were collected from the outcrop, using a gouge sampler and A 1 m long handy geo-slicer for laboratory analyses. The altitudes of every sampling site were measured by leveling, based on the reference datums situated near the study site.

2.2. Laboratory analyses

2.2.1. Grain size analysis

The laser diffraction grain size analyser of LS 13 320 (Beckman Coulter Co., Ltd.) at Shinshu University was used for grain size analysis of collected samples after treated with 10% hydrogen peroxide (H_2O_2) solution to remove the organic carbon (Haque and Hoyanagi, 2021; Switzer, 2013; Switzer and Pile, 2015). The machine can determine the grain size ranges between 0.04 μm and 2000 μm. The method of Folk and Ward (1957) graphical measured was used to calculate the grain sorting (φ) of these samples (Blott and Pye, 2011).

2.2.2. Geochemical analyses

Geochemical proxies including the ratio of total organic carbon and total nitrogen (TOC/TN) and stable carbon isotope ratio ($\delta^{13}C$ value) have been used to recognize the sources

of organic matter of the sediment. TOC/TN of the terrestrial sediment is above 15 and the marine sediment is 3−10 (Meyers, 1997; Watson and Whitefield, 1985), whereas the $\delta^{13}C$ values of terrestrial sediment range between −25‰ and −28‰ and marine sediment range between −18‰ and −22‰ (Denies, 1980; Jasper and Gagosian 1990; Prasad et al., 2017; Ray and Shahraki, 2016; Sarkar et al., 2009). For geochemical analyses, the samples were taken in a glass bottle (the weight of the samples was less than 1 gram) and treated with 1 N HCl to remove inorganic carbon. These bottled samples were then warmed on a hot plate (temperature in between 50–60˚C) for 14 days and distilled water was poured into them so that these samples were not completely dry on it. These prepared samples had been used for the analysis of TOC and TN by using the Flash 2000 (Thermo Fisher Scientific Co., Ltd.). A standard of antipyrine was used (C: 70.19%; N: 14.88%) and the analytical prerecession was ±0.03%. $\delta^{13}C$ analysis had been carried out using an elemental analyzer (Flash EA1122, Thermo Fisher Scientific Co., Ltd.) and a mass spectrometer (Delta V Advantage, Thermo Fisher Scientific Co., Ltd.) at the laboratory of the Faculty of Science of Shinshu University. A few milligrams of prepared samples were taken in tin capsule and heated to 1000˚C in the furnace of the elemental analyzer, and the resulting purified CO_2 and N_2 gas were fed directly into the mass spectrometer using the pure helium carrier gas. The results of $\delta^{13}C$ value were expressed as per mil (‰) relative to the Vienna Peedee Belemnite (V–PDB) standard. It has been measured against working standard (Atropine; $\delta^{13}C = -20.8$ ‰) with every eight samples and the precision was ±0.15 ‰ for $\delta^{13}C$.

2.2.3. Diatom analysis

The sediment samples of study sites were used for diatom analysis. These samples were taken (appx. 1gm) into 200 ml beakers with 30 ml of 30% H_2O_2 and warmed on the hot plate (temperature ~80–90˚C) for 15–20 minutes until the release of all effervescence. 20 to 30 ml of 10% HCl was added to the residue. The samples were warmed on the hot plate again and flooded with distilled water. The acid was removed by a top-up test tube with distilled water and centrifuged for 4 minutes at 1700 rpm (at least 3 times). Clay mineral was dispersed and

removed by using 0.01 N sodium pyrophosphate solution for 5 hours (at least 4 times). Sodium pyrophosphate was then removed by using a centrifuge (4 minutes; 1700 rpm at least 3 times). The slides were prepared on 18×18 mm cover glass and mounted in Pleurax on a glass slide. The diatoms were identified from the slide using a 1000x magnification Olympus Microscope and diatom identifications were referred to Krammer (2000, 2002, 2003), Lange-Bertolt (2000, 2001), Levkov (2009), and Patrick and Reimer (1966, 1975). According to Round et al. (1990), and Jones (2007), diatom assemblages are represented as a percentage of the total count of diatoms and their ecological groups, namely freshwater, brackish and marine habitat.

2.2.4. Radiocarbon dating

Radiocarbon age of selected samples collected from the Khulna district considered for this study (Figure 1.1). The ^{14}C age determination had been carried out on shell, peat, wood, and seed fragments using Accelerator Mass Spectrometer (AMS) at the Institute of Accelerator Analysis Ltd. at Fukushima, Japan. The ^{14}C age of shell and wood of same sampling core at depth 93 cm below the surface has been calculated to understand the reservoir effect on the sampling area. The samples show modern in their age and reflected no reservoir effect to measure the radiocarbon age at the study site. Umitsu (1993) measured the ^{14}C age of wood and shell fragment (*Neritiolae neritina*; a tidal environment in the mangrove zone) at depth 34 m and 35 m of the Dewlatpur sedimentary core of Khulna in the upper delta plain in his study and showed the age of 8890±150 year BP and 8910±150 year BP, respectively. The same type of shell species has been considered to determine the ^{14}C age of the study. For that, the reservoir effect is not considered to the calibration of ^{14}C age of shell collected from Dhigholia of the study. Umitsu (1993), Stanley and Hait (2000), and Allison and Kepple (2001) were not considered reservoir effects and/or not calibrated to measure the age of shell samples collected from the GBM delta plain area of their study. The ^{14}C age was converted into a calibrated calendar age with an error of 2σ using *OxCal v4.3* with the *IntCal13* database (Bronk Ramsey, 2009; Reimer et al., 2013).

2.3. Identification of coastal dynamics from satellite data

Satellite images from four time periods were utilized to evaluate transformations along the Haringhata coast (Figure 1.1): Landsat Multispectral Scanner (MSS) (57 m spatial resolution) obtained in February 1977, Landsat Thematic Mapper (TM) (28.5 m spatial resolution) obtained in February 1989, Enhanced Thematic Mapper (ETM) (28.5 m spatial resolution) obtained in February 2000 and Operational Land Imager (OLI) (30 m spatial resolution) acquired in February 2020.

The images were pre-processed in reference to well known remote sensing Landsat data procedure (Unger Holtz, 2007), including radiometric and atmospheric correction, co-enrollment, and resampling. The dark-object subtraction technique was utilized over the images to eliminate atmospheric effects caused by clouds, dust, smoke, etc. (Chavez, 1996), as part of the radiometric corrections. The sun azimuth and sun elevation data, which were extracted from the image header files, were utilized to complete the radiometric correction process. Following Chander and Markham (2003), all images were changed to top-of-atmosphere reflectance from digital numbers to allow comparison between images.

Relative radiometric standardization (Coppin et al., 2004; Ghosh et al., 2015; Langat et al., 2019; Mas, 1999) was likewise completed to standardize the differences arising from the sun illumination and atmospheric conditions. All images were geo-rectified using 47 ground control points (GCPs). This procedure brought about a root mean square error (RMSE) of 0.002812 pixels. Afterward, the images were resampled to a 30 m pixel size utilizing the nearest neighbor resampling technique.

Two distinct methodologies were applied to recognize the coastline and identify changes: 1) land and water interface separation for coastline identification utilizing a water index algorithm; and 2) coastline digitization for mapping erosion/accretion patterns along the Haringhata coast. Several indices derived from satellite data for detecting water surfaces have been developed. Sensitivity of the green band to variances of turbid water and sediment make it very useful for discerning wide-ranging classes of vegetation while different portions of the

infrared band strongly contrast land and water features. The Modified Normalized Difference Water Index (MNDWI) algorithm, that has been extensively utilized for land-water interface separation (Ghosh et al., 2015; Langat et al., 2019; Ma et al., 2007; Rokni et al., 2014; Sunder et al., 2017), was adopted to recognize changes of the coastline. MNDWI was assessed for TM and ETM images of 1989 and 2000 as (Green–MIR)/(Green+MIR), where Green and MIR are the appearances in the green and mid-infrared bands of these images, while for the OLI image of 2020 MNDWI was estimated as (Green–SWIR1)/(Green+SWIR1), where Green and SWIR1 are the appearances in the green and short wave infrared bands of the OLI image. Normalized Difference Water Index (NDWI) derived from Green and Near-infrared (NIR) bands was also used for land-water interface separation. This index was applied over the 1977 MSS image as this image had only four bands and there was no option to apply the MNDWI index over this particular image. NDWI was estimated for the MSS image of 1977 as (Green–NIR)/(Green+NIR). A Boolean approach was then applied to the NDWI and MNDWI images to produce land and water classes. To extract the coastline layers, on-screen digitization of the coastline was executed. Thereafter, coastline layers were overlaid to examine the coastline position at each date. Coastline positions were highlighted to explain coastal advancement/retreat, as well as erosion/accretion prone areas and the coastline changes were calculated. Ideally, comparisons throughout extended periods of time should be made at the same tide level for the best correctness. However, data management is limited by its availability throughout such extended periods (in this case 1977–2020). Satellite passes occur at fixed times and cannot be adjusted for each capture to ensure tidal consistency. These are the source of errors in conducting this kind of research related to the use of recorded data. Dry season (December to February) and low-tide images were preferentially used in this study to minimize tidal impacts because tidal fluctuations are lower during dry seasons (Figure 2.1). It was also expected that the variations in the water level during low tides were little contrasted with the level of the coastline shifts. Furthermore, it was ensured that the image acquisition date did not correspond with neap or spring tides. These measures can significantly improve precision and are standard methods in remote sensing work.

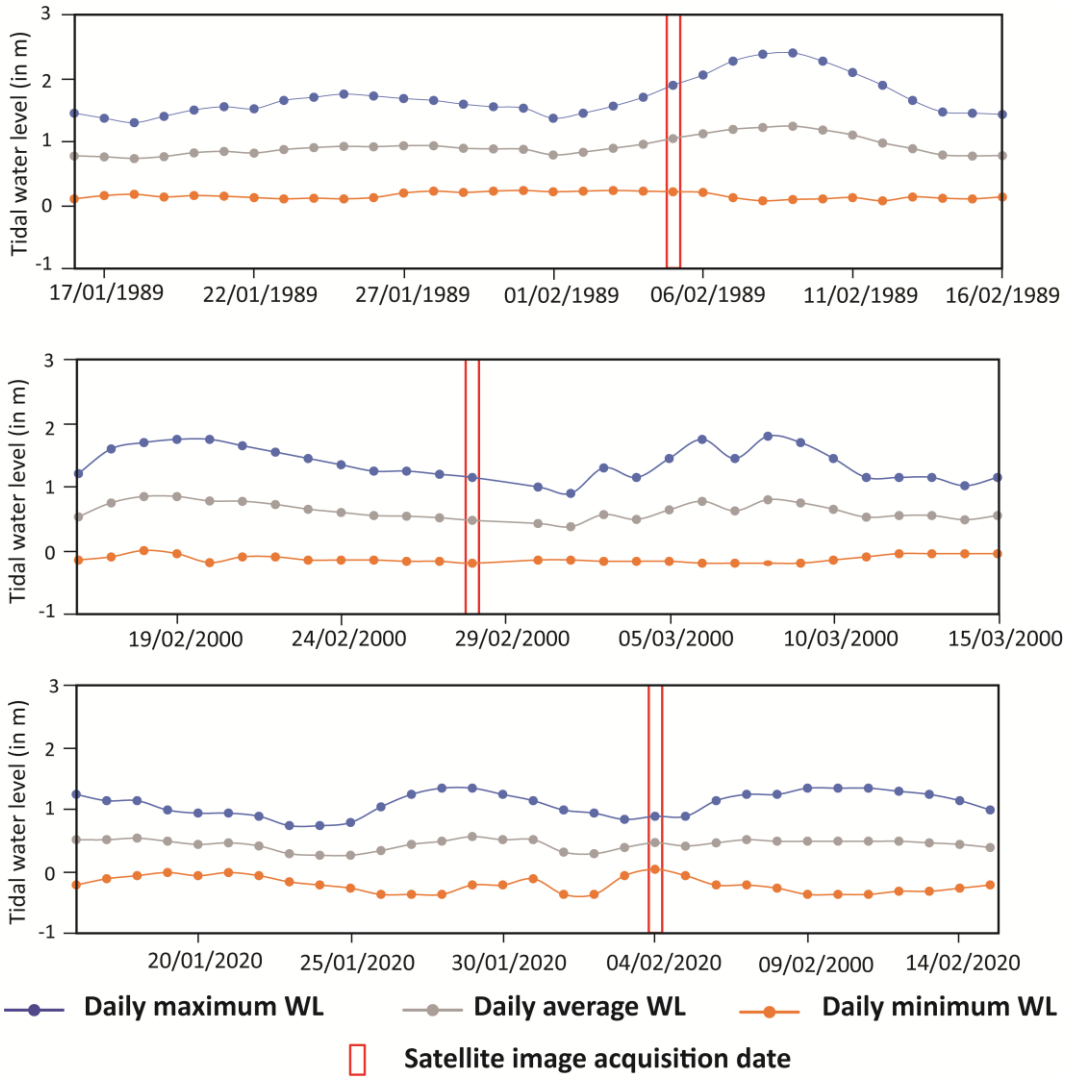

Figure 2.1: Daily tidal water level at Patharghata during the period of satellite image acquisitions (data sources: Bangladesh Water Development Board).

To validate the NDWI and MNDWI methods, the 1976 topographical map was used for the 1977 image, the Local Government Engineering Department (LGED) maps of 1989 and 2000 were used for the images of 1989 and 2000, respectively, and high-resolution Google Earth™ images from 2020 were used for the image of 2020 as reference data. On-screen digitizations were performed to extract the "true" boundaries between land and water from all reference data and afterward, compared with the NDWI and MNDWI generated coastline layers. To estimate the accuracy of the land/water classification for all maps, an accuracy assessment method described by Congalton and co-authors was used (Congalton, 1991; Congalton and Green, 2019; Congalton et al., 1983). The entire image processing and analysis procedure was carried out using ENVI (5.1, Esri, Colorado, CO, USA) and ArcGIS (10.2, Esri, Colorado, CO, USA) software.

CHAPTER 3

Change in depositional environment and its relations with sea level during late Holocene

This chapter has been modified from the published article titled 'Influences of sea level on depositional environment during the last 1000 years in the southwestern Bengal delta, Bangladesh' in *The Holocene* (2021, Vol. 31 (6), pp. 915–925).

3.1. Introduction

Large river deltas and their adjacent ocean margins have provided a significant terrestrial-aquatic interface, where rivers transfer and discharge a huge amount of particulate and dissolve materials from terrestrial sources to the oceans (Milliman and Farnsworth, 2013). Variation of the organic matter composition in sediment is strongly influenced by river discharge and inflow of seawater. The geochemical transformation of organic matter and diatom assemblages enable to recognize the changes in the coastal depositional environment (Gao et al., 1012; Prasad et al., 2010, 2017; Ray and Shaharaki, 2016; Ray et al., 2015).

Many authors have discussed the development and classification of the GBM delta landform, timings and development phases of the Brahmaputra-Ganges River systems as well as GBM delta (Akter et al., 2016; Chamberlain et al., 2017; Goodbred Jr. and Kuehl, 1999, 2000a, 2000b; Goodbred Jr. et al., 2003, 2014; Islam and Tooley, 1999; Pickering et al., 2018; Sarkar et al., 2009; Umitsu, 1993; Wilson and Neidhardt et al., 2013). Umitsu (1993), Allison (1998), Goodbred Jr. and Kuehl (2000b), Allison et al. (2003), and Goodbred Jr. et al. (2014) reported that the main channels of the Ganges River started draining the western part of the basin from 3050 BC and that result continues to develop the present-day configuration of delta around 1550 to 1050 BC (Figure 1.1). The fluctuation of sea level has been recorded in the last 1000 years of the Holocene (Grinsted et al., 2010; Mann et al., 2009; Nunn et al., 1998; Ota et al., 1990), and the depositional process of the low-lying deltaic plain is highly influenced by the relative sea level (RSL). Several kinds of indicators can be used to reconstruct the paleoenvironment and the Holocene sea level change, but geochemical analyses of organic matter of sediments are considered to illustrate the effect of the RSL change on the depositional process. Considering the geomorphology and altitude, the study area is suitable to interpret the terrestrial and marine influences on the depositional environment in the late Holocene. Here, the sediments were collected along the N-S direction of the Rupsa-Pasur river (Figure 3.1) and analyzed accordingly which could help to provide a better understanding of the vertical and lateral changes in the depositional features that reflect different environments in relation to interpret the effect of RSL of the region.

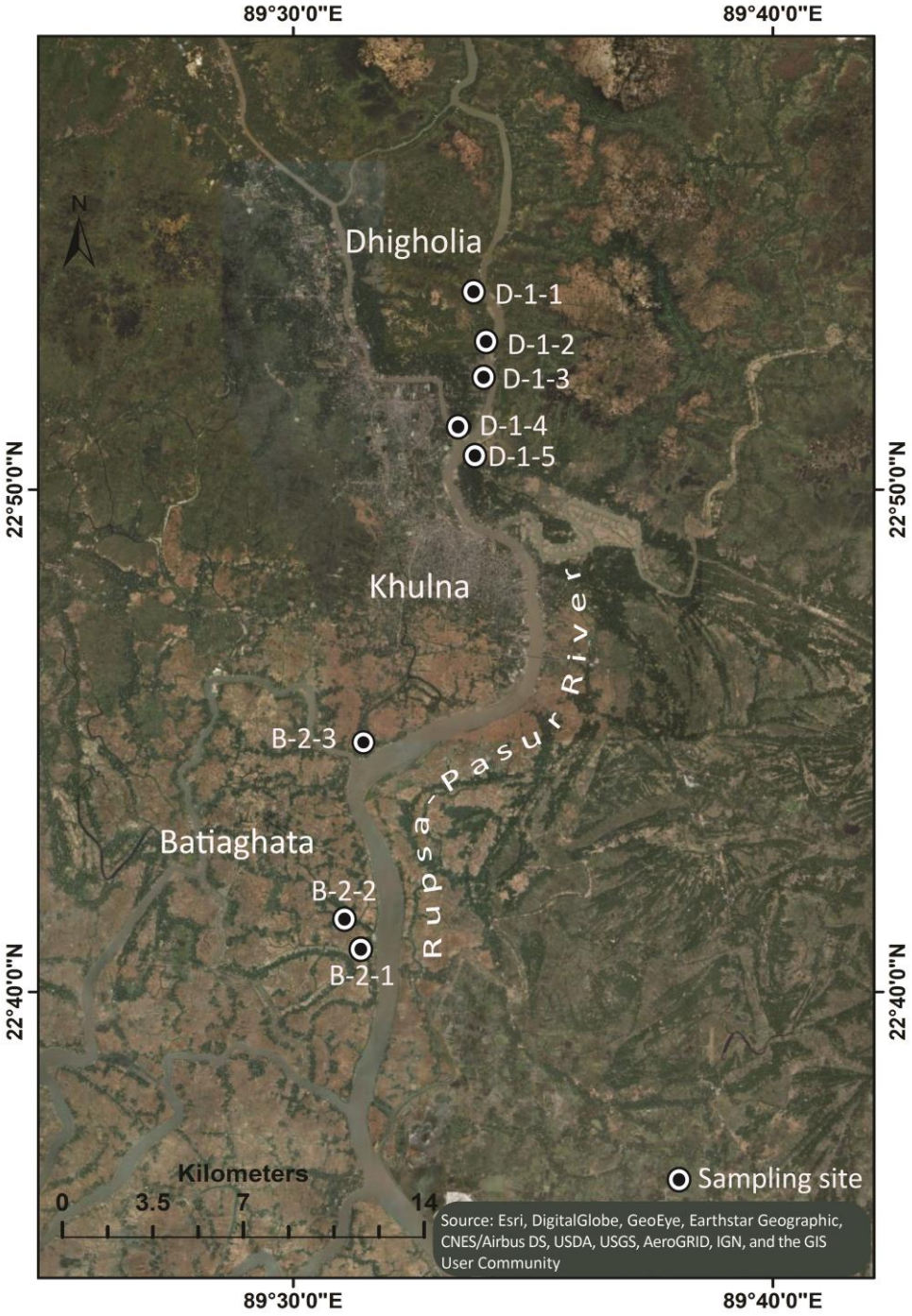

Figure 3.1: Location map of the study area shows the sampling sites at Dhigholia and Batiaghata of Khulna district (see Figure 1.1, Page 6 site location) (modified after Haque and Hoyanagi, 2021).

A detailed lithofacies have been carried out during sample collection from two locations along with N-S direction – Dhigholia (landward in upper delta plain) and Batiaghata (seaward in lower delta plain) of Khulna district, Bangladesh (Figures 1.1 and 3.1). The procedure of laboratory analyses of collected samples has been described in Chapter 2. The analyses of sedimentary facies, geochemical proxies, diatom assemblages, and radiocarbon (^{14}C) age of the sediments have been carried out to gain a better understanding of changes in the sedimentary environment (lateral and vertical) due to fluctuation of sea level during the last 1000 years, which could be helpful to understand the future delta development process in the area.

3.2. Sedimentary facies and depositional environment

Based on the lithology, grain size distribution, sedimentary structure, and composition of sediment, five sedimentary facies were identified in the sections (Figures 3.2−3.3). Sedimentary facies with geochemical proxies and diatom assemblages have been used to characterize the origin of organic matter and describe the depositional environment of the study area (Bouillon et al., 2003; Breithaupt et al., 2014; Graham et. al., 2001; Kristensen et. al., 2008; Lamb et. al., 2006; Meyers, 1994, 1997; Omura and Hoyanagi, 2004; Omura et al., 2006; Prasad and Ramanathan, 2009; Saintilan et al., 2013). The TOC/TN vs $\delta^{13}C$ values diagram has been used to identify the sources of organic matter in sediments (Figure 3.5; Blair and Carter, 1991; Hoefs, 2009; Lamb, 2006; Marchand et al., 2005; Sarkar et al., 2009). Diatom assemblages help to distinguish the ecology of the environment during the deposition of the sediments (Jones, 2007; Round et al., 1990). The description and depositional environment of sedimentary facies are followed.

3.2.1. Facies A (bioturbated light yellow to gray mud)

Light yellow to gray mud is found in the lower part at Dhigholia and upper part at Batiaghata successions (Figure 3.2). Parallel to wavy laminated gray to pale-yellow fine-grained sand with shell fragments and burrows have been found in these mud layers. The TOC,

TOC/TN, and $\delta^{13}C$ values of the sediments are 0.16–0.91%, 7.16–11.4, and −18.09– −22.31‰ respectively (Figure 3.2). The brackish to marine diatom species are abundant in these facies (Figure 3.4).

Interpretation: Facies A is composed of mainly mud containing significant traces of the burrows and shell fragments with parallel to wavy laminated fine-grained sand that reflects the signature of a tidal flat or tidal influenced environment (Daidu, 2013). TOC/TN and $\delta^{13}C$ value indicate a marine-influenced sedimentary source (Deines, 1980; Jasper and Gagosian 1990; Meyers, 1997; Prasad et al., 2017; Ray and Shahraki, 2016; Sarkar et al., 2009; Watson and Whitefield, 1985). The plotting of TOC/TN and $\delta^{13}C$ values indicates that the marine/tidal water column has a major contribution of organic matter of the facies (Figure 3.5). Diatom assemblages suggest a strong tidal influence during the deposition of the sediments of Facies A (Figure 3.4).

3.2.2. Facies B (bluish gray mud)

The lower part of the sedimentary successions of B-2-2 and B-2-3 at Batiaghata are composed of the facies (Figure 3.2). Bluish gray carbonaceous rich mud laminated with parallel and cross-laminated white to grayish-white colored silty sand (Figure 3.2). The TOC, TOC/TN, and $\delta^{13}C$ values of the sediment range from 2.20–5.31%, 12.63–13.91, and −22.72– −22.31‰, respectively (Figure 3.2). The brackish diatom species are significantly found in the facies (Figure 3.4b).

Interpretation: The bluish gray mud facies containing very fine parallel to cross sand laminae and grain size can be interpreted as a low energy environment. The TOC/TN and $\delta^{13}C$ values indicate a transitional brackish environment where brackish water habitat diatom species are found in the deposits of the facies. The facies contain a high concentration of organic mud with plants or root traces and have parallel and cross silty sand laminae which indicate a lower delta mud plain environment (Howa and Stanley, 1991; Rossi et al., 2019).

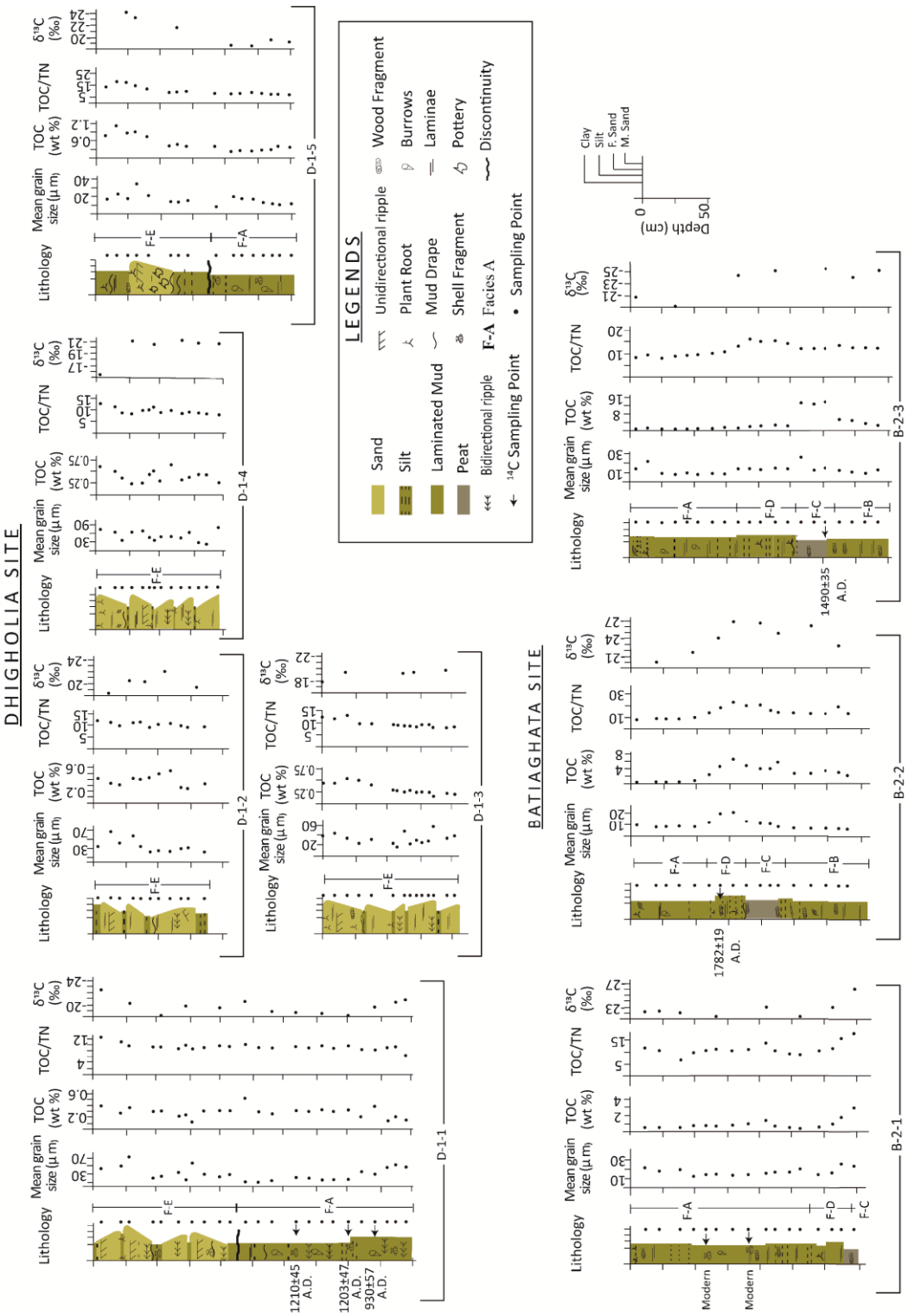

Figure 3.2: Vertical distribution of lithology, mean grain size, TOC, TOC/TN, and $\delta^{13}C$ values in the sedimentary successions of Dhigholia and Batiaghata. The position of sampling sites shown in Figure 3.1, Page 25 (Haque and Hoyanagi, 2021).

3.2.3. Facies C (dark gray to black peat with peaty mud)

The dark gray to black peat facies are documented in the B-2-3 (130–155 cm), B-2-2 (83–108 cm) successions at Batiaghata, and peaty mud is found over the peat layer and in the bottom of the B-2-1 (165–170 cm). Highly carbonaceous organic-rich dark gray to black peaty mud containing wood and plant fragments, and interbedded with silty sand has been found over the peat layer. The facies are containing a large quantity of organic matter (TOC up to 13.39%). The TOC/TN of these facies zones reach up to 23.11, and the $\delta^{13}C$ value is −26.83‰ (Figure 3.2). Brackish to freshwater habitat diatoms are dominantly found in the facies (Figure 3.4b).

Interpretations: The peat layer was formed under brackish to freshwater swamp environment and deposited during the regression of the sea (Mukherjee, 1972; Rashid et al., 2013). It is observed that the $\delta^{13}C$ value and TOC/TN of the peat layer are more comparable with the value of the sediments of the mangrove forest of Sundarbans (Prasad and Ramathan, 2009; Rajan et al., 2011; Ray et al., 2015; Sarkar et al., 2009) and also comparable with a global range of mangrove of the coastal areas (He et al., 2010; Hoefs, 2009; Gonneea et al., 2004; Ray and Shahraki, 2016; Thimdee et al., 2003). The TOC/TN vs. $\delta^{13}C$ value shows that terrestrial influenced C_3 plants are the dominant source of organic matter in this sedimentary Facies C (Figure 3.5). The lithology, geochemical analyses, and diatom assemblages indicate that the mangrove organic matter sources during the deposition of the sediments.

3.2.4. Facies D (yellowish-gray mud)

Yellowish-gray mud is observed over the peaty mud at Batiaghata successions (Figure 3.2). Parallel to wavy laminated olive-gray to pale yellow fine sand with rootlets, and plant fragments have been found in these layers. The facies contain organic matter (TOC ~2%), TOC/TN is above 15 and $\delta^{13}C$ value is below −25‰ (Figure 3.2). Freshwater habitat diatom species are observed in the facies (Figure 3.4b).

Interpretation: Existence of rootles and high concentration of TOC, TOC/TN, and lower value of $\delta^{13}C$ value indicate a terrestrial influenced environment and the TOC/TN vs. $\delta^{13}C$ value diagram shown that C_3 plants are the dominant source of organic matter in the facies (Figure 3.5). Diatoms analysis represents the increase of freshwater influences during deposits of sediments.

3.2.5. Facies E (laminated silty sand)

The facies is underlined by an erosional surface that lies over the upper part of tidal influenced Facies A at Dhigholia (Figure 3.2). Parallel to wavy laminated medium to fine-grained sand is overlaid by 2–8 cm thick mud layer common at the Dhigholia (Figure 3.3a). Bidirectional to unidirectional ripples, horizontal laminated light gray to pale yellow silty sand has alteration with thinly laminated olive black mud. The mud contains root trace and shell fragments. A depositional sequence over the 20 to 65 cm thick with pottery noted in the upper part of the D-1-5 sampling site at Dhigholia, has laminated silty sand facies with ill-sorted medium to fine-grained sand with abundant rootlet (Figures 3.2 and 3.3b). The successions were exposed due to riverbank erosion and shown coarsening upward medium to fine-grained sand over the sampling point of the pottery.

The TOC/TN is low (8–10) in the lower part of the facies and the value gradually increases in the upper part; and shown higher (up to 17.97) at D-1-5 succession (Figure 3.2). The average $\delta^{13}C$ values are relatively low in these successions (−22.55‰ at D-1-1 and −24.18‰ at D-1-5) whereas higher values are observed in the topmost part of D-1-2, D-1-3, and D-1-4 sedimentary successions (Figure 3.2). A total of 12 species of diatoms are identified in the facies that represent the freshwater habitat diatoms abundance in the facies as shown in figure 3.4a.

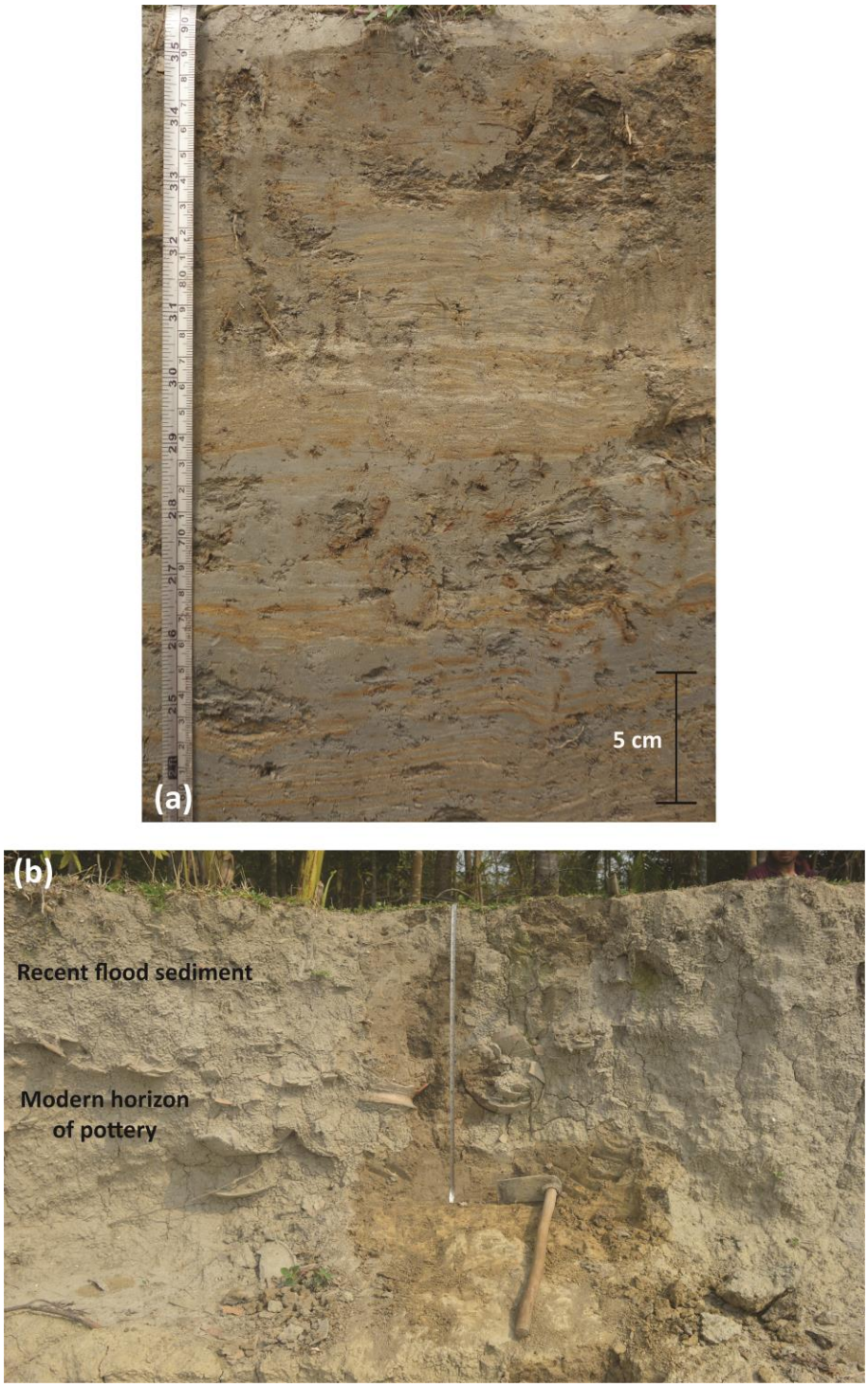

Figure 3.3: (a) Immature soil horizon overlain by coarsening upward sequence of fine to medium grained sandstone with erosional contact at D-1-2 sampling site indicating flood deposit; **(b)** Massive to coarsening upward sequence of fine-grained sediment overlain a pottery sequence at D-1-5 sampling site indicating a major flood event deposit (possible flood event of 1998) in the sampling area at Dhigholia (length of steel tape is 80 cm) (modified after Haque and Hoyanagi, 2021).

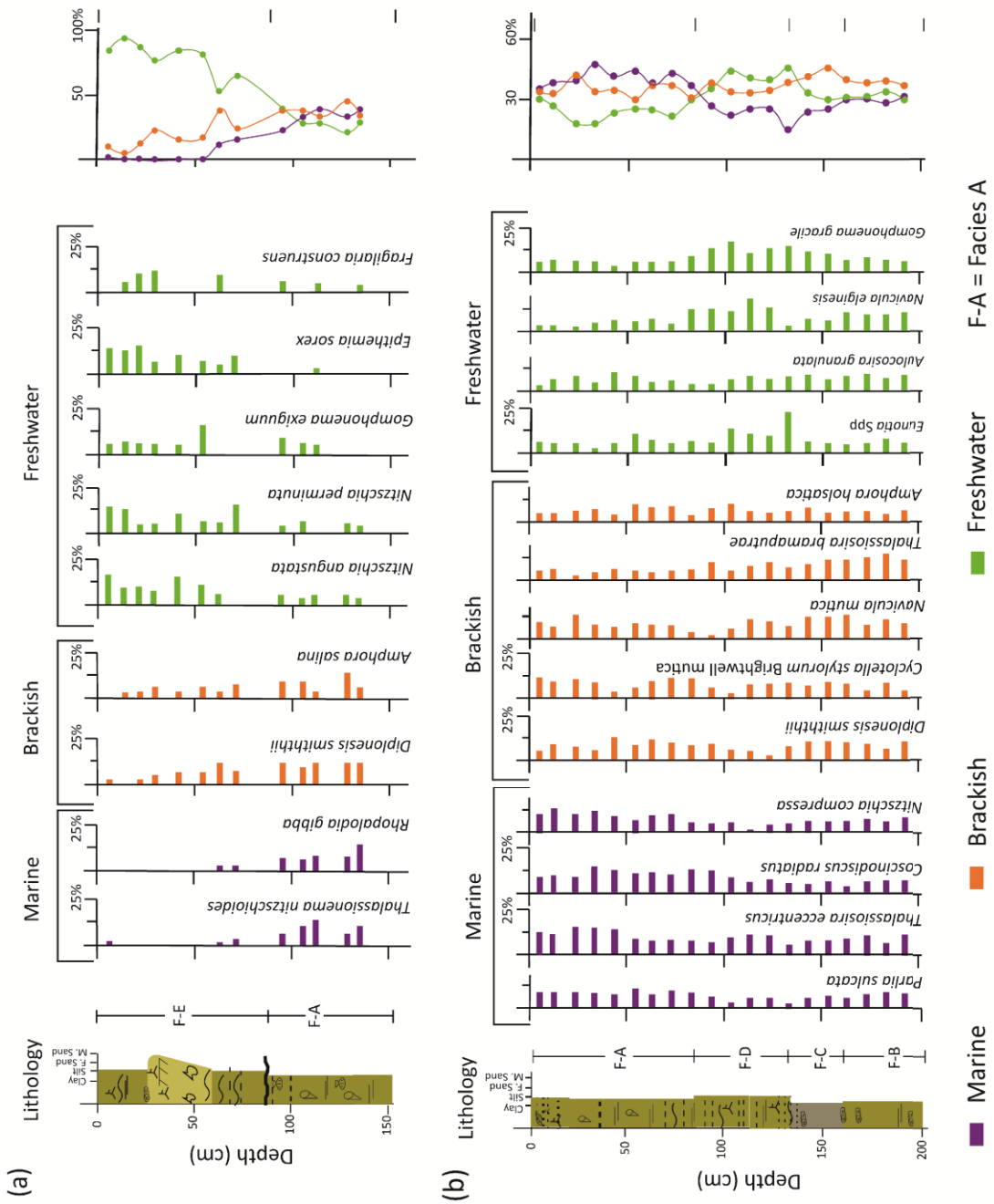

Figure 3.4: Variations of fossil diatom assemblages of two boreholes **(a)** D-1-5 and **(b)** B-2-3 sampling site located at Dhigholia and Batiaghata respectively of the study area (Haque and Hoyanagi, 2021). Legends of sedimentary column see Figure 3.2, Page 28.

Interpretation: The lithology, grain size, and their characteristic features indicate that the sediments could be deposited during the terrestrial river avulsions/flood event over the present level of flood plain or valley flat (Howard et al., 1968). The transitional to terrestrial influence has been observed in the upper part of these sections where the TOC/TN reaches up to 17.97 and relatively lower $\delta^{13}C$ ~−24.18‰ in the D-1-5 succession (Figure 3.2). It has been noted that the $\delta^{13}C$ value is shown lower at the bottom of D-1-2, D-1-3, and D-1-4, and shows higher at the top of the successions due to the growth of sugar cane and paddy field which mostly belong to C_4 Plants (C_4 plant; $\delta^{13}C$ value −17‰– −9‰; Deines, 1980) over the sampling areas. Diatom assemblages suggest the terrestrial freshwater influences in the sedimentary succession of D-1-5 (Figure 3.4a). Figure 3.5 shows that the terrestrial plant originated organic matter input, particularly the C_3 plant is observed in the upper part of the sedimentary sequence at Dhigholia.

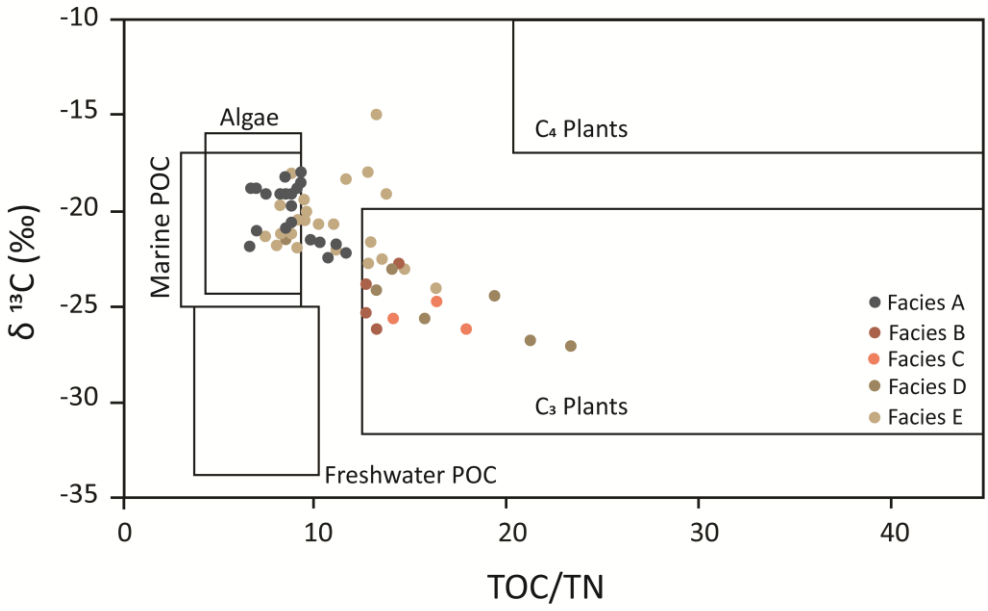

Figure 3.5: TOC/TN and $\delta^{13}C$ values of organic matter to characterize the ranges for different sources of organic matter of the sediments (after Blair and Carter, 1991; Hoefs, 2009; Lamb, 2006; Marchand et al., 2005; Sarkar et al., 2009) of the study area (Haque and Hoyanagi, 2021).

3.3. Discussion

The altitudes of every sampling point and radiocarbon dating have been considered to illustrate the lateral variation of sedimentary facies and the effect of RSL change on depositional environment of the study area (Figures 3.6−3.7). Two facies A (bioturbated light yellow to gray mud) and E (laminated silty sand) are identified at Dhigholia whereas four facies B (bluish gray mud), C (dark gray to black peat with peaty mud), D (yellowish-gray mud), and facies A are found at Batiaghata (Figure 3.6). The time stratigraphy diagram of Wheeler (1964) has been used to illustrate the effect of the RSL on the depositional process of the study area. The ^{14}C age and geometric position have been considered to reconstruct the diagram of RSL and sedimentary environmental changes over the study area (Figure 3.7). Facies A of Dhigholia is shown older in radiocarbon age and deposited before 1300 AD whereas pottery and flood sediment of modern age lies over it (Figure 3.6). Facies C shows the age of 1490±35 AD, Facies D 1782±19 AD, and modern aged samples of Facies A successively found at Batiaghata (Figure 3.6). The area does not have stable datum plain. So, the altitude of the upper part of Facies A at Dhigholia and Facies C at Batiaghata have been compared to the present mean sea level (MSL). This helps to construct a simplified sea level curve (Figure 3.7). The depositional environment of the sediment, chronology and record of global sea level change have been considered to understanding the effect of sea level on the depositional process over the study area. Considering these analyses, the sediments were deposited in three stages- Stage I (850–1300 AD), Stage II (1300–1850 AD) and Stage III (1850 AD –Recent) that show a noticeable effect of RSL on the depositional environment change in the low-lying southwestern delta basin during the last 1000 years (Figure 3.7). The descriptions of the stages are followed.

Stage I (850–1300 AD): Tidal influenced Facies A of Dhigholia was deposited in this stage (Figure 3.7). The shells were found in Facies A at depth 220 cm, 200 cm, and 159 cm at D-1-1 and dated by ^{14}C methods showing the age of 930±57 AD, 1203±47 AD, and 1210±45 AD respectively (Table 3.1; Figure 3.6). The sea level (and ground temperature) was

comparatively higher than the present level in and around 1250 AD (Grinsted et al., 2010; Mann et al., 2009; Warrick and Ahmed, 1996) and it was 90 cm above the present level in the Pacific (Nunn, 1998; Ota et al., 1990). The sediments of Facies A were deposited in the landward upper delta plain at Dhigholia where RSL was higher than the present level (up to +80 cm) over the study area (Figure 3.6).

Table 3.1: Radiocarbon age and sedimentation rate of the study area.

Lab Code	Sam. No.	Location		Materials	Log Depth (cm)	^{14}C age (yr BP)	Calibrated age (cal AD)	Sedimentation rate† (mm/year)
		longitude	Latitude					
IAAA-200074	D-1-1 12	89°33′48.7″E	22°54′13.5″ N	Shell	220	1130±20	930±57	2.20
IAAA-190610	D-1-1 20	89°33′48.7″E	22°54′13.5″N	Shell	200	850±20	1203±47	2.45
IAAA-200075	D-1-1 36	89°33′48.7″E	22°54′13.5″N	Shell	159	840±20	1210±45	1.96
IAAA-190611	B-2-3 153	89°31′28.7″E	22°44′46″N	Peat	153	360±20	1490±35 (50.1%) 1594±38 (45.3%)	2.89
IAAA-200159	B-2-2 68	89°31′5.30″E	22°41′23.7″N	Seed coat	68	220±20	1663±18 (40.7%) 1782±19 (43.4%)	2.88
IAAA-200076	B-2-1 93	89°31′37.07E	22°40′34.48″N	Shell	93	Modern	Modern	-
IAAA-200077	B-2-1 93	89°31′37.07E	22°40′34.48″N	Wood	93	Modern	Modern	-
IAAA-190612	B-2-1 57	89°31′37.07E	22°40′34.48″N	Shell	57	Modern	Modern	-

† The sedimentation rates have been calculated considering higher percentage of probability of calibrated age and sedimentation up to 2018.

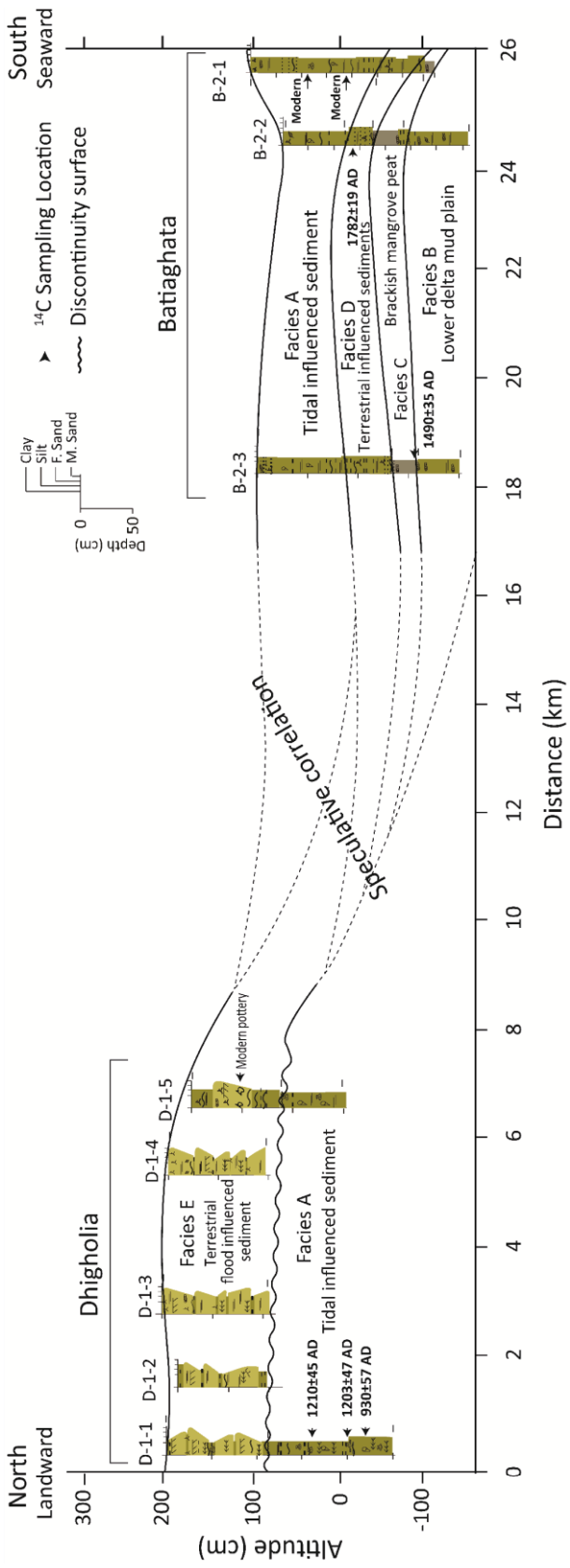

Figure 3.6: Stratigraphic sections showing the vertical and later changes of sedimentary facies, depositional environment along the N–S direction from Dhigholia to Batiaghata (Haque and Hoyanagi, 2021).

Stage II (1300–1850 AD): The lower delta mud plain Facies B, brackish mangrove peat of Facies C, and terrestrial influenced Facies D were deposited successively at Batiaghata during the stage (Figure 3.7). The peat and seed fragments found at B-1-3 and B-1-2 successions showing the age of 1490±35 AD and 1782±21 AD respectively (Table 3.1; Figure 3.6). The ground temperature fell rapidly after 1300 AD towards the Little Ice Age and the level dropped up to 90 cm below the present level measured in the Pacific in 1750 AD (Nunn, 1998; Ota et al., 1990). The mangrove peat has been applied as an indicator of the former sea level (Cohen et al., 2005; Woodroffe et al., 1985) and RSL fell up to 110 cm below the present level (Figure 3.6). The rate of fall of sea level was faster than the subsidence rate and the mangrove ecosystem was replaced by the freshwater habitat ecosystem in the upper part of the sediment (Facies D). Due to the dropped of RSL, upstream water was discharged through the channel causing a down-cut of the river valley and/or increase of riverbed gradient and formed a new base level (Duff, 1993). The terrace and/or non-depositional or erosional surfaces were formed at Dhigholia due to regression and fell of the base level (Figure 3.7).

Stage III (1850 AD –Recent): The tidal influenced sediment of Facies A was deposited over the Facies D at Batiaghata, where the modern aged shell and wood fragments have been found at depth of 57 cm and 93 cm in B-2-1 (Table 3.1), and terrestrial flood sediment of Facies E have been deposited over the Facies A in landward, where modern pottery was found at Dhigholia during this stage (Figures 3.6 and 3.7). The sea level and the ground temperature rose after around 1750 AD and reached the present level (Abu-Zied and Bantan, 2015; Grinsted et al., 2010; Mann et al., 2009; Nunn, 1998, Warrick and Ahmed, 1996). The average rate of MSL rise ranges from 1.1–1.7 mm/year in the last century (Hay et al., 2015; Intergovernmental Panel on Climate Change [IPCC], 2007) and the rising trend of tidal river water level was 3–5 mm/year for the last thirty years (1981–2013) recorded in the study area (Climate Change Cell [CCC], 2016).

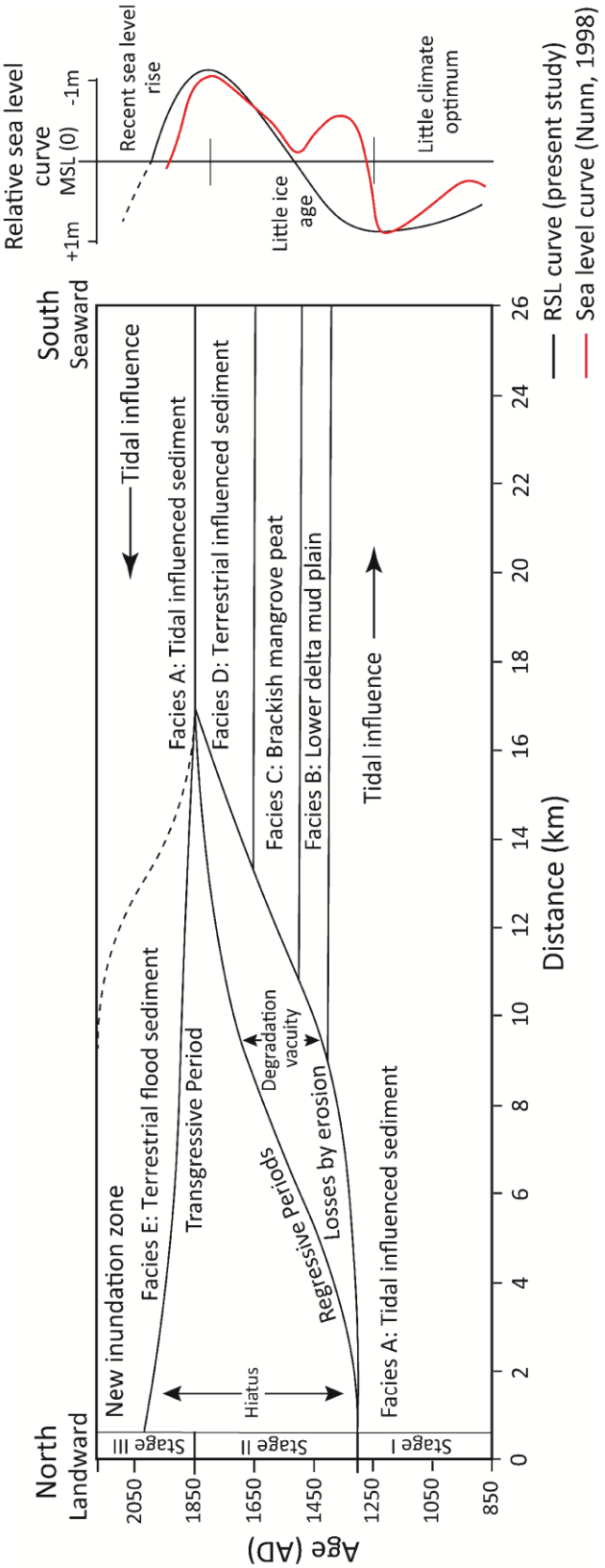

Figure 3.7: Schematic illustration of the depositional environment, time stratigraphy, and relative sea movement in and around the study sites and a comparisn of sea level on a global scale (modified after Haque and Hoyanagi, 2021, Nunn, 1998).

The rise of global temperature has increased the water volume in the ocean influencing the tidal limit, as well as sea level in an area. It also affects the flooding intensities in the coastal region. The net subsidence is attributed to sedimentation, tectonics, compaction; and RSL changes that have triggered the gradual shifting of the coastal environment (Brown and Nicholls, 2015). Due to the shifting of the Ganges estuary from the Khulna region to the east after 1.8 Ka (Allison et al., 2003), the major sediment and flow are now passing through the present GBM estuary and the sedimentation rate has gradually decreased in the southwestern delta basin compare to central estuary delta (Figure 1.1). The estimated average sedimentation rate of the study is 1.96–2.89 mm/year of the last 1000 years (Table 3.1) - that is calculated by using depth to ^{14}C age of organic matter - is also comparable to the average sedimentation rate of the Holocene 2–5 mm/year over the southwestern GBM delta (Allison et al., 2003; Islam and Tooley, 1999; Stanley and Hait, 2000), and modern ^{137}Cs based sediment accumulation rate ranging from 0–11.3 mm/year with an average of 3.7 mm/year in the lower delta plain areas (Allison and Kepple, 2001). The dominant sediment of southwestern lower delta plain has been supplied by GBM estuary, carried westward by tidal transport, and deposited inland by cyclone event and monsoonal coastal setup (Figure 1.1). For that, the sedimentation rate shows higher in the lower delta compare to the upper delta plain (Allison and Kepple, 2001; Goodbred Jr. et al., 2014; Willson and Goodbred Jr., 2015). The subsidence over the study area ranges from 1.5–2.0 mm/year (Krien et al., 2019) whereas it is 2.8 mm/year reported for the Sundarbans (Brown and Nicholls, 2015; Karpytchev et al., 2018) and reached up to 5.2 mm/year along the coast (Hanebuth et al., 2013) (Figure 1.1). The elevation of Sundarbans varies from 0.9 to 2.11m above sea level (Ghosh et al., 2015, 2016; Spalding, 2010). The average sedimentation rate of Holocene is insufficient to offset the effect of subsidence and the rising trend of present sea level (Hanebuth et al., 2013; Willson and Goodbred Jr., 2015). Due to the rising trend of the sea level as well as the base level, the influences both the terrestrial and coastal flood have increased and created a new area of inundation that also increases the sedimentation over the area (Alongi, 2015; Griffiths et al., 2019; Nicholls and Wilson, 2001; Pickering et al., 2017;

Takagi et al., 2016). For this, upstream water is hindered while flowing through the channel increasing the terrestrial flood-influenced sediment deposits over the erosional surface towards the land, tidal influenced sediment from the coast deposited upon it (Figure 3.7). The effect of the recent trend of rising sea level (Figure 3.7) and sediment supply characteristics along the river mouth of southwestern GBM delta coast has been demonstrated in Chapter 4.

3.4. Conclusions

The study interprets the depositional environment and their relation to the relative sea level change of southwestern GBM delta, Bangladesh. Five facies have been identified with the sedimentary successions. The geochemical proxies and diatom assemblages have been used to characterize the organic matter and reconstruct the depositional environment of the sediment. Tidal influenced Facies A is identified in the lower part at the Dhigholia (landward) that was deposited during 850–1300 AD when sea level reached higher than the present. The sea level fell after around 1300 AD and lower delta mud plain Facies B, brackish mangrove peat of Facies C (1490±35 AD), and terrestrial influenced Facies D (1782±19 AD) were deposited successively at Batiaghata toward the sea. These sediments were deposited during the regression of the period 1300–1850 AD and the terrace was formed at Dhigholia due to the lowering of the base level. Tidal influenced Facies A gradually thickened at lower delta plain Batiaghata where a new level of inundation occurred due to the rising trend of the sea after 1850 AD along the study area. It also hinders upstream water flow through the channel increasing flood intensities and the terrestrial flood deposits of Facies E are deposited over the erosional surface at the upper delta plain of the Dhigholia. The depositional process of the low-lying southwestern GBM delta has been controlled by the sea level; the intensities of the terrestrial flood sediment deposits in landward and tidal influenced sediment from sea gradually deposit upon it due to the rising trend of the present sea level. The findings of the study will contribute to understanding the effect of sea level on depositional environment change in the last 1000 years, particularly for the coastal region.

CHAPTER 4

Effect of sea level rise on geological development in southwestern delta coast

This chapter has been modified from the accepted article titled 'Coastal development in southwestern Bangladesh: understand the interplay between storm and sea level rise' in *Progress in Physical Geography* (2021, Doi: 10.1177/03091333211046189).

4.1. Introduction

Sea level rise and sediment supply have influenced coastal morphology and sedimentation on Bangladesh's southwestern GBM delta coast (Haque et al., 2021a). Recent satellite images along the GBM delta coast reveal that net gain in land area was comparatively higher in the central delta estuary than along the southwestern coast of the delta (Brammer, 2014; Sarwar and Woodroffe, 2013) (Figure 1.1). Periodic erosion and accretion, as well as internal changes in delta systems, are common and they can balance themselves if the systems are undisturbed, but erosion has been dominant over the last three decades, especially along the southwestern coast of the delta. Ahmed (1999) proposed that most of the coastal erosion was caused by both continuous wave action and storm surges, and the rate of erosion increased with increasing wind speed (Hossain, 2012). The coast of Bangladesh has shallow offshore bathymetry. Storms, especially tropical cyclones, which have eroded the coast, including offshore, beaches and dunes. The eroded sediments are transported to the steep canyon walls of the Swatch of No Ground in the Bay of Bengal (Figure 1.1) and are also deposited onto the low elevation nearshore and coastal zone (Hanebuth et al., 2013; Kudrass et al., 2018; Morton and Sallenger Jr., 2003; Shibayama et al., 2008; Williams and Flanagan, 2009). Rahman et al. (2011) and Bhargava et al. (2021) showed that southwestern coast accretion was mainly observed along the west and east. In contrast, erosion was higher in the south to southwest direction (Figure 1.1).

Sedimentation processes on the open tidal coasts are controlled by the input of riverine sediment and influence of offshore wind and waves (Yang et al., 2005). The landward extension and thickness of storm overwash deposits depends on wind speed and tidal surge height, and the storm builds its deposit above the spring tidal limit (Hesp, 2006). Storm deposits show different forms among the various coastal environment settings such as tidal flats, backshore, inner shelf, etc. (Xiong et al., 2018). Many diverse and comprehensive suites of proxies have been used to

identify the characteristics and provenance of coastal deposits (Das et al., 2013; Lambert et al., 2008). In the GBM delta system, most sediment from upstream accumulates along the central coastal island located at the mouth of the estuary and a portion is transported southwestward and temporarily stored offshore where the water depth is less than 20 m. This sediment has been resuspended and carried west by coastal current and directed in the tidal channels by tidal currents (Allison, 1998; Allison and Kepple, 2001; Barua et al., 1994; Mikhailov and Dotsenko, 2007; Mouyen et al., 2018; Rahman et al., 2018; Wilson and Goodbred Jr., 2015) (Figure 1.1).

Bangladesh's coastal area is storm dominated and one of the most unstable deltaic coasts in the world. In this study, satellite images of different vintages have been used to find a suitable location that would represent the coast of the southwestern GBM delta of Bangladesh in terms of coastal morphology and sedimentation. Remote sensing techniques are combined with geological core analyses to understand coastal depositional processes. The field survey was carried out in the Haringhata coastal area of the Barguna district, Bangladesh, on 10–13 February 2020 (Figures 1.1 and 4.1). General morphological features of the coast are shown in Figure 4.2. Samples were collected from three sites along a north-south transect to interpret the depositional environment (Figure 4.1). Satellite images were analyzed to interpret morphological change. A detailed methodology for sample collection, laboratory analyses and satellite image processing have been described in Chapter-2.

The specific objectives of the study include: 1) documenting the coastal dynamics of the Haringhata region over a period of 43 years (1977 to 2020) using satellite images; 2) identification of depositional environments and sources of organic matter using sedimentary facies and laboratory analyses of grain size, total organic carbon (TOC), total nitrogen (TN), stable carbon isotope ratio ($\delta^{13}C$ values) and diatom assemblages from core and 3) understanding sedimentary processes and the causes of morphological changes.

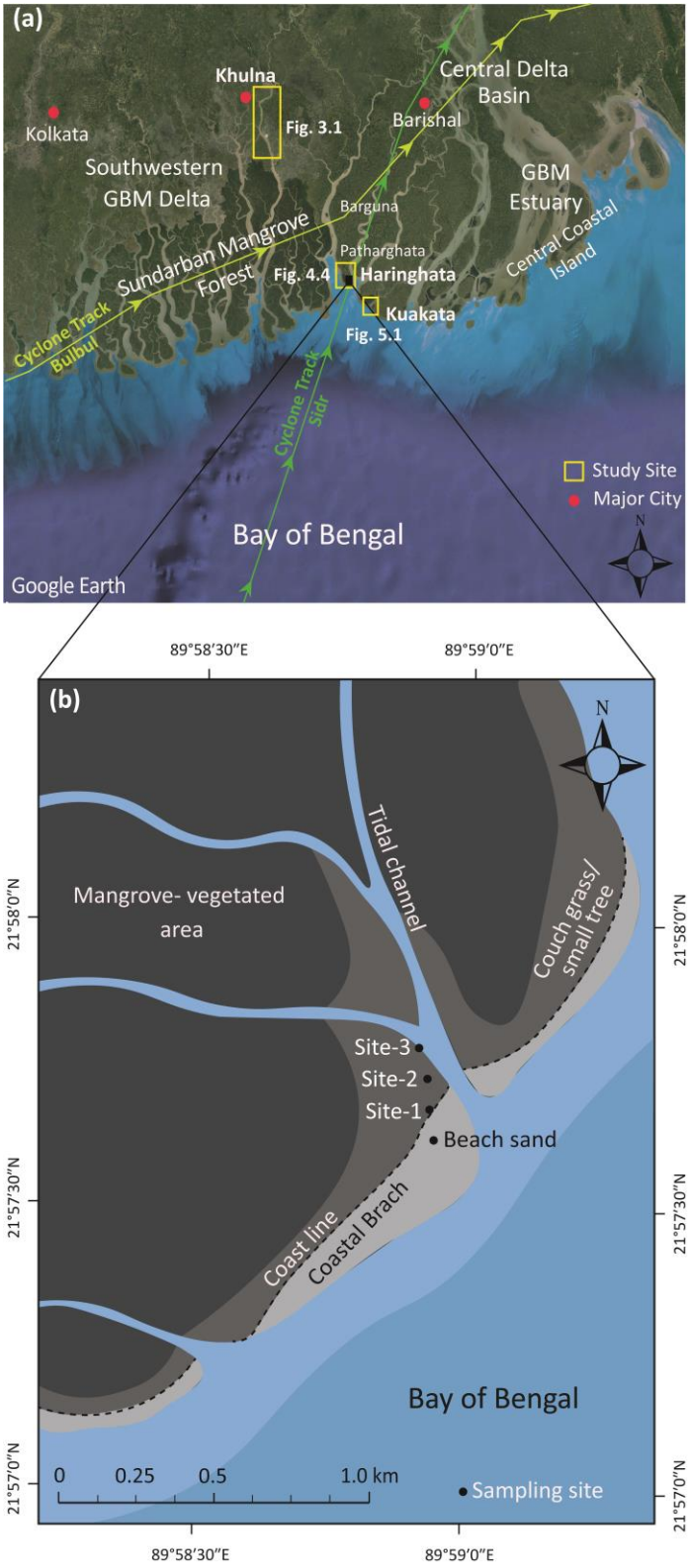

Figure 4.1: (a) Path of Cyclone Sidr (2007) and Bulbul (2019) passing over the study area (Haque and Jahan, 2016; Needs Assessment Working Group [NAWG], 2019). **(b)** Field investigation map of Haringhata coastal region shows the sampling sites (modified after Haque et al., 2021a).

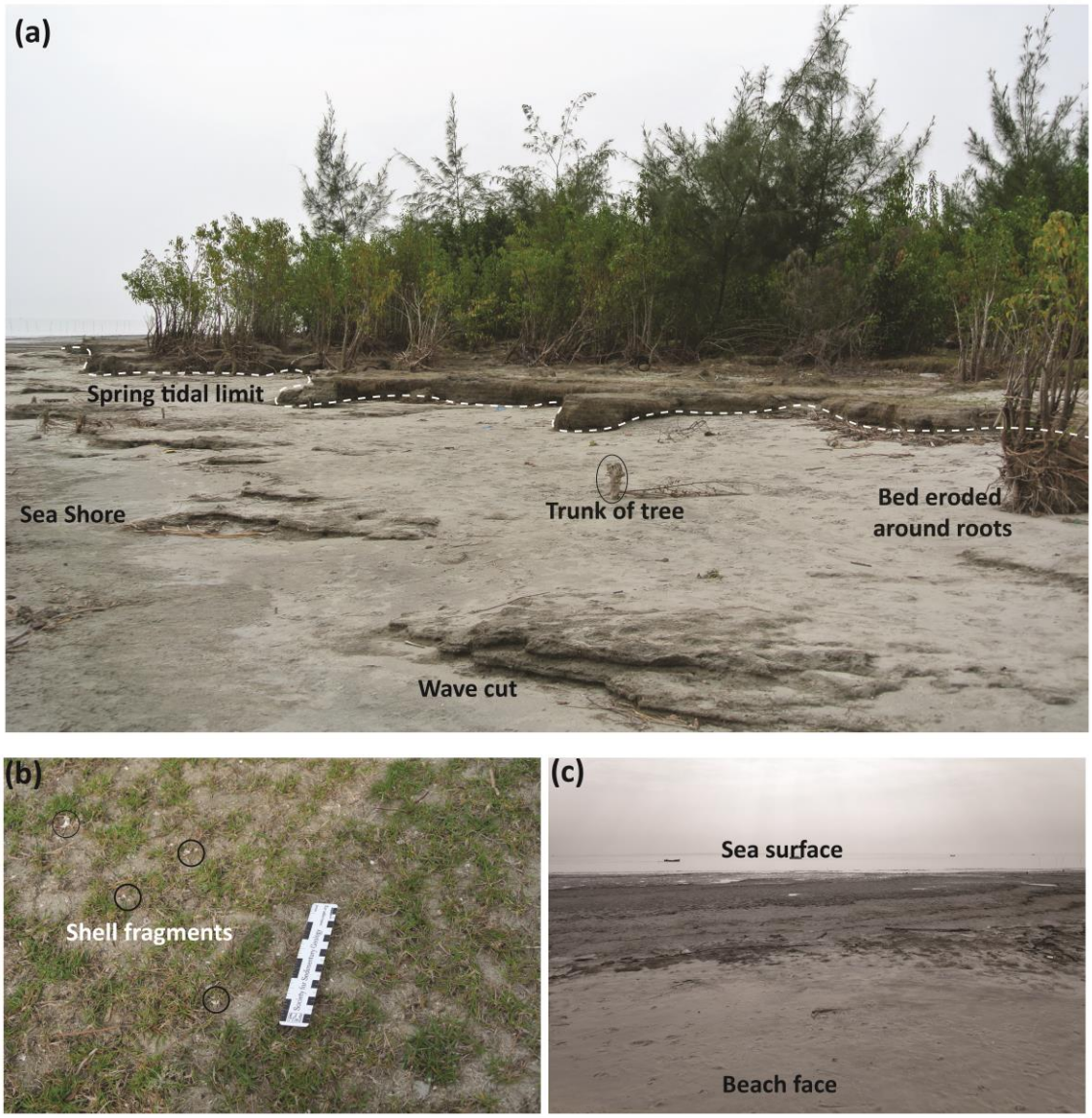

Figure 4.2: (a) General morphological feature of the study area, showing coastal erosion, wave cut formed soil erosion near Site-1 (along the southern coastline); **(b)** sand with shell fragments were found during field investigation; **(c)** beach face during low tide (toward the Bay of Bengal) (modified after Haque et al., 2021a).

4.2. Results

4.2.1. Coastline dynamics and morphological change

The NDWI image for 1977, and MNDWI for 1989, 2000, and 2020 are shown in Figure 4.3. The image classifications for land and water resulted in overall accuracies of 83%, 86%, 89%, and 94% and kappa indices of 0.74, 0.83, 0.87, and 0.92 for the images of 1977, 1989, 2000, and 2020, respectively (Table 4.1). The results also indicate that the difference between MNDWI generated coastlines and the 'true' coastlines digitized from reference data varies between 3 to 11 meters (Table 4.1), indicating that the MNDWI technique is robust.

The coastline changes in the Haringhata region are shown in Figures 4.4−4.5 (a–d) while the extents of erosion and sedimentation are given in Table 4.2. Three regions (western, southern, and eastern) of the Haringhata coast are recognized where the changes are evident. Accretion has been dominated on the western and eastern parts of the coast whereas the southern part of the coast was subject to erosion (Table 4.2). In addition, some parts of the coastline were unchanged.

Table 4.1: Range of difference between MNDWI generated coastline positions and reference data generated coastline positions, kappa coefficient and overall classification accuracy for the images.

Location	Type of Landsat Image	Displacement in meter in respect to reference data		Kappa coefficient	Overall classification accuracy (in %)
		Highest	Lowest		
1977	MSS	11	7	0.74	83
1989	TM	8	5	0.83	86
2000	ETM	6	4	0.87	89
2020	OLI	4	3	0.92	94

The dynamics of the coastline between 1977 and 1989 is shown in Figure 4.5a. Western and eastern parts of the Haringhata coastline experienced a net accretion of 5.50 km^2 and 5.64 km^2, with the coastline displacement ranging between 0.15 and 1.2 km, and 0.12 and 1 km, respectively. These changes affected the coastlines for approximately 12 km along the strike in each case. In contrast, the shorter southern coast (2.7 km long) experienced net erosion of 3.24 km^2 with a coastline displacement ranging between 0.7 and 1 km.

Figure 4.5b shows the coastline dynamics between 1989 and 2000. The locations that experienced accretion are again the western and eastern coast, which are 10.3 km and 11.7 km long, respectively. However, the amount of accretion is greatly reduced to the 1977–1989 period. Coastline advancement was only 0.11–0.49 km in the west and 0.05–0.66 km in the east net accretion 0.04 km^2 and 1.10 km^2, respectively. In contrast, the short southern coast 4.9 km long, experienced net erosion of 5.44 km^2 and coastline retreat ranging between 0.22 km and 1.4 km.

Between 2000 and 2020, the southern part of the Haringhata coastline, which extends for 4.8 km, witnessed net erosion of 3.48 km^2 and coastline retreat ranging between 0.09 and 0.90 km. In contrast, the western and eastern parts of the coastline, extending for 9 and 11.3 km, respectively, experienced net accretion of 0.79 km^2 and 0.41 km^2, with corresponding coastline advance ranging between 0.04 km and 0.66 km, and 0.03 km and 0.76 km.

The total change in coastline position during the entire forty-three years period between 1977 and 2020 is shown in Figure 4.5d. Western and eastern coasts experienced net accretion of 3.53 km^2 and 5.72 km^2 and coastline advance ranging between 0.09 km and 1.4 km, and 0.02 km and 2.5 km, respectively. The location exposed to extended erosion is the southern coast. The total erosion in this location was 8.91 km^2 with 2.3 km and 2.9 km of coastline retreat.

The erosion to accretion ratio (E–A ratio) is an indicator of shoreline dynamics, which is a measure of the degree of variation across the period from 1977 to 2020. The coast is constructive if the E–A ratio is less than 1. Consequently, it loses its land mass or it is erosional if the ratio is above 1. Accretion was highest during 1977–1989 when the E–A ratio was 0.29.

Landmass was lost as erosion increased from 1989 to 2000 and erosion substantially decreased from 2000–2020 (Table 4.2). Most of the accretion occurred along the western and eastern directions, whereas erosion occurred along the southern direction (Figure 4.4). Satellite image analysis reveals that the southern coastline experienced retreat due to erosion from 1977–2020, ranging between 5 and 127 m/year. In contrast, the western and eastern coastline experienced seaward advancement due to accretion, ranging between 2 and 100 m/year and 0 and 83 m/year, respectively.

Table 4.2: Erosion, accretion, and E–A ratio of selected locations from 1977–1989, 1989–2000, 2000–2020, and 1977–2020 at Haringhata, Bangladesh.

Location	1977–1989				1989–2000			
	Erosion (in km²)	Accretion (in km²)	Overall Change (in km²)	E–A ratio	Erosion (in km²)	Accretion (in km²)	Overall Change (in km²)	E–A ratio
Western coast	0	5.5	(+) 5.50	0.29	0.95	0.99	(+) 0.04	4.77
Southern coast	3.24	0	(-) 3.24		5.44	0	(-) 5.44	
Eastern coast	0.07	5.71	(+) 5.64		0.05	1.15	(+) 1.10	
	2000–2020				1977–2020			
Western coast	0.44	1.23	(+) 0.79	2.90	0.31	3.84	(+) 3.53	0.96
Southern coast	3.48	0	(-) 3.48		8.91	0	(-) 8.91	
Eastern coast	0.06	0.47	(+) 0.41		0.11	5.83	(+) 5.72	

Overall change, (+) = Accretion [A]; (-) = Erosion [E]

$$\textbf{E–A ratio} = \frac{\Sigma\, Erosion\ (km^2)}{\Sigma\, Accretion\ (km^2)}$$

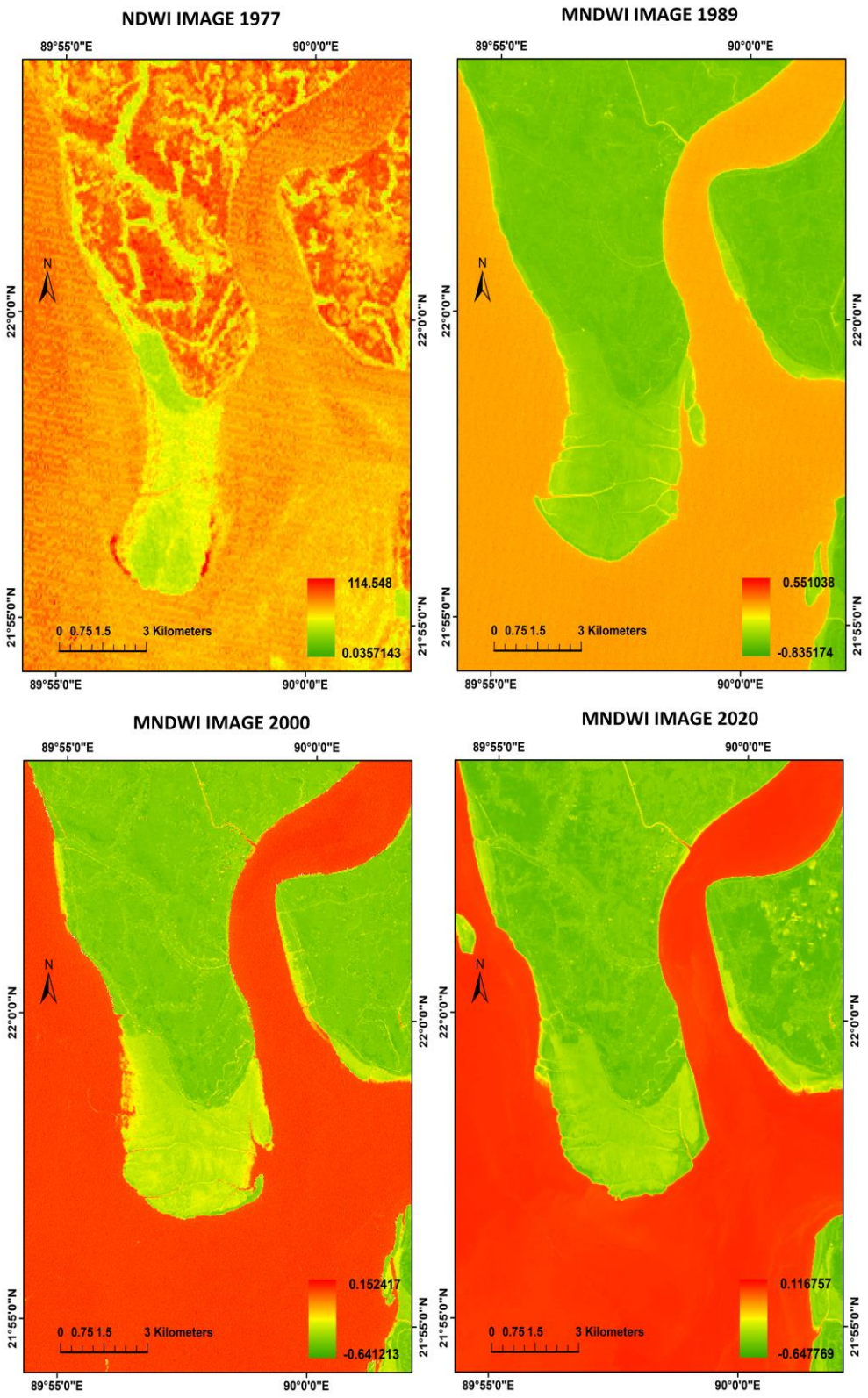

Figure 4.3: MNDWI and NDWI images of the Haringhata coastal region (Haque et al., 2021a).

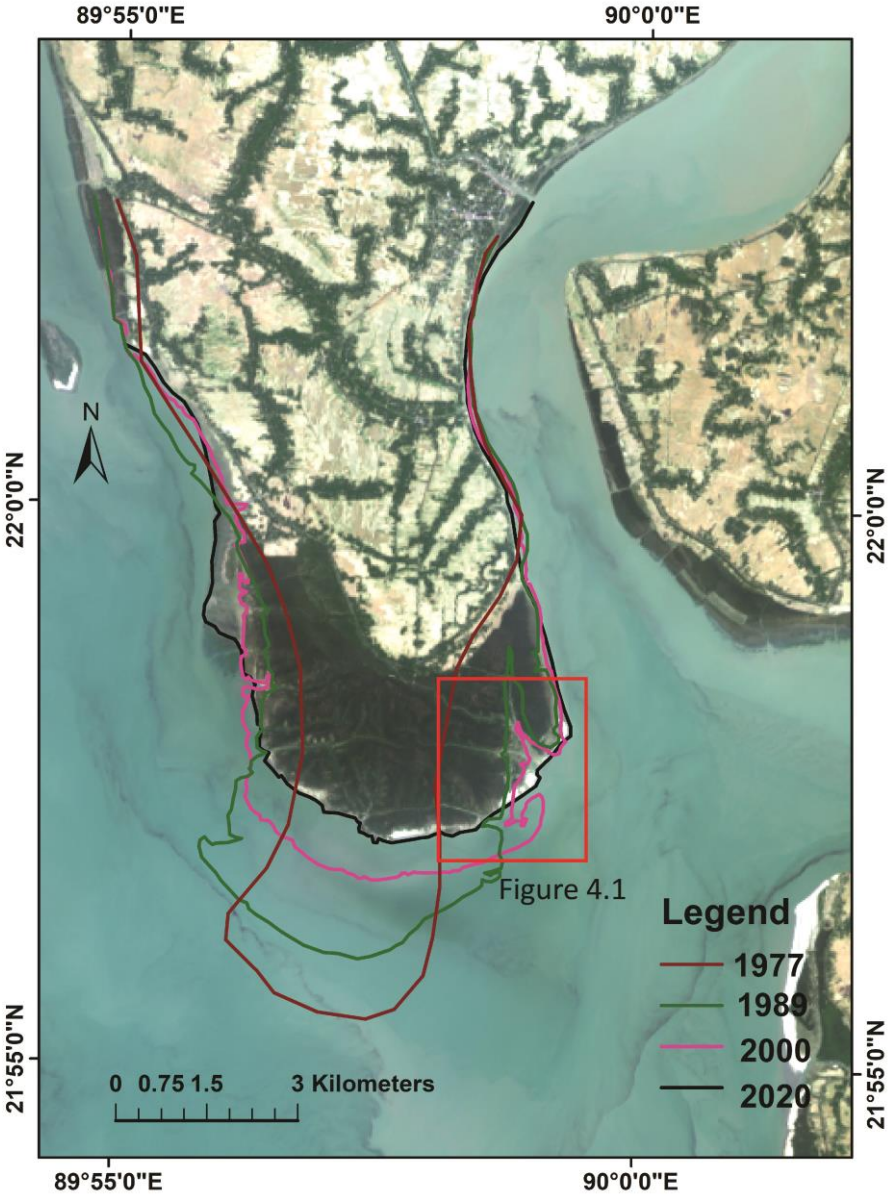

Figure 4.4: Coastline change map of the study area, based on image analysis from 1977 to 2020 (Haque et al., 2021a).

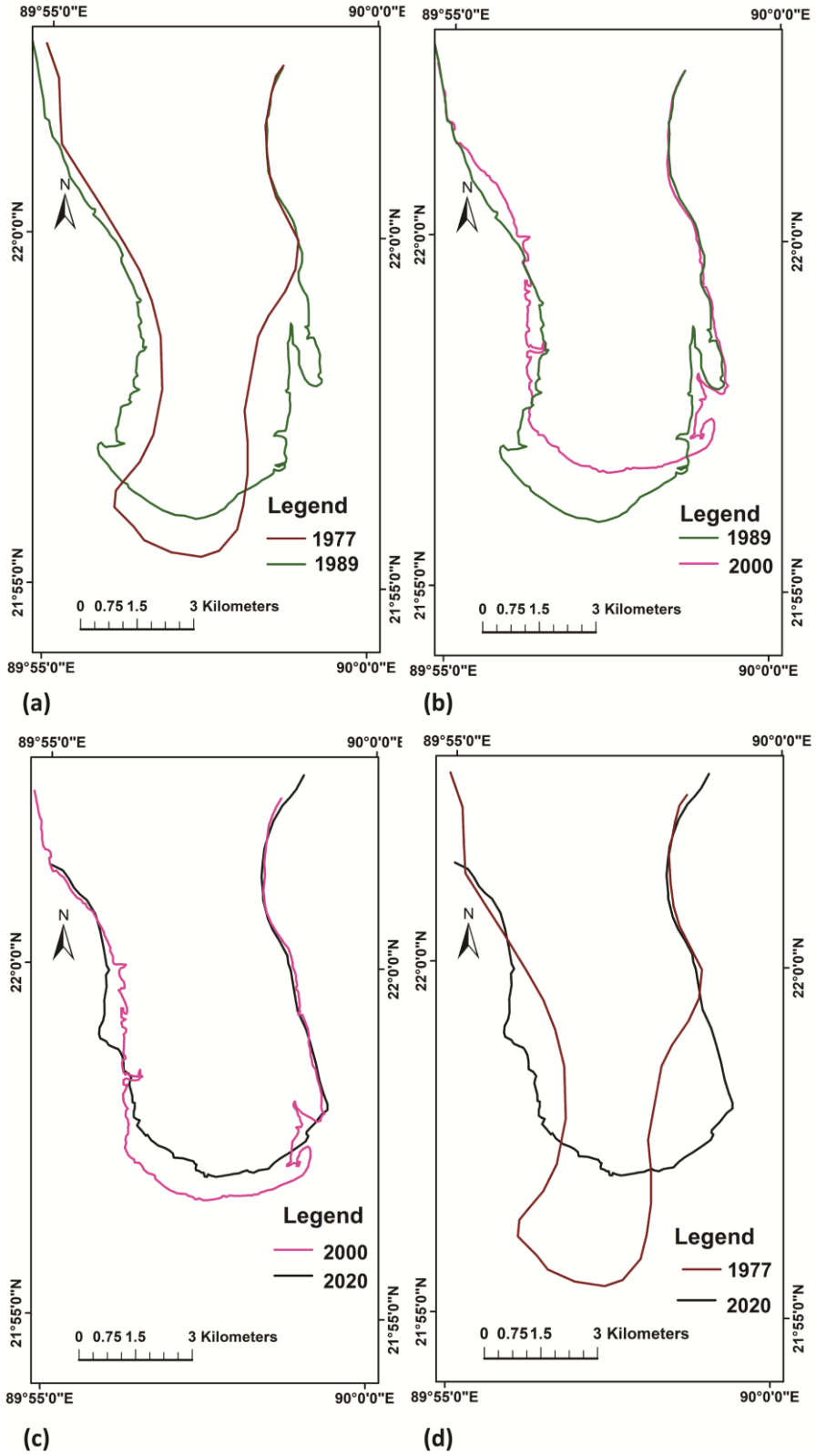

Figure 4.5: Coastline change map based on image analysis from **(a)** 1977 to 1989, **(b)** 1989 to 2000, **(c)** 2000 to 2020, and **(d)** 1977 to 2020 (Haque et al., 2021a).

4.2.2. Sedimentary facies and depositional environment

Lithology, grain size and sedimentary structures in the three cores allow the definition of two sedimentary facies up to 130 cm thick (Figure 4.6). A summary of organic geochemical proxies results is shown in Table 4.3. These sedimentary facies, together with geochemical proxies and diatom assemblages, can be used to define the origin of organic matter, provenance and depositional environment of the sediments.

4.2.2.1. Facies A (bluish gray mud)

Facies A contains 72–91% mud (clay 7–11% and silt 65–80%) and 9–28% sand and occurs in the deepest part of the succession. Parallel to wavy laminated bluish gray mud is interbedded lenticular to ripple laminated yellowish gray to grayish white silty to very fine-grained sand (Figure 4.6a). Laminated mud–sand couplets are also observed in the upper part of the facies (Figure 4.6b). The bottoms of the ripples are sharp, and lenses corresponding to the ripples are asymmetric with foresets dipping in opposite directions. Some ripples showed offshoot structure. The facies showed yellowish red to grayish red and contained plant fragments and rootlets. The average TOC and TOC/TN of the facies range between 0.14% and 0.87%, 7.1 and 18.8, respectively. The $\delta^{13}C$ values range between –24.4‰ and –19.7‰, and the highest values at the bottom of the facies, decreasing upward (Figure 4.7; Table 4.3).

Interpretation: The abundance of mud indicates that the facies was deposited by settling in slack water, alternating with a high energy regime that permitted the transportation and deposition of very fine-grained sand (Figure 4.6). The presence of lenticular bedding, ripples, and asymmetric lenses with foresets dipping in opposite directions indicates tidal influence (Basilici et al., 2012; Greb and Archer, 1998; Tessier, 1998; Yang and Nio, 1985). The sand and mud laminae have not shown systematic thickness variation. The occurrence of sand within a muddy interval was generated by tidal current rather than the storm (Nio and Yang, 1991). The offshoot structures of the ripples indicated wave energy during the deposition of the sediment. Very fine-grained sand and mud couplets imply an upper intertidal to a supratidal flat

environment where plant rootlets and yellowish to grayish red sediment suggest that the sediments were deposited above the fluctuating normal tidal limit (Hori et al., 2001; 2002) (Figure 4.6). The sedimentary structures and geochemical proxies indicate a transitional coastal environment of the lower delta plain where the organic matter in the sediment was primarily of marine origin (Figure 4.7). The amount of terrestrial influenced organic matter increases in the upper part of the facies because mangrove forests gradually covered the area after deposition (Figures 4.2a and 4.4).

Table 4.3: Site coordinate, distance from the coast, and summary of mean grain size, and geochemical proxies of litho-sections at Site 1–3.

Core ID	Coordinate		Distance from Coast (m)	Lithology	Mean grain size (µm)	Organic geochemical proxies		
	Latitude	Longitude				TOC (%)	TOC/TN	$\delta^{13}C$ (‰)
Site 1	21°57'40.62"N	89°58'56.10"E	edge of coast	Facies B	105	0.36–0.74	10.6–14.7	−22.82–−18.82
				Facies A	42	0.25–0.87	8.8–18.8	−24.35–−19.69
Site 2	21°57'44.03"N	89°58'55.89"E	120	Facies B	82	0.18–0.69	8.9–12.9	−20.80–−18.81
				Facies A	40	0.19–0.42	9.23–12.1	−23.54–−22.10
Site 3	21°57'47.21"N	89°58'54.66"E	225	Facies B	65	0.15–0.57	7.4–13.3	−21.89–−18.82
				Facies A	44	0.14–0.39	7.1–13.65	−23.12–−21.48

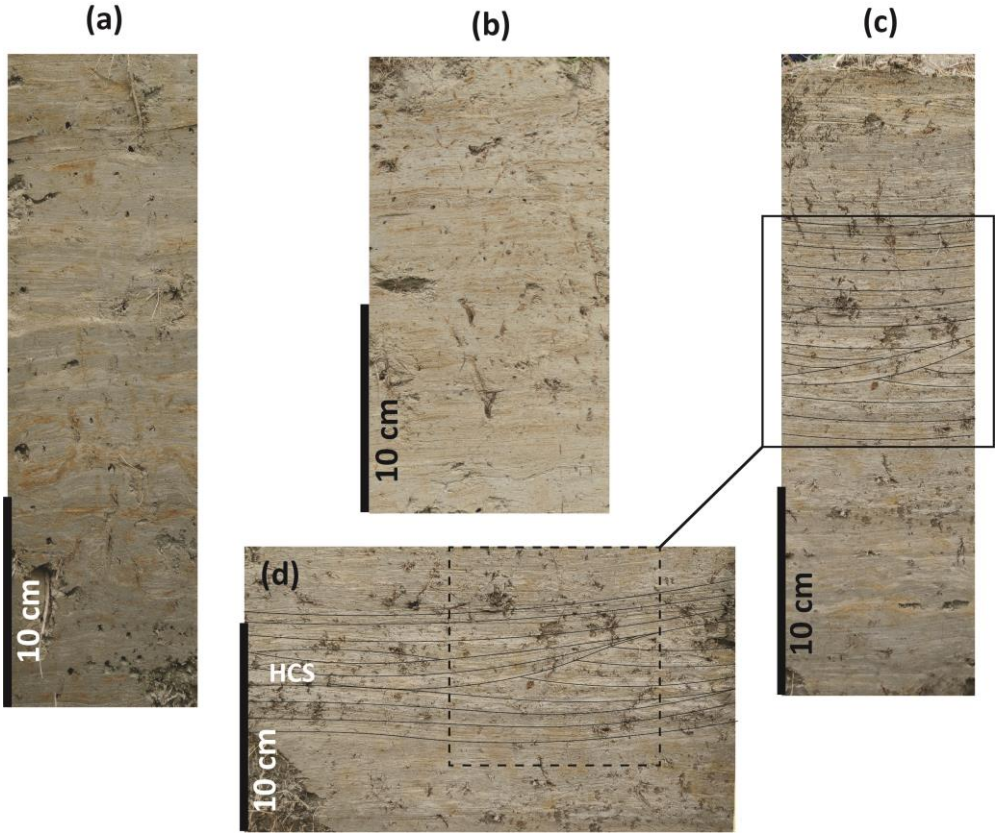

Figure 4.6: (a) Parallel to wavy laminated bluish gray colored mud interbedded with lenticular to wavy laminated silty to very fine-grained sand with burrows found at Site-3 indicate tidal influences; **(b)** very thin sand-mud couplets with plant rootlets found at Site-3 indicate upper intertidal to supratidal flat deposit; **(c)** parallel stratification to hummocky cross stratified normal graded storm overwash deposits overlies the bluish gray mud with sharp to depositional contact at Site-2; **(d)** gradual change of sedimentary structure with low angle to parallel laminae in the lower part, hummocky cross-laminated dip upward, and parallel laminae in the upper part of the bed (modified after Haque et al., 2021a).

4.2.2.2. Facies B (gray to grayish white silty sand)

Facies B overlies the bluish gray colored mud and contains 31–62% mud (clay 3–6% and silt 28–56%) and 38–69% sand. The facies has a low angle parallel laminae at the lower part, hummocky cross-stratification (HCS) at the middle and horizontal laminae at the upper part (Figures 4.6c−d). HCS extends laterally up to 55 m and has had a tabular shape in outcrop. The basal surface of the facies has a sharp contact. The fieldwork was conducted after cyclone Bulbul affected the coast in November 2019 (Figure 4.1a; NAWG, 2019). A sandy layer with shell fragments covered the surface of the study area (Figure 4.2). The grain size of these surficial sediments gradually decreases inland, whereas mud concentration and sorting value increase (Figure 4.8). The grain size distributions at Site-1 show that the sediments of Facies A are dominated by mud, whereas Facies B shows a bimodal population with a mixture of mud and fine-grained sand (Figure 4.9). The grain size distribution of Facies B shows fining upward whereas mean grain size decreased from coast to inland (Figures 4.7–4.8; Table 4.3). The average TOC values of Facies B range between 0.15% and 0.74% and TOC/TN values are between 7.4 and 14.7. The $\delta^{13}C$ values are high at the base of the facies (–20.2‰ to –18.8‰) and lower in the upper part (–20.7 ‰ to –22.8‰; Figure 4.7; Table 4.3).

The lateral variation of diatom assemblages in the surficial sediment of Facies B is shown in Figure 4.9. The marine species *Thalassiosira oestrupii*, *Bacterosira fragilis*, *Cyclotella stylorum* and brackish species *Cyclotella striata*, *Frafilaria fasciculata*, *Navicula halophila* are abundant at Site-1. The brackish *Navicula cryptotenella*, *Navicula pygmaea* and *Navicula perminuta*, and freshwater *Nitzscia recta* and *Cymbella pusilla* diatom species are abundant at Site-3. The total relative abundance of diatoms gradually changes from marine–brackish at the more outboard Site-1 to brackish–freshwater at the more inland Site-3. The beach sediment is dominated by brackish to freshwater species.

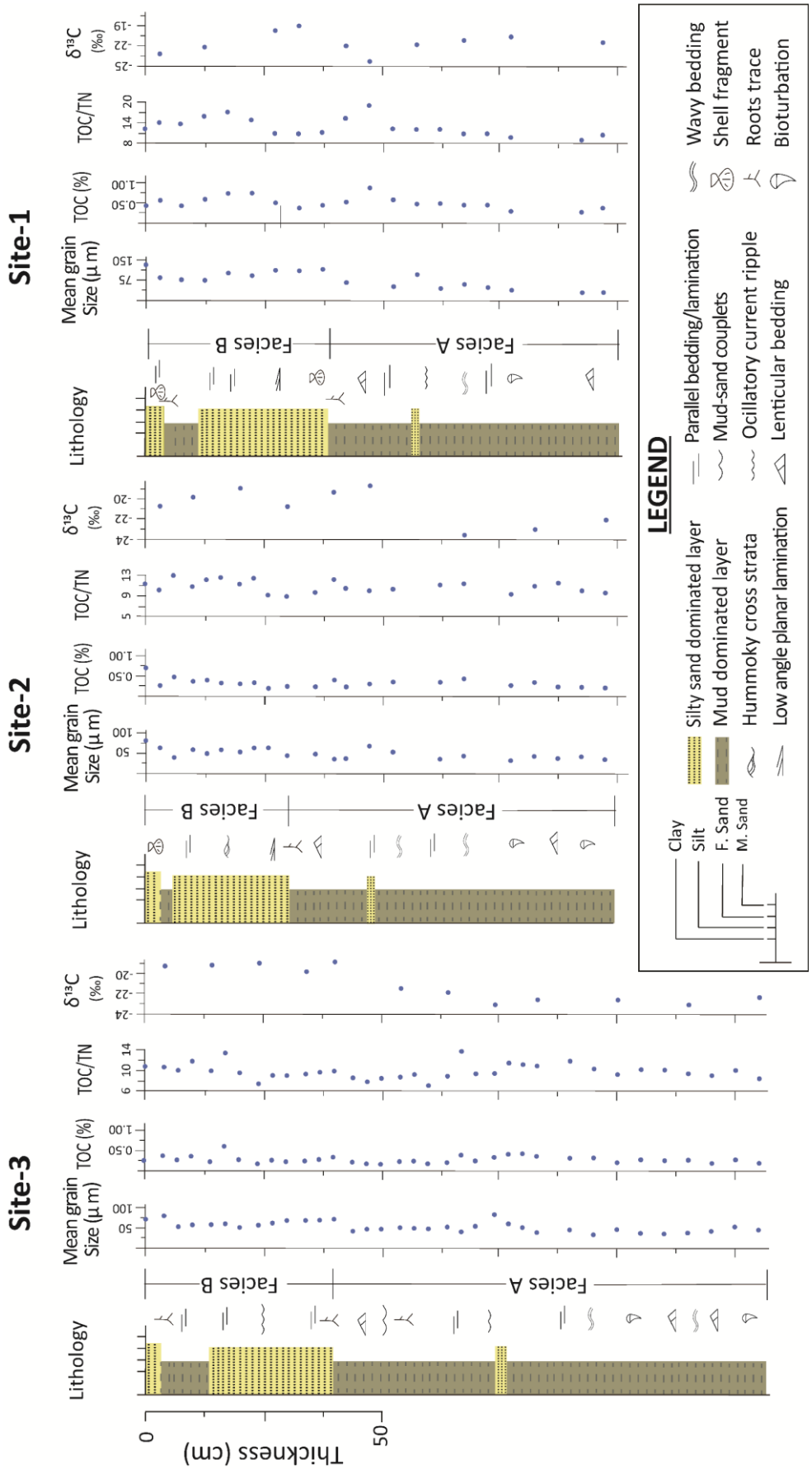

Figure 4.7: Vertical distribution of mean grain size, TOC, TOC/TN, and $\delta^{13}C$ values of litho-sections at Site 1–3 (Haque et al., 2021a).

Interpretation: Facies B overlies the Facies A with parallel stratification to HCS, and the depositional process is similar to tidal beaches in coastal environment (Daidu et al., 2013). However, HCS on open coast sandy tidal flats typically has a smaller wavelength than HCS on beaches and shelves (Yang et al., 2005). The landward extent of storm overwash deposits commonly ranges from 200 to 400 meters from the shoreline with reported a maximum of 1600 meters during extreme storm wave events (Morton et al., 2007; Soria et al., 2017). Tides could have deposited the sand grain, but most of the sands were produced by oscillatory flows, either alone or combined with unidirectional flows. Continuous waves form beaches (Bird, 1960; Curray et al., 1969; Tanner, 1995) and combined wind and wave energy enhance the process that causes coastal erosion (Figure 4.2). In contrast, waves generated by a tropical cyclone can erode materials from foreshore to shoreface (beached, dune, etc.), and deposit them in more inland low energy depositional settings such as backshore, tidal march, swamp, lake, and above the spring tidal limit (e.g., Buynevich et al., 2004; Das et al., 2013; Donnelly et al., 2004; Hesp, 2006; Morton and Sallenger Jr., 2003; Williams and Flanagan, 2009). Sediment eroded from the coastal beaches was the probable source of sand in storm overwash deposits. Anisotropic HCS is an indicator of fair-weather conditions, as well as physical mechanisms of tides or waves that combine with sufficient energy of an extreme wave event, such as cyclone, that affects the proximal and sheltered area of the coast (Basilici et al., 2012) (Figure 4.6). The combination of high intense precipitation, wind, and storm surge produces floods in the low-lying coastal region, and water levels reach up to 12 m above mean sea level during storm surge (Antony et al., 2014; Auerbach et al., 2015; Krien et al., 2017).

The grain size of the surficial sediment decreases inland and sorting increases, indicating that the beaches were the probable sources of sand in the Facies B (Figure 4.8) (Brill et al., 2016; Haque et al., 2021b; Nott et al., 2013). The grain size distribution of Facies B shows a bimodal population where mud carried by the suspended and nearshore deposit of bay and sand sourced from the beaches are mixed (Figure 4.9). The grain size with positive excursions in $\delta^{13}C$

values, indicate the marine influence of severe storm events (Das et al., 2013; Lambert et al., 2008) (Figure 4.7). All the analyses refer that the facies is storm overwash deposits and deposited during a severe storm surge. The TOC (%) and TOC/TN values gradually increase and $\delta^{13}C$ values decrease in the upper parts of the facies indicating post-depositional changes due to the growth of plants and the contribution of organic matter from C3 plants from the mangrove forest as well as post-depositional growth of couch grass ($\delta^{13}C$ values of C_3 plant range between –28.33‰ and –25.26‰) (Figures 4.1−4.2).

The diatom assemblages of the surficial sediments show relative abundance of marine–brackish diatoms in the seaward samples (Site-1), gradually changing to freshwater–brackish dominated in the samples collected from 120 m (Site-2) and 225 m (Site-3) inland (Figure 4.10). The landward decrease of marine–brackish diatoms indicates the presence of freshwater sources during deposition of the sediment. Heavy precipitation during the storm would have flooded the adjacent river and its tributaries that carry suspended mud and freshwater diatoms towards the coast. The grain size and diatom assemblages indicate that land-derived sources were likely incorporated with storm deposits during deposition. The depositional characteristics and landward extension of sandy sediment indicate that the tropical cyclones SIDR of 2007 (Category 4 on the Saffir–Simpson scale) and Bulbul of 2019 that affected this coast were likely responsible for the overwash deposits of Facies B (Figure 4.1a; Haque and Jahan, 2016; Krien et al., 2017; NAWG, 2019). The upstream freshwater mixes with seawater and creating low sea surface salinity near the coast (Behara and Vinayachandran, 2016; Benshila et al., 2014; Felton et al., 2014; Vinayachandran et al., 2002). As a result, the beach sediments contain relatively greater amount of freshwater–brackish diatoms.

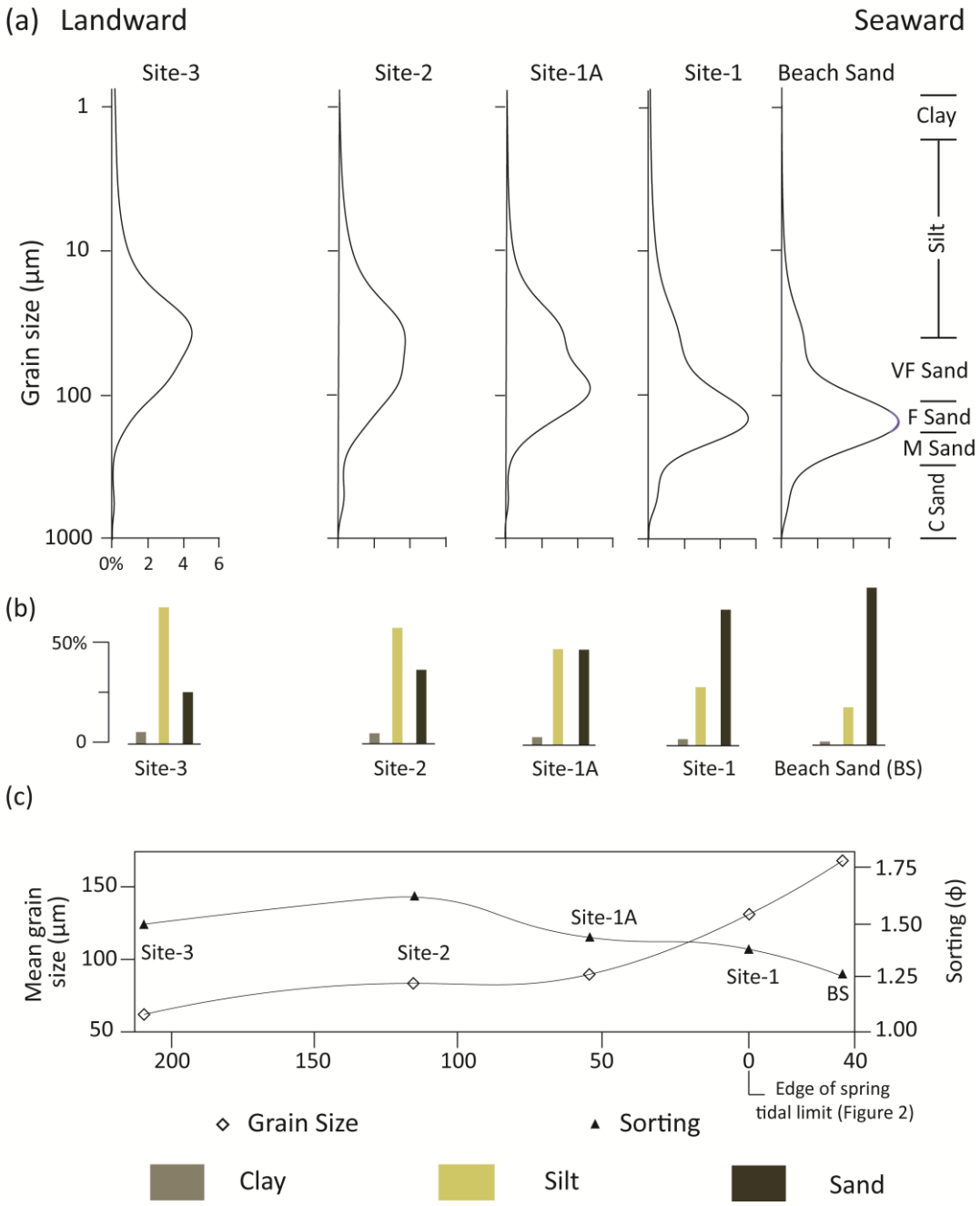

Figure 4.8: Lateral variation of **(a)** grain size distribution; **(b)** clay, silt, and sand percentage, and **(c)** mean grain size and sorting values of surficial sediments of Site 1–3 and beach sand (Haque et al., 2021a).

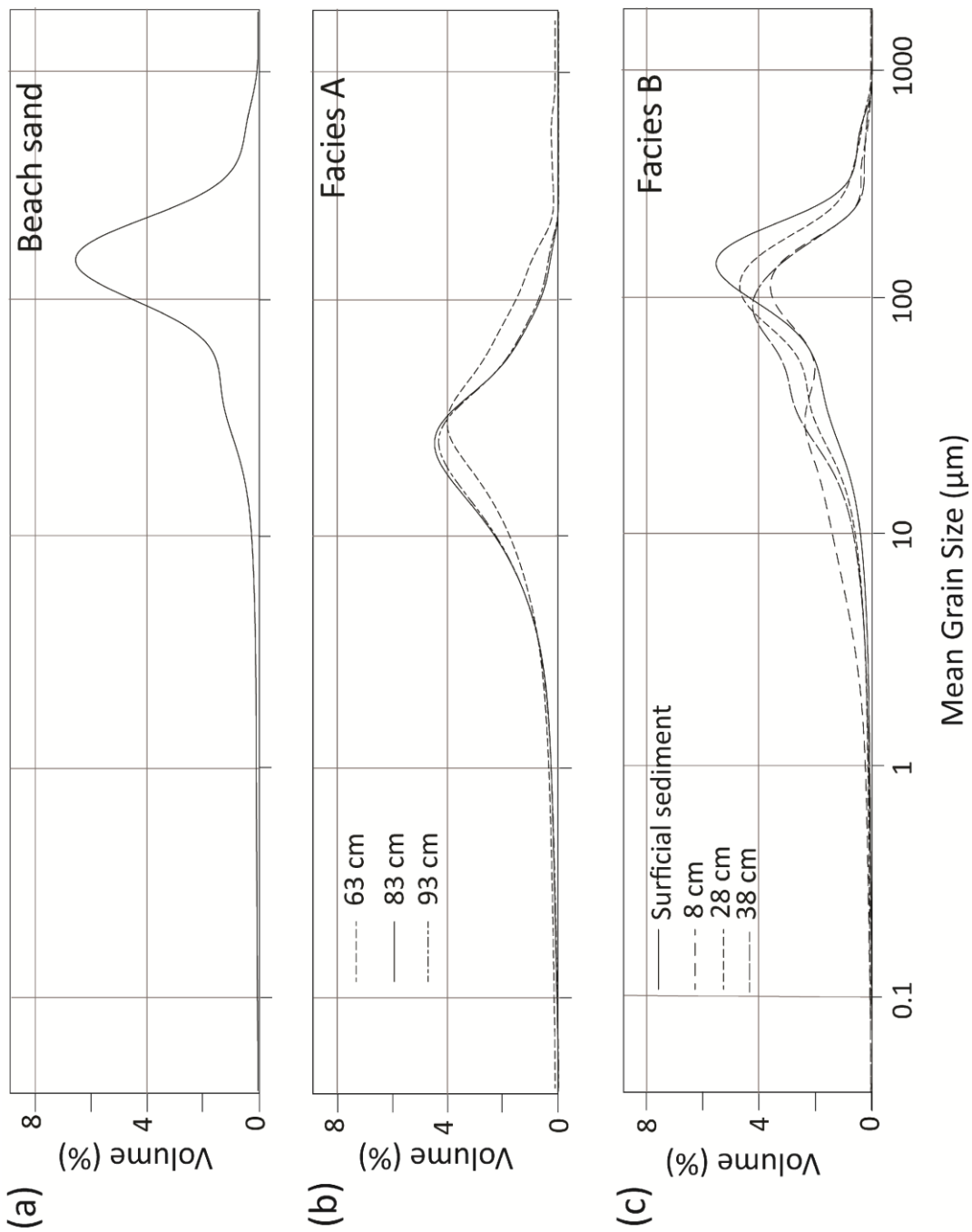

Figure 4.9: Comparison of grain size distribution among **(a)** beach sand, **(b)** Facies A, and (c) Facies B of Site-1 (Haque et al., 2021a).

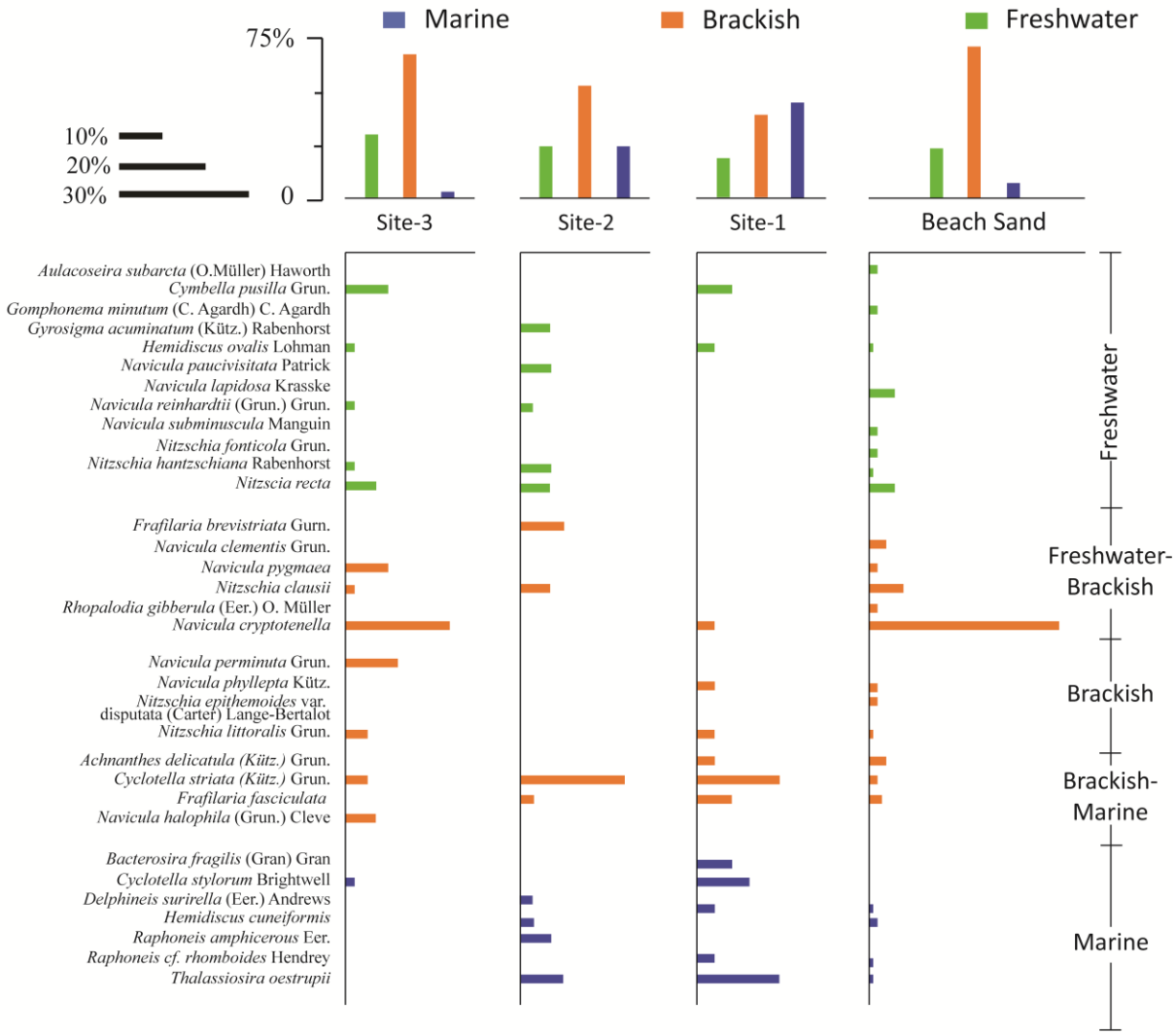

Figure 4.10: Fossil diatom assemblages of surficial sediments at Site 1–3 and beach sand (Haque et al., 2021a).

4.3. Discussion

The most remarkable outcome is the enormous change in the coastline because of the firm erosion and sedimentation impacts. Comparison of data from satellite images and cores provides new insights into, and a thorough understanding of the morphology and stratigraphic development of the southwestern coast of the GBM delta. The trend of rising sea level along the area (Figure 4.11; CCC, 2016) and limited sediment supply from upstream (Islam and Gnauck, 2009; Rahman et al., 2018) likely caused the morphological changes observed in the area (Figure 4.4). Figure 4.12 shows the influence of sea level rise, coastal erosion, and depositional processes on the study area. The lower part of the succession (Facies A) was deposited under marine conditions where tides and waves play an important role in transportation and reworking of sediments. The storm overwash deposits (Facies B) overlie Facies A. The coastline dynamics, sedimentary facies, geochemical proxies and diatom assemblages provide understanding of the complex evolution of deposits and morphological change within the study area.

The GBM delta coastal area comprises two physiographic units – the tidally active southwestern GBM Delta, that is covered by Sundarbans mangrove forest, and the central delta basin of GBM estuary (Islam and Gnauck, 2008) (Figure 1.1). The change of delta morphology depends on the balance between sediment added and removed from the coastal system. The morphological change of a delta system is controlled by the rate of relative sea level rise (R), rate of sediment input from river (Q), grain size (M) and marine processes for sediment transport (D). The coastal dynamics depend on the accommodation and sediment supply ratio (R·D: Q·M) and the system is balanced if the ratio is 1. If the increased amounts of sediment (Q) are delivered to the river mouth, it can overcome the effect of rising sea level (R·D<Q·M), and the delta becomes a constructional landform (Swift and Thorne, 1991). This condition also introduces more terrestrial organic matter from upstream to the deposits (Milliman and Farnsworth, 2013). The delta lobe was constructive during the period 1977−1989 (E–A ratio is 0.29), but the ratio ranges to 2.90–4.77 during the last thirty years and the coast loses landmass (Figure 4.4; Table 4.2). Bhargava et al. (2021) reported that the E–A ratio was 2.20 in the Sundarbans mangrove forest area from 1984 to 2018, which corresponds with our study.

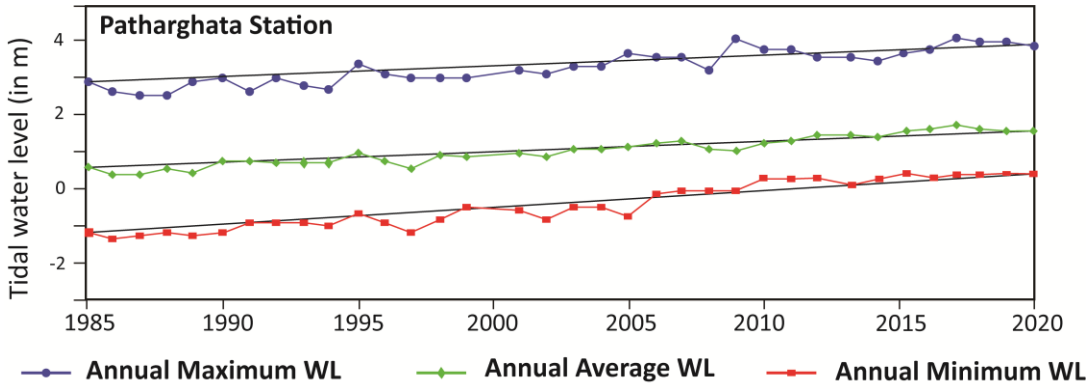

Figure 4.11: Observed trend of tidal water level using tide gauge at Patharghata based on the linear regression analysis over the last 35 years (modified after Climate Change Cell [CCC], 2016).

Rahman et al. (2018) reported that the sediment load of the GBM delta system is declining at a rate of 4×10^6–10×10^6 ton/year and sediment discharge is now 50% less (500×10^6 ton/year) than the earlier estimate (Goodbred Jr. and Kuehl, 1999; Milliman and Meade, 1983; Milliman and Syvitski, 1992). The contribution of sediment from the Ganges River system was significantly reduced following the construction by the Indian Government in 1975 of the 'Farakka' barrage (river dam) to divert Ganges main streamflow. The barrage has caused a gradual decrease in flow of the Ganges River over the past 45 years (Mirza, 1998; Pethick, 2012; Shaha and Cho, 2016; Winterwerp and Giardino, 2012). The river flow over the study area is linked to the mainstream of the Ganges mainstream through the Gorai River tributaries. The Gorai River water discharge was significantly decreased from 3338 m^3/sec in 1962 to 500 m^3/sec in 2003 and the tributaries of the southwestern delta are not significantly connected well to carry upstream sediment (Allison and Kepple, 2001; Islam and Gnauck, 2009; Wilson and Goodbred Jr., 2015). If the sediment is directed from the adjacent river, the modern sedimentation rate probably remained constant or decreased from river to ocean. However, comparatively higher sediment accumulation rate in the lower delta plain area indicates that sediment was mainly discharged through the GBM estuary, transported and deposited under the influences of the tides, waves and storm surges (Allison and Kepple, 2001; Haque and Hoyanagi, 2021; Wilson and Goodbred Jr., 2015) (Figure 1.1).

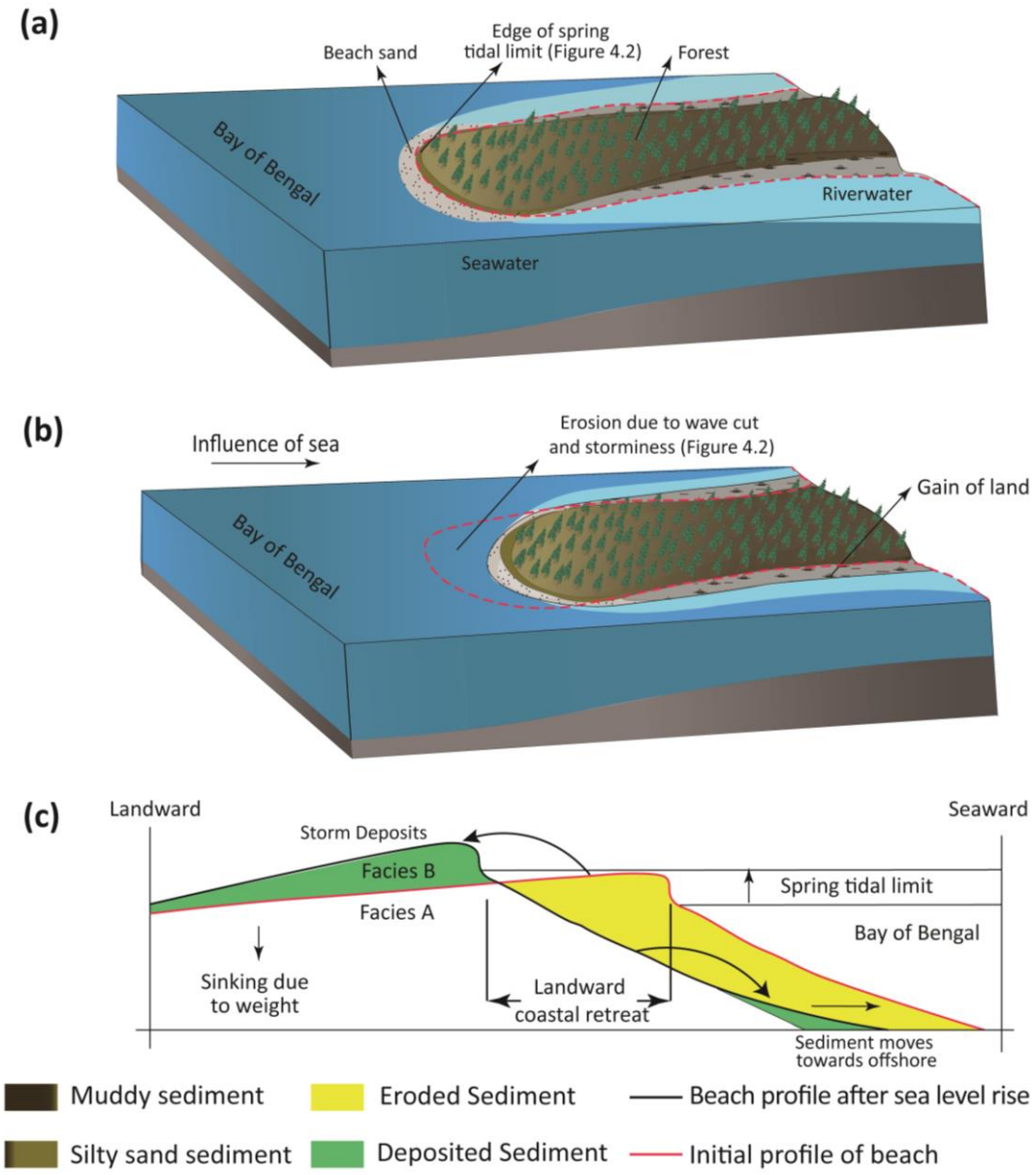

Figure 4.12: (a–b) schematic diagrams of northward migration of land due to coastal erosion and storm-dominated silty sand sediment gradually thickened over tide-dominated muddy sediment from coast to inland (Brunn, 1962); **(c)** conceptual process for the erosion and preservation process of storm-dominated southwestern coast of Bangladesh (Haque et al., 2021a).

Facies A was deposited in a marine influenced environment along the river of the Haringhata coast (Figure 4.12). The sediment that is transported and deposited as modern deposits of Facies A is initially sourced from the river mouth, being dispersed onto the offshore and stored on seasonal as well as annual timescales. Wave and tidal current subsequently resuspended the stored sediment and deposited onshore (Barua 1990; Rogers et al. 2013; Stanley and Hait 2000). Such sedimentaries and environments are also observed in modern deposits along the Rupsa–Pasur river in the southwestern lower delta plain area (Haque and Hoyanagi, 2021). Parallel to cross stratified Facies B of the storm overwash deposits overlies the Facies A with sharp contacts. Core analyses (Figure 4.7) and lateral variation of grain size of surficial sediments (Figure 4.8) show normal grading as well as landward fining and thinning trends. These characters are typical of modern overwash deposits (e.g., Hawkes and Horton, 2012; Horton et al., 2009; Morton et al., 2007; Nott et al., 2013; Shigeno and Nanayama, 2016; Soria et al., 2017; Switzer and Jones, 2008; Williams and Flanagan, 2009). Presence of multiple layers/parallel laminae in storm deposits have also been observed widely (e.g., Brill et al., 2016; Phantuwongraj et al., 2013; Shigeno and Nanayama, 2016; Soria et al., 2017; Switzer and Jones, 2008). The mean grain size for suspended river sediment is approximately 6.5 φ (11.1 μm) (Datta and Subramanian, 1997) and monsoonal floods and rainfall during cyclones carries suspended mud to the ocean. In contrast, tidal advection transported suspended sediment from offshore and also reworked and eroded the nearshore and beach face sediments (Figure 4.2a). These sediments were redeposited during storm landfalls and enhanced the sedimentation rate along the coast (Allison and Kepple, 2001).

The satellite images show that the southern coast permanently lost landmass while deposition occurred along both eastern and western flanks of Haringhata (Figures 4.4–4.5). The sediments carried by the GBM estuary temporally settle on the offshore and then resuspended due to tidal and coastal currents, resulting in rapid accretion along the Haringhata coast (Barua, 1990; Mikhailov and Dotsenko, 2007). The overall E–A ratio is 0.96 indicates that erosion and deposition were balanced from 1977 to 2020 (Table 4.2). This highlights the several factors

such as tides, waves and storm surge might be involved in the redistribution of eroded sediment to balance the sediment budget. In contrast, the area lost landmass during the last 30 years (Table 4.2). This loss was caused by a reduction in sediment input from upstream such that rising sea level was able to increase accommodation, and marine influences gradually increased (R·D>Q·M) (Swift and Thorne, 1991).

Waves and currents removed more sediment than was delivered to the southern coastline and it retreated throughout the period of observation (Figure 4.4). However, wave height and direction at 21° N, 90° E, close to the study area, did not change significantly from 1989–2010 (Shibly and Takewaka, 2012). Therefore, other processes may also be involved in increasing the E–A ratio at the southwestern GBM delta coast. The morphological change may be controlled by two factors: relative sea level rise due to both local subsidence and eustatic rise, and decreasing sediment input from upstream. Subsidence is relatively rapid for the young delta sediment, ranging between 2.8−5.2 mm/year (Brown and Nicholls, 2015; Hanebuth et al., 2013; Karpytchev et al., 2018) and relative sea level rise (7−8 mm/year) can significantly exceed the eustatic rise (3.0±0.7) (Figure 4.11; CCC, 2016; Hay et al., 2015). The sediment supply is insufficient to balance subsidence along the southwestern coast. Both processes increase the inequality (R·D>>Q·M) leading to landward advanced of the shoreline.

The rapid sedimentation that occurred during the storm events could maintain coastal elevation in the face of sea level rise, but these occasional events were unable to offset the physical damage caused by sea level rise and reduced sediment supply from upstream over the last thirty years. The morphological development of the area is the result of both increased marine influence due to relative sea level rise and decreased fluvial influence, including water flow and fluvial sediment supply caused by anthropogenic activity. The southwestern delta coast permanently lost landmass; marine influences, as well as tides, waves, and storm surges, redistributed the eroded sediments which progressively thickened towards land (Figure 4.12; Brunn, 1962). The characteristics, sources, and depositional processes of modern storm

overwash deposits have been described in Chapter 5. The outcome of this study will contribute to understanding the influences on deposition and erosion in the coastal area.

4.4. Conclusions

The effect of sea level rise and fluvial sediment supply on the southwestern GBM delta development have been interpreted by integrating satellite images and core analyses. Satellite image analysis shows that the southern coastline underwent permanent land loss, while the western and eastern coastline advanced seaward. Parallel to wavy laminated bluish gray Facies A was deposited in an intertidal to supratidal coastal environment. Geochemical proxies imply that marine-influenced sediments were the major contributors of organic matter in Facies A. Planner stratification to HCS silty sand of Facies B overlies the muddy Facies A. The grain size distribution of Facies B indicates two different sedimentary components. Mud was supplied by the adjacent river and from resuspended offshore sediment, and sand was reworked from the coastal beaches. The grain size distribution and diatom assemblages of Facies B suggest that storm surge inundation occurred simultaneously with river flooding due to intense precipitation during cyclones. The geological development of the delta coast is the result of the combined effects of the increased marine influence due to sea level rise and reduction in sediment supply from upstream. Both processes act to moved accommodation landward. Coastal erosion and accretion of the southwestern GBM delta coast was also influenced by tides and storm surges which led to significant sediment redeposition.

Combining satellite images and geological core analyses provides insights into the coastal morphology and depositional processes at the Haringhata coast river mouth. Investigation of geological data extending over longer time periods and high-resolution satellite images would further expand our understanding of delta evolution, particularly in the context of climate change.

CHAPTER 5

Depositional setup and characteristics of storm deposits following the 2007 Cyclone Sidr at Kuakata coast

This chapter has been modified from the published article titled 'Depositional setup and characteristics of the storm deposit by the 2007 Cyclone Sidr on Kuakata Coast, Bangladesh' in *Marine Geology* (2021, Vol. 442, 106652).

5.1. Introduction

Tropical cyclones are known as one of the major sources of coastal and shallow marine sedimentation, resulting in storm deposits. The storm deposits show different characteristics among the distinctive coastal environment setting are generated by distinct sedimentary and hydrodynamic processes, which are related to geological and ecological factors of the region (Xiong et al., 2018). Storm surge that is formed by cyclone, reworks and erodes nearshore and beach face sediment. Then the sediment gets transported and deposited on low energy coastal setting including backshore tidal marsh, swamp, lake and above the spring tidal limit along the coast (e.g., Buynevich et al., 2004; Das et al., 2013; Donnelly et al., 2004; Hesp, 2006; Morton and Sallenger, 2003; Williams and Flanagan, 2009). The deposits are products of meteorological, hydrodynamic, sedimentary, and ecological processes, have been recognized to be excellent research objectives for coastal sedimentary dynamics, reconstruction of paleoenvironment, assessment of different event deposits, management and restoration of coastal wetland (e.g., Cahoon, 2006; Das et al., 2013; Degeai et al., 2015; Elsey-Quirk, 2016; Elsner et al., 2000; Guntenspergen et al., 1995; Liu and Fearm, 1993; Morton et al., 2007; Turner et al., 2006; Walker, 1984). Several studies have been carried out to characterize the distinguishing feature of high energy extreme wave event deposits like tsunami and storm surge (e.g., Das et al., 2013; Foster et al., 1991; Goff et al., 1998; Goto et al., 2015; Hawkes and Horton, 2012; Horton et al., 2009; Kortekaas and Dawson, 2007; Kudrass et al., 2018; Morton et al., 2007; Nott et al., 2013; Phantuwongraj and Choowong, 2012; Pilarczyk et al., 2016; Soria et al., 2017, 2018; Switzer and Jones, 2008; Williams, 2009).

The combination of high intense precipitation and cyclonic wind produces flood, and storm surge height goes up to 12 m with a severe consequence in the low-lying coastal region of Bangladesh (Antony et al., 2014; Auerbach et al., 2015; Krien et al., 2017). Hasegawa et al. (2008), and Haque and Jahan (2016) noted that Cyclone Sidr (November 2007) was one of the severe tropical cyclones (a Category 4 storm type on the Saffir-Simpson Hurricane wind scale

of 1 to 5) that hit Bangladesh (Figure 4.1a). Since, sedimentary signature, grain size and sorting of storm deposits are significantly influenced by the magnitude and local geological factor in an area (Brill et al., 2016; Matias et al., 2008; Shigeno and Nanayama, 2016; Soria et al., 2017; Watanabe et al., 2018).

The study area locates at the western part of Kuakata, Patuakhali, and is one of the most frequently storm affected areas on the southern coast of Bangladesh (Figure 1.1). The coast loses its landmass due to the sea level rise and is facing some extreme wave events. Rahman et al. (2013) mentioned that the western Kuakata suffers erosion that causes a shoreline shifting toward inland on an average of 350 m (maximum 450 m) from 1984–2010 (Figure 1.1). The study area is near the coast and has an approximately 150 m wide sloping sandy beach (Figure 5.1). The embankment, that was erected in 1962 separating the shoreline and the residential area is appx. 12 m wide and 5 m high above mean sea level (Japan Society of Civil Engineers [JSCE], 2008; Shibayama et al., 2009). Only an extreme wave event like Sidr overtops the embankment and inundates behind the area of the embankment.

The complexity of hydrodynamic (interaction of bay and fluvial/river flooding) and geomorphologic process have contributed the depositional process during a storm in low lying coastal regions. No work has been conveyed to characterize the storm deposits precisely in the coastal region of Bangladesh. A 1 m long handy geo-slicer was used to collecting samples for laboratory analyses and a gouge auger was used to measuring the thickness of different sedimentary units (Figure 5.1a). The samples were prepared for grain size, geochemical proxies, and diatom analyses to characterize the storm overwash deposits following Chapter 2.

In this work, lithofacies, mean grain size, sorting, geochemical proxies include TOC, TN, and $\delta^{13}C$ values, and diatom analyses have been carried out to gain a better understanding of the storm surge deposit in the southern coast of Bangladesh.

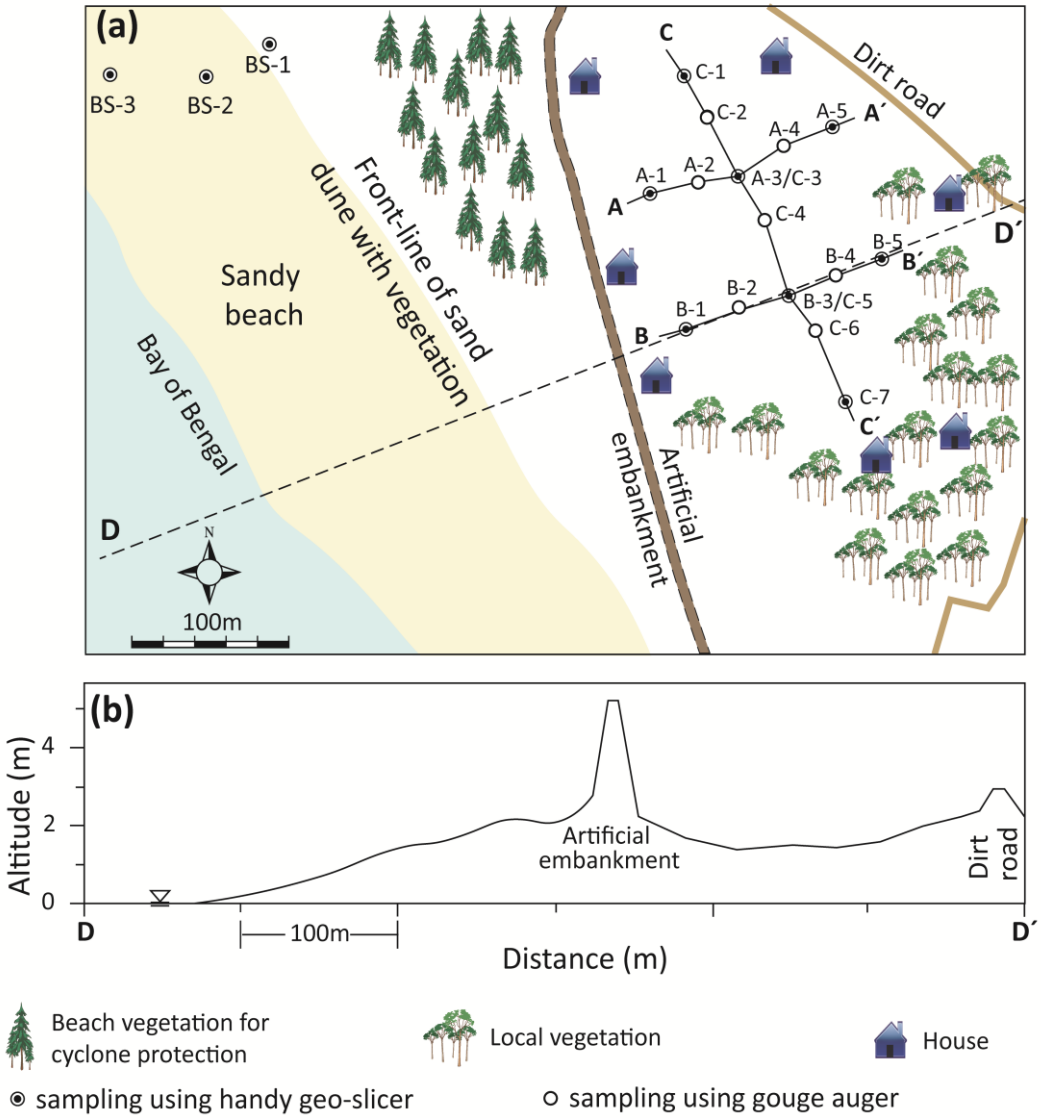

Figure 5.1: **(a)** Overview of the study area shows the location of the sampling sites along three adjacent transects A, B, and C (core coordinate showed in Table 5.1, Page 75; see Figure 1.1, Page 6 site location); and **(b)** Topographic cross-section along D-D´ (Haque et al., 2021).

5.2. Results

5.2.1. Sedimentary characteristics of cores

The up to 70 cm long geological core collected from fifteen sites situated at a distance of 135–277 m from the coast (Table 5.1) along with three transects (A–A′ and B–B′ perpendicular, and C–C′ parallel to the current shoreline) were studied (Figure 5.1). Based on the sedimentary facies, grain size distribution, and sedimentary structures, three sedimentary units were identified in the successions. The descriptions of the units are followed.

5.2.1.1. Unit A (bluish gray mud)

The massive or parallel laminated bluish gray unit containing up to 99% mud (20–26% clay, 73–79% silt) is observed at the bottom of the successions. The average mean grain size of this unit is ranging from 12–20 μm. This unit underlies Unit B and has root trace, plant fragments also noted with yellowish and carbonaceous layer (Figures 5.2–5.4).

5.2.1.2. Unit B (white to light gray sand)

White to light gray 1 cm to 17 cm thick sand unit overlies bluish gray mud (Unit A) with sharp to erosional contact (Figures 5.2–5.3, Table 5.1). This unit shows normal grading where massive sand with mud clast is found in the base and parallel laminae in the upper part (Figures 5.2 and 5.4). This unit shows one main group of particle populations with higher variability ranges between 90 μm and 256 μm for fine sand (Figure 5.4). The average mean grain size and sorting value of the unit range between 110 μm and 153 μm, and 0.90 φ and 2.24 φ, respectively (Table 5.1). The grain size of the unit gradually decreases and sorting values increase from bottom to top (Figure 5.4) whereas the average mean grain size and thickness of the unit decrease and the sorting value increase from the coast to inland (Figure 5.5).

5.2.1.3. Unit C (olive-gray sandy silt)

The lower part of this unit shows parallel laminae while the upper part exhibits massive structure. The root trace with grayish brown oxidized and organic rich layers have been found in the upper part of the unit. This unit shows normal grading and contains 59–67% mud (11–17% clay and 42–55% silt) and 33–41% sand grain. The grain size distribution shows a bimodal population with higher variability ranges between 4 µm and 40 µm, 90 µm and 256 µm, respectively. Mud content gradually increase in the upper part of this unit (Figure 5.6).

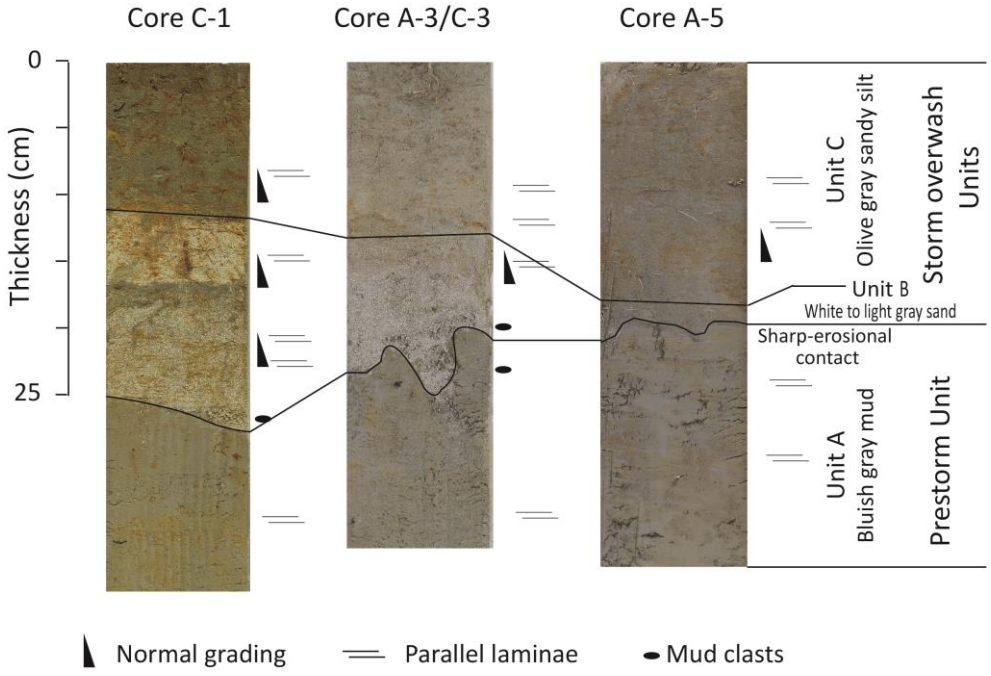

Figure 5.2: Photograph and sedimentary characteristics of cores C-1, A-3/C-3 and A-5 (Haque et al., 2021b). The position of the sedimentary cores shown in Figure 5.1, Page 72.

Table 5.1: Core coordinate, distance from the coast, thickness, mean grain size, and sorting value of each sand layer of unit B and modern beach sand (BS) of the study area.

Core ID	Coordinate		Distance from Coast (m)	Thickness (cm)	Mean Grain Size (μm)	Sorting (φ)
	Latitude	Longitude				
Transect A						
A-1	21.84039703	90.08906904	157	6	135.8	1.16
A-2	21.84046702	90.08935897	185	5	-	-
A-3	21.84048797	90.08959902	210	9	141.3	1.02
A-4	21.84066198	90.08988401	245	2	-	-
A-5	21.84076399	90.09017101	277	1	109.8	2.24
Transect B						
B-1	21.83964500	90.08928596	135	9	152.7	0.9
B-2	21.83977299	90.08960799	170	3	-	-
B-3	21.83982999	90.08990597	203	5	139	1.15
B-4	21.83993803	90.09019498	234	3	-	-
B-5	21.84002898	90.09046596	266	5	117.1	1.8
Transect C						
C-1	21.84104604	90.08927397	Parallel to the coastline (approximately 208m)	14	132	1.26
C-2	21.84082199	90.08941798		17	-	-
C-3 (A-3)	21.84048797	90.08959902		9	141.3	1.02
C-4	21.84024900	90.08976096		5	-	-
C-5 (B3)	21.83982999	90.08990597		5	139	1.15
C-6	21.83963603	90.09006296		3	-	-
C-7	21.83924401	90.09024200		2	123	1.13
Beach Sand						
BS-1	21.84119498	90.08666804	N/A	N/A	159.5	0.42
BS-2	21.84104302	90.08639999	N/A	N/A	221.6	0.96
BS-3	21.84105400	90.08581996	N/A	N/A	185.7	0.72

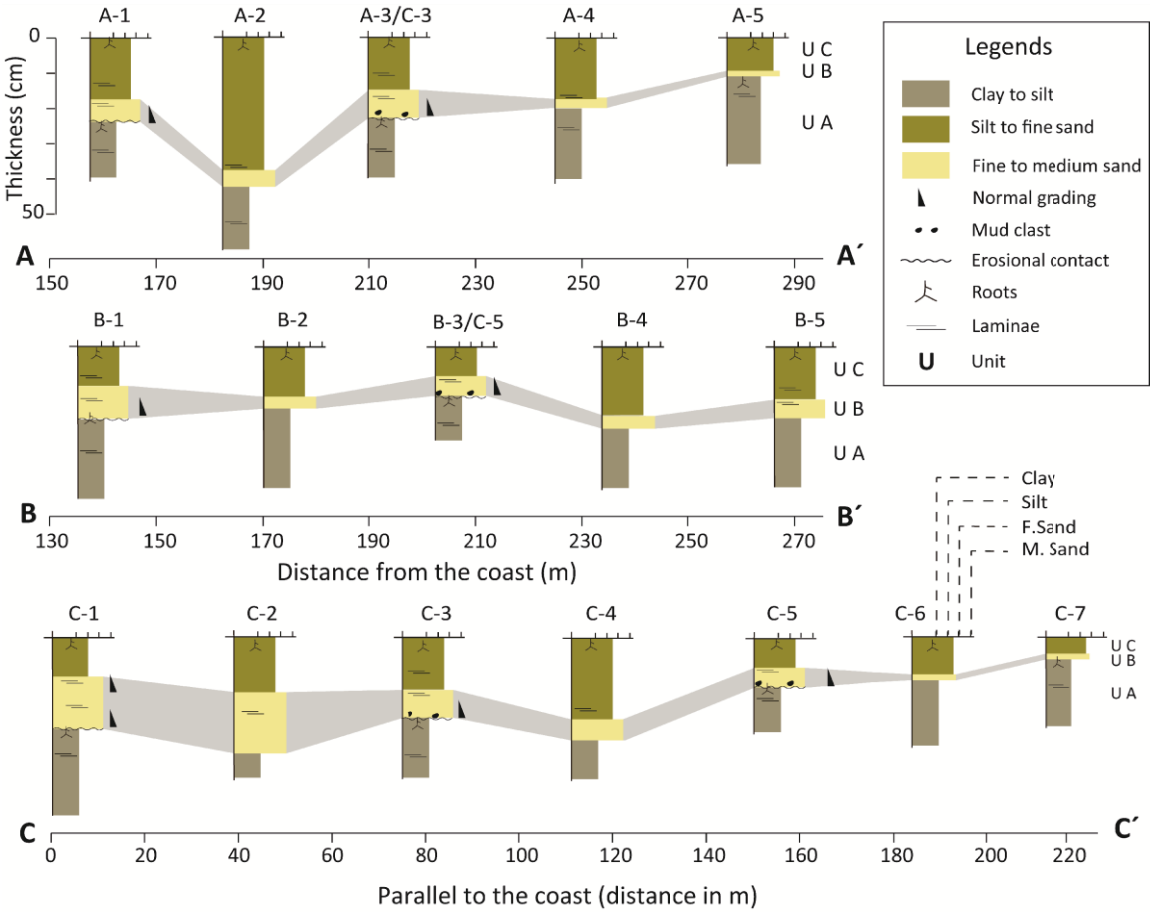

Figure 5.3: Sedimentary facies and structure of cores along with transects A, B, and C (Haque et al., 2021b).

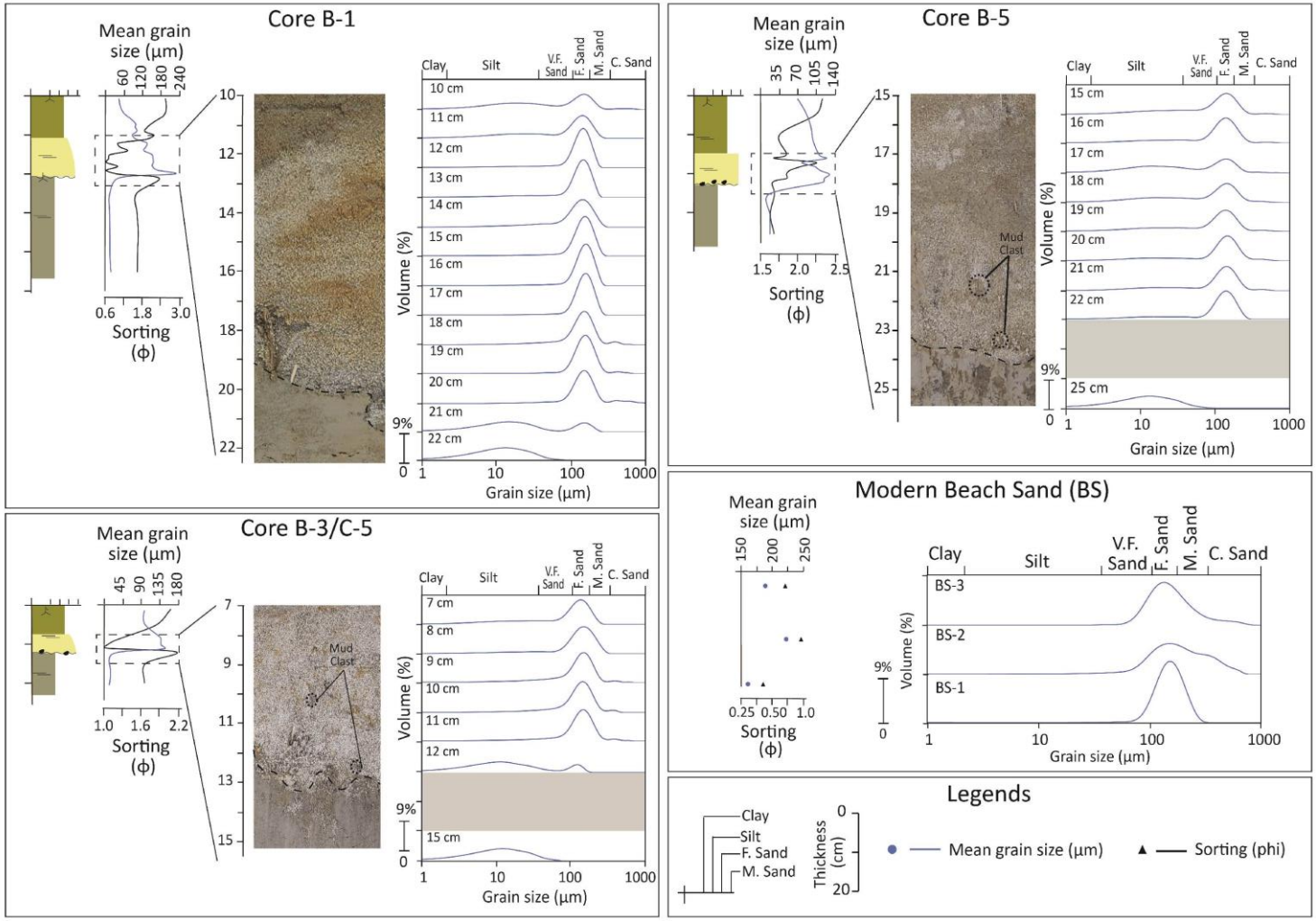

Figure 5.4: Mean grain size and sorting of cores B-1, B-3/C-5, B-5, and modern beach sand. The dotted area highlights the change of vertical distribution of grain size of unit B. The grain size distribution of modern beach sand (BS-1–3) is also shown (Haque et al., 2021b). Legends of sedimentary column see Figure 5.3, Page 76.

5.2.2. Geochemical characteristic of sedimentary units

The organic geochemical proxies including TOC, TOC/TN, and $\delta^{13}C$ values provide valuable tools for characterizing storm deposits (Das et al., 2013; Frappier, 2009; Lamb et al., 2006; Miller et al., 2006). The vertical distributions of these proxies show significant variation with depth in the sedimentary successions of the study area (Figure 5.7). The average TOC and TOC/TN values of the bluish gray mud (Unit A) ranges from 0.21%–0.29% and 7.5–9.3, respectively. The values show low in unit B where TOC value ranges from 0.14%–0.21% and TOC/TN ranges from 5.2–6.4. The concentration of average TOC and TOC/TN gradually increases in Unit C and ranges between 0.33% and 0.78%, and 8.9 and 11.1, respectively (Figure 5.7). The $\delta^{13}C$ values of unit A range between −21.69‰ and −20.41‰ whereas it shows high values in Unit B and ranges from –20.06‰ to –18.01‰. The $\delta^{13}C$ values gradually decrease and ranges between –22.83‰ and –19.43‰ in Unit C (Figure 5.7).

5.2.3. Fossil diatom assemblages

Diatom assemblages present as a percentage of the total count of diatoms and their ecological groups, namely freshwater, brackish, and marine habitat (Jones, 2007; Round et al., 1990). The species with large valves seem to be broken within the samples. Based on the vertical distribution of diatom assemblages, it can be divided into two zones– A and B (Figure 5.8). The freshwater diatom *Navicula cryptotenella,* brackish diatoms *Fragilaria brevistriata*, *Fragilaria fasciculata*, *Nitzschia clausii,* and marine diatoms *Delphineis surirella and Raphoneis cf. rhomboides* are abundant in Zone A (Unit A). The shallow marine diatoms *R.* cf. *rhomboides* and *Navicula ingrata,* brackish diatoms *Navicula halophila* and *Navicula phyllepta,* and freshwater *Eunotia subarcuatoides*, *Navicula cryptotenella*, *Navicula subminuscula* diatoms are abundant in the sand and sandy silt sediment of Zone B (Unit B and C).

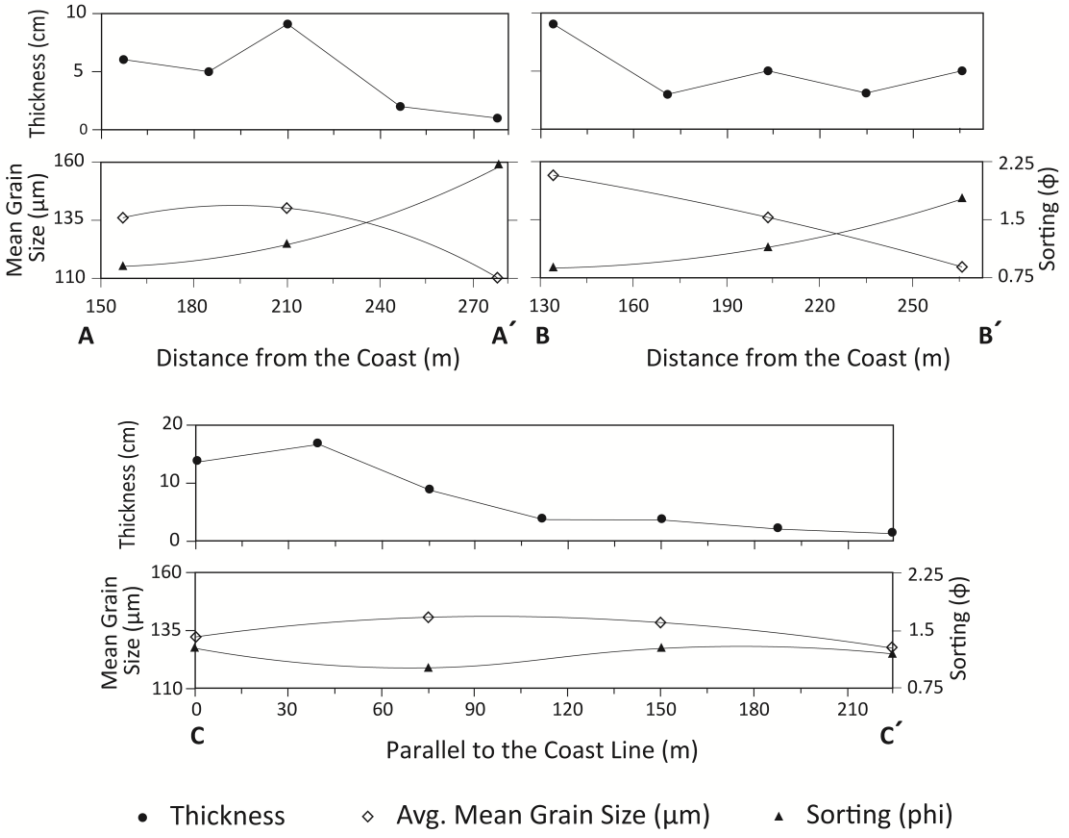

Figure 5.5: Lateral trend of thickness, mean grain size, and sorting of unit B along the transects A–C (Haque et al., 2021b).

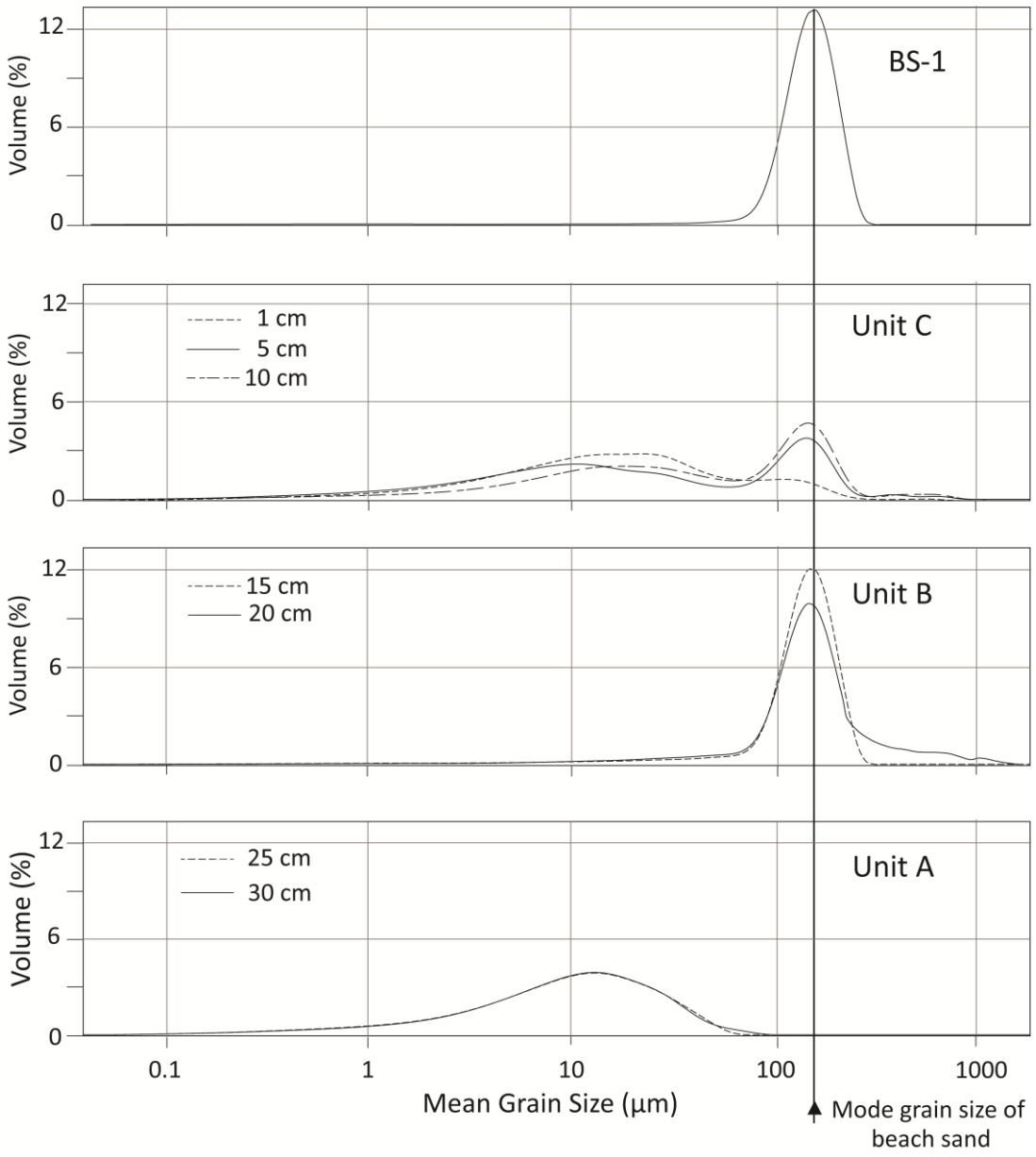

Figure 5.6: Comparison of the grain size distribution of among sediment of unit A–C of core B-1 and BS-1 (Haque et al., 2021b).

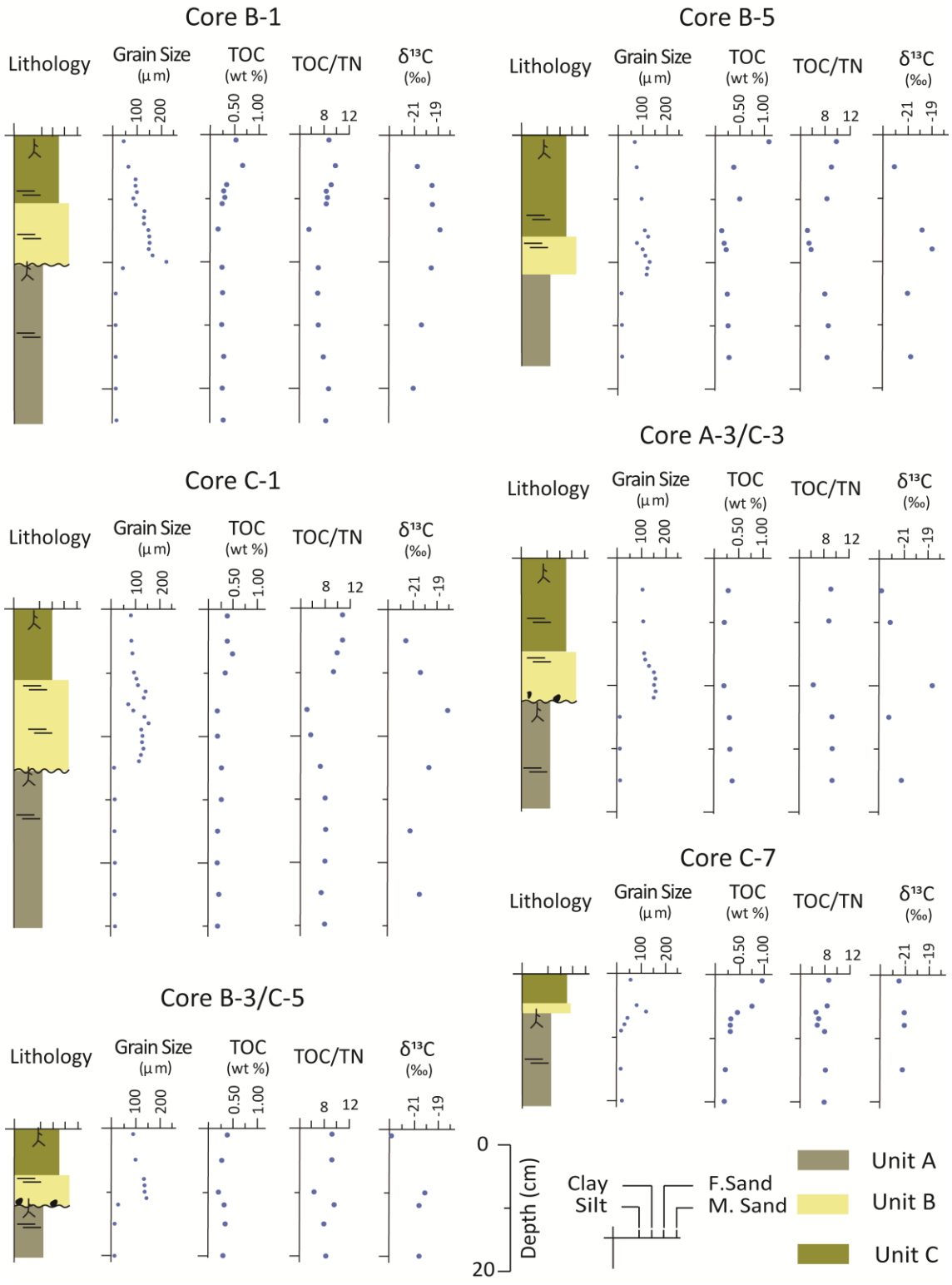

Figure 5.7: Vertical distribution of mean grain size, TOC, TOC/TN, and $\delta^{13}C$ values of B-1, B-5, C-1, A-3/C-3, B-3/C-5, and C-7 (Haque et al., 2021b). Symbols of sedimentary column see Figure 5.3, Page 76.

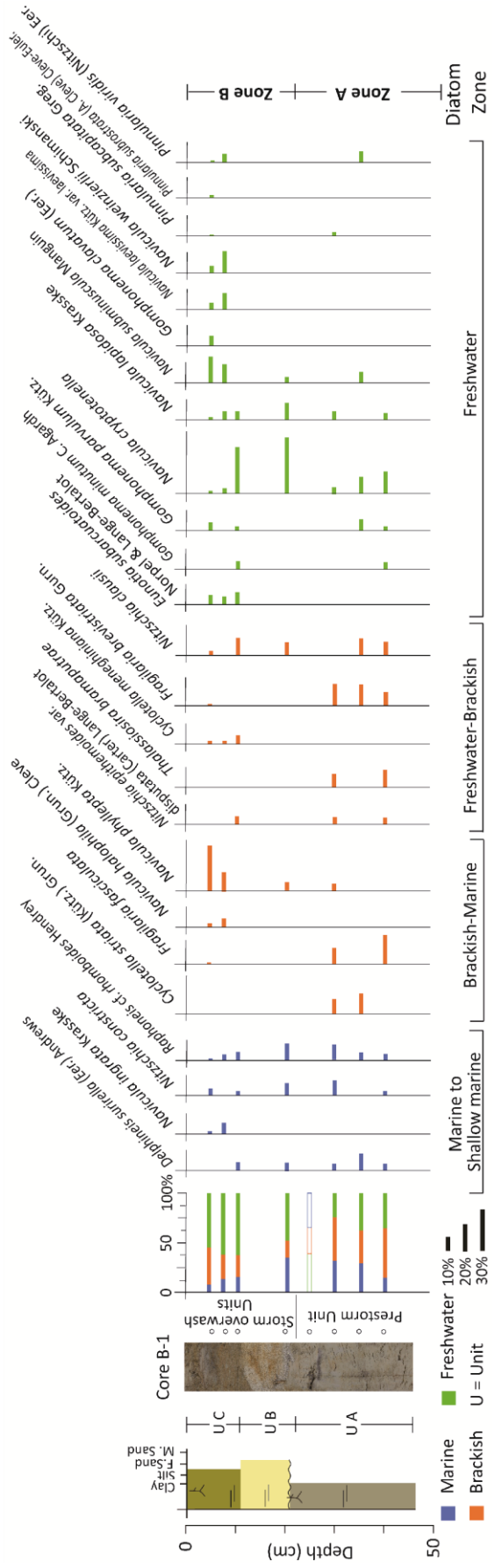

Figure 5.8: Fossil diatom assemblages of core B-1. The color coding for the sediment is shown in Figure 5.3, Page 76 (Haque et al., 2021b).

5.3. Discussion

5.3.1. Sediment sources

The sedimentary facies, grain size distribution, geochemical proxies and diatom assemblages have been considered to identify the sources of sediment of storm overwash deposits. The modern beach over the study area is covered by fine to medium sand which is coarser than the sediment composition of the surrounding land and riverbank. The grain size suggests that the wave force played an important role in developing the sandy beach on the Kuakata coast (JSCE, 2008). Most of the sediment of the GBM estuary is transported during the months of monsoon. The mean grain size for suspended rivers sediment was approximately 6.5 φ (11.1 μm) and sediment concentration reached as high as 2000 ppm were reported by Datta and Subramanian (1997) and MES II (2001). TOC/TN value of marine sediment ranges between 3 and 10, whereas it shows above 15 of terrestrial sediment (Watson and Whitefield, 1985; Meyers, 1997). The $\delta^{13}C$ values of marine and terrestrial sediment ranges between –18‰ and –22‰, and –25‰ and –28‰, respectively (Lamb et al., 2006; Prasad et al., 2017; Ray and Shahraki, 2016; Sarkar et al., 2009).

The mud of Unit A contains plants and/or root trace with parallel silty sand laminae. The sedimentary facies, TOC/TN, and $\delta^{13}C$ values of Unit A indicate a lower delta mud plain environment where marine/tidal water column is the major contributor of organic matter in the sediment (Figures 5.7−5.8). White to light gray sand (Unit B) has been found overlies the mud unit during field investigation for the study (Figures 5.1–5.2). The grain size distribution of Unit B is comparable with the modern beach sand (Figures 5.4 and 5.6). The mean grain size and thickness of the unit decrease from the coast to inland and the sorting values increase (Figure 5.5), indicating sand grains were sourced from the seaward (Brill et al., 2016; Soria et al., 2017). The negative shift TOC, TOC/TN in conjunction with positive excursions in $\delta^{13}C$ values indicate marine influences of severe storm events during deposition of Unit B (Figure 5.7; Das et al., 2013; Lambert et al., 2008). The abrupt change of sedimentary facies, grain size

distribution, geochemical proxies are showing between units A and B indicates a sudden increase of sediment supply from the seaward during Cyclone Sidr. Unit C shows bimodal grain size distribution and the particle population densities interpret as the sediments are mixing of two different sources (Figure 5.6). The variability between 90–256 μm fine grained sand is sourced from the beach sand whereas muddy sediment came from the suspended and nearshore deposits of the bay, and also likely carried from the suspended river's sediments that flooded the area during landfall of the storm. The TOC and TOC/TN values gradually increase, and the decrease of $\delta^{13}C$ values in Unit C indicates the input of some terrestrial sources of organic matter and/or the post-depositional changes due to productivity of couch grass after the deposition of the sediments (Figure 5.7; Das et al., 2013).

The sediment of Unit B exhibits that the grain size distribution is dominated by fine to medium grained sand with a small quantity of mud particle, and it grades into bimodal grain size distribution dominated by silt (4–40 μm) and fine sand (90–256 μm) at Unit C (Figure 5.6). The cluster highlighted in Figure 5.9 clearly distinguishes the overwash storm deposits (Unit B and C) and tidal mudflat sediment. The diagram failed to show a clear similarity between modern beach sand and Unit B. It is probably caused by the intrusion of mud particles with beach sand during transportation and sorted by storm waves during deposition.

Rivers and rain of the GBM delta system trigger a large input of freshwater into the sea and have delivered land derived or terrestrial nutrients along the coast. The upstream water dominantly discharges through the GBM estuary during monsoon and post-monsoon season (Figure 1.1; Dai and Trenberth, 2002). The coastal surface current disperses freshwater to the southward and gradually mixing with saltier waters below (Behara and Vinayachandran, 2016; Benshila et al., 2014) and creates low salinity at the sea surface near the coast (Felton et al., 2014; Vinayachandren et al., 2002). Diatom assemblages of Zone A of core B-1 dominated by freshwater–brackish to brackish–marine species. The presence of *F. brevistriata, F. fasciculata* in Zone A indicates a brackish mudflat environment for Unit A where presence of *D. surirella*

with silty sand laminae reflected that the area was affected by ocean tide during the deposition of the sediments (Figure 5.8). The combination of river/bogs origin freshwater *N. subminuscula* and *E. subarcuatoides,*and brackish–marine *N. phyllepta*, *N. ingrata and R.* cf. *rhomboides* diatoms dominantly found at Zone B in the upper part of core B-1 (Figure 5.8). Facies changes and presence of brackish–marine diatoms with fluvial freshwater diatoms indicate sudden environmental change and/or thickening of sediment over the study area during a storm surge. Cyclone induced storm surge carried brackish–marine diatoms from the bay and heavy rainfall for that flooded adjacent river which carried river/bogs origin freshwater diatoms and deposited at the sampling site during landfall of the storm (Wang et al., 2019).

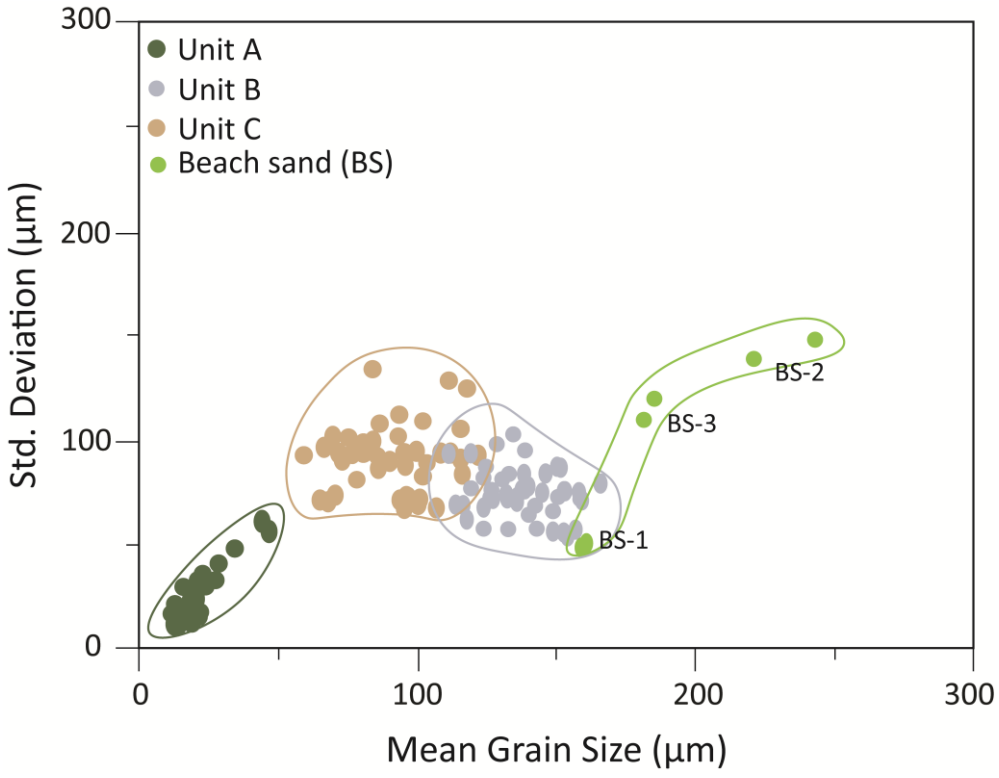

Figure 5.9: Bivariate plot of mean grain size and standard deviation of grain showing distinct clusters on sediments of unit A–C and modern beach sand (modified after Haque et al., 2021b; Switzer et al., 2005; Switzer, 2013).

5.3.2. Depositional model for storm deposit

The storm deposit found behind the embankment in the west Kuakata shows a unique characteristic that allows developing a depositional model for storm overwash deposits from the southern coast of Bangladesh. Kuakata coast seems to be one of the areas which were suffered by the 2007 Cyclone Sidr (Figure 4.1a; Shibayama et al., 2009). Harris (1963) mentioned several reasons that cause the rising water level during a storm, such as earth's rotation, pressure, wind direction, wave, and rainfall. The storm creates an abnormal rise of water over the astronomical tide. The high concentration of suspended sediments is formed near the coast of GBM delta where the water depth is less than 5 m, and the sediments at that depth resuspended due to tidal force and coastal current of the area (Barua, 1990). The storm, especially cyclone events are very effective in mobilizing and transporting the nearshore sediment onto the low-lying coastal plains (Hawkes and Horton, 2012; Leatherman, 1981; Morton and Sallenger, 2003; Williams and Flanagan, 2009). Tide-modified current, wind-induced and strong storm surge help moving the suspended sediment-rich water masses both inland and shallow shelf in various directions depending on the position of cyclone gyre (Chang et al., 2001; Kim et al., 2008; Miles et al., 2015). Many dunes and landmasses of the coast are completely washed away in the coastal area during the storm effect of Sidr (Hanebuth et al., 2013; Shibayama et al., 2009).

The shoreface adjacent to Kuakata has a gentle slope and low wave energy that form fine to medium grained sand beaches (Figures 5.1 and 5.4). Large scale cyclone events that normally move from south to north form large swells in the Bay of Bengal, this phenomenon causes high energy conditions and forms a disequilibrium in the marginal coastal environment in Bangladesh. Eroded sediment from temporally settled nearshore muddy deposits, beach face and dune system are the main sources of storm deposit at Kuakata. Heavy rainfall during cyclone events also flooded adjacent areas of the bay that carried fluvial sediment. The eroded sediment moves gentle slope to a steeper canyon wall of Swatch of No Ground of the Bay of Bengal (Figure 1.1) (Kudrass et al., 2018) and is also carried toward inland low lying delta coast during the landfall of the storm.

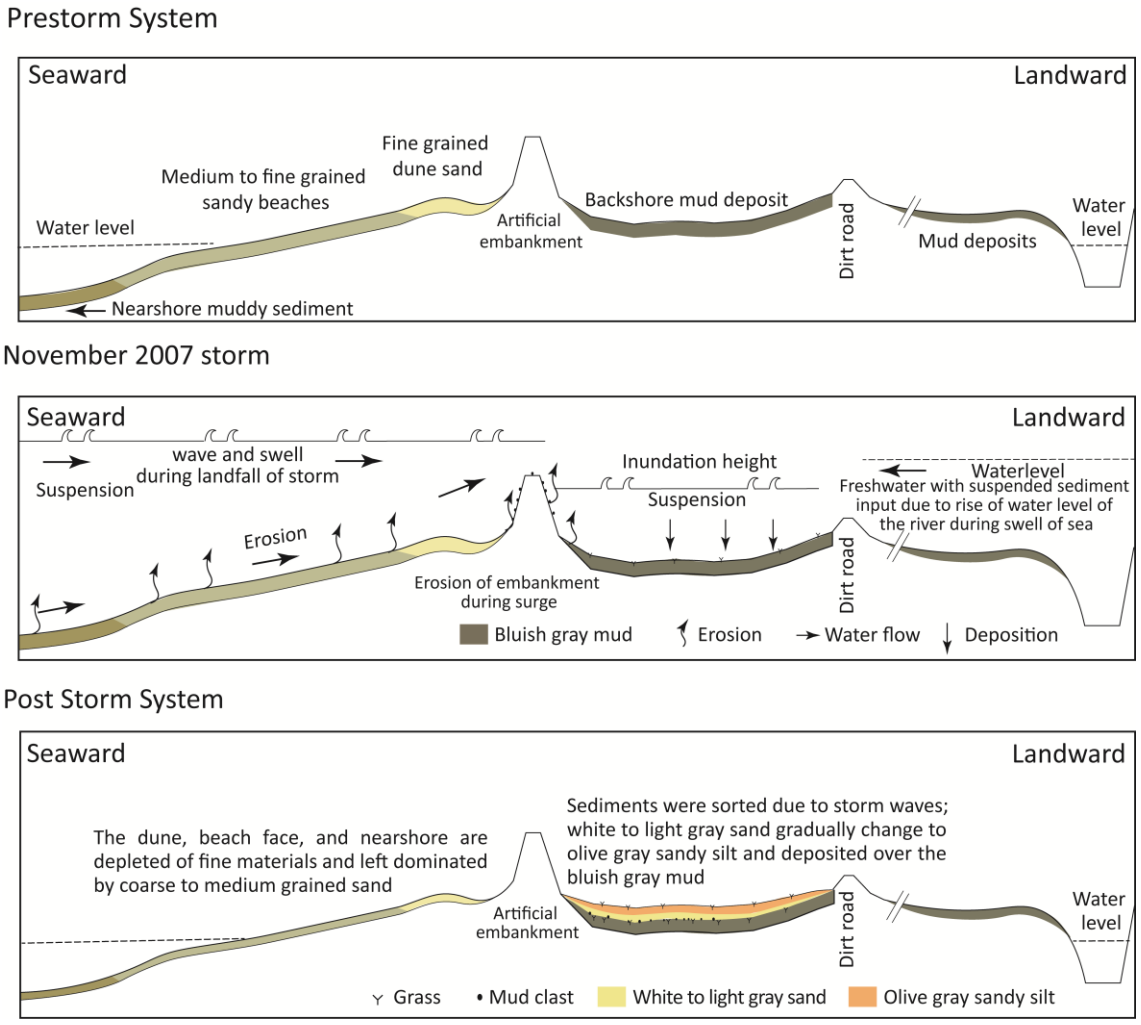

Figure 5.10: Schematic depositional model for the storm deposits at West Kuakata, Bangladesh (Haque et al., 2021b).

Table 5.2: Comparison of the sedimentary signatures and microfossil analyses of the Cyclone Sidr storm surge and other recent storms deposits.

Name of storm surge			**Cyclone Sidr**	**Cyclone Bulbul**	**Typhoon Haiyan**	**Typhoon Haiyan**
Event date			Nov. 2007	Nov, 2019	Nov. 2013	Nov. 2013
Study location			Kuakata, Bangladesh	Haringhata coast, Barguna, Bangladesh	Tanauan, Leyte, Philippines	Basey, Samar, Philippines
Coastal morphology			Sandy beach, low elevated riverine deltaic coast	Very fine sand beach, low elevated riverine deltaic coast	Sandy beach, coastal plain	Carbonate−siliciclastic sandy beach
Ground surface elevation of study area			Appx. 5 m at crest of embankment. Tidal mud flat up to 1.5−2.0 m.	1.5−2 m	1.5−2 m	2−3 m
Intensity at landfall			Cat-4 (appx. 250 kph), 944hPa	Cat-2 (appx. 120 kph)	Cat-5 (appx. 296 kph), 895 hPa	Cat-5 (appx. 296 kph), 895 hPa
Maximum inundation level (asl)			More than 6 m	Less than 3 m	5 to 6 m	5 to 6 m
Sedimentary texture and Structure	**Trench scale**	**Thickness**	5 cm to 55 cm	2 cm to 5 cm	2 cm (distal) to 10−20 cm (proximal)	2−8 cm
		Vertical change in grain size	Unit 1: white to light gray normal graded sand. Unit 2: olive gray normal graded sandy silt. It shows bimodal grain size distribution dominated by silt (4–40 µm) and fine sand (90–256 µm).	Not analyses	Unit 1: sand sheet to mud, coarsening upward sequence Unit 2: washover terrace, coupled fining and coarsening upward sequence	Not reported
		Sorting	Moderate to poorly sorted	Moderate to poorly sorted	Moderate to well sorted	Poorly sorted
		Sedimentary structure	Unit 1: massive or parallel laminae Unit 2: Parallel laminae but change to massive at upper part	Massive or parallel laminated	Unit 1: massive to horizontal laminae Unit 2: sub horozontal laminae	Massive
		Basal contact	Sharp to erosional	Sharp	Sharp to depositional	Sharp to depositional
	Transect scale	**Cross shore geometry**	Unit 1: landward thinning trend Unit 2: highly variable thickness	Landward thining trend.	Washover terrace (proximal); sand sheet to mud (distal) with varying thickness landward but generally thick in depression.	Overall but not systematic landward fining
		Lateral grading	Unit 1: landward fining trend Unit 2: no systematic trend found in this unit	Landward fining trend	Overall landward fining	Overall landward fining
		Inland extent	305 m	225 m	1.6 km	350 m
Microfossil description			Diatom assemblages separated the pre-storm and storm overwash sediments. Storm overwash sediments contained both river/bogs origin freshwater and marine diatoms. The presence of brackish-freshwater diatoms are comparatively higher at the upper part of deposits than the marine diatoms.	Relatively abundance of marine–brackish diatoms found at surficial sediment towards the sea and is gradually change to brackish–freshwater dominated in landwards.	Presence of intertidal and subtidal benthic, and planktic foraminifera differentiated the underlying and overwash sediments. Planktic foraminifera are highest in the overwash sediments closest to the shoreline (20 m from the shoreline), and lowest at inland sites (from 440–890 m).	Concentrations of foraminifera are highest at sample sites closest to the shoreline and begin to markedly decrease beginning at 100 m inland from the coast. Foraminifera were absent at pre-Haiyan soil.
References			(This study) Haque et al., 2021b	(Chapter 4) Haque et al., 2021a	Pilarczyk et al. (2016), Soria et al. (2017)	Pilarczyk et al. (2016), Soria et al. (2017)

Table 5.2: (Cont.).

Name of storm surge			Typhoon Haiyan	Cyclone Yasi	Hurricane Ike	Hurricane Rita
Event date			Nov. 2013	Feb. 2011	Sept. 2008	Sept. 2005
Study location			Hernani Beach, Philippines	South of Caims, northeast Queensland, Australia	Galveston and SanLuis island, Texas, USA	Constance Beach, Louisiana, USA
Coastal morphology			Pleistocene reef, gentle slope sand coast	Sandy beach ridge plains	Ridge and swale topography, Barrier Island	Beach ridges, separated by low lying muddy marshes
Ground surface elevation of study area			Ridge crest 2.2 m (50 m from coast) − 2.6 m (230 m inland)	Ridge crests at higher then 4-5 m	0.75−2.2 m	0.50−2 m (ridges)
Intensity at landfall			Cat-5	Cat-5	Cat-2 (appx. 175 kph)	Cat-3 (appx. 190 kph)
Maximum inundation level (asl)			2.5 to 5.0m	3 to 6 m	2.7 to 3.7 m	4 to 5 m
Sedimentary texture and Structure	**Trench scale**	**Thickness**	2−20 cm	5−50 cm	2−28 cm	2−50 cm
		Vertical change in grain size	Unit 1: normal graded, massive to laminated fine to medium sand Unit 2: bi-modal grain size distribution, significantly coarser than Unit 1 found at landward	Fining upward with fine skewed trends	Alternate coarsening to fining upward; coarsening upward sequence	Unit 1: coarsening upward sand sheet Unit 2: coarsening upward washover terrace
		Sorting	Poorly sorted	not reported	not reported	well sorted
		Sedimentary structure	Massive to laminated structured	Horizontal lamination. Basal part dominated with coarse grain sand and grain size gradually decrease at upward.	Laminated structure found at x-ray	Unit 1: planner to horizontal laminae Unit 2: prominent foreset laminae
		Basal contact	Erosional	Sharp to erosional	Sharp to erosional	Sharp to erosional
	Transect scale	**Cross shore geometry**	Overall landward thinning trend	Highly variable thickness	Landward thinning trend, thicker deposit found at swale	Landward thinning
		Lateral grading	Unit 1 shows landward fining trend but comparatively coarser grained sediment found in Unit 2 that deposited at landward.	Lateral fining in one site. No systematic trend in another site	Not reported	Fining towards inland
		Inland extent	220 m	Up to 87 m	Up to 320 m	At least 500 m
Microfossil description			Foraminifera assemblages reflects significant reworking of sediment during deposition. The *Amphistegina Sp*. Gradually decrease in upperpart of storm deposits.	Marine to marine−brackish diatoms found with freshwater diatoms. High percentage marine diatoms found at seaward, and percentage of freshwater diatoms increased at land ward.	Foraminiferal assemblages of overwash deposits are common to bay and nearshore environments along coast of Gulf of Mexico. Presence of *E. albumbilicatum, B. subaenariensis* reflect slightly deeper excavation and transport than solely nearshore provenance.	Concentration of foraminifera higher in seward and gradually decrease towards land.
References			Brill et al. (2016)	Nott et al. (2013)	Hawkes and Horton (2012)	Williams (2009)

Local topography and geomorphology significantly controlled depositional process during the storm events (Table 5.2). The intensity of surge wave and sources of the storm sediment significantly controlled the inland extension of the storm deposits (Hawkes and Horton, 2012; Williams, 2010). The overwash sediments deposited due to cyclone Sidr have two units that are mixed of silt (4–40 μm) and fine sand (90–256 μm) (Figure 5.6). Overall the units have massive or parallel laminae and fining upward sequence (Figure 5.7). The two units of storm deposits can be formed due to multiple wave arrivals (e.g., Sedgwick and Davis, 2003; Soria et al., 2017; Switzer and Jones, 2008) or different inundation heights (e.g., Hawkes and Horton, 2012; Williams, 2009) or sediment carried by different sources, sorted according to storm wave and different settling velocities (e.g., Brill et al., 2016; Hong et al., 2018; Shigeno and Nanayama, 2016). The grain size distribution, texture, and composition of sediment of Unit B are comparable to modern beach sand and dune of the Kuakata coast (Figures 5.4 and 5.6). The unit shows normal grading as well as landward fining and thinning trends (Figures 5.5–5.6). These characters normally show in modern overwash deposits (e.g., Hawkes and Horton, 2012; Horton et al., 2009; Morton et al., 2007; Nott et al., 2013; Shigeno and Nanayama, 2016; Soria et al., 2017; Switzer and Jones, 2008; Williams, 2009). Presence of multiple layers/parallel laminae in storm deposits have been appeared widely in various reports (e.g., Brill et al., 2016; Phantuwongraj et al., 2013; Shigeno and Nanayama, 2016; Soria et al., 2017; Switzer and Jones, 2008). The maximum inland extension of sand layers depends on storm's inundation height and roughness of depositional surface. Local topography and grain size of sourced sediment also affect the inland extension of storm deposits (Watanabe et al., 2017).

Gradational contact was observed between units B and C (Figure 5.2). Bimodal Unit C has mixed sediment of fine sand and silt (Figure 5.6) and showed normal grading in sequence (Figure 5.7). Both marine and freshwater diatoms are found at storm overwash deposits. The presence of brackish-freshwater diatoms is comparatively higher than the marine diatoms at the upper part of deposits (Figure 5.8). The grain size and diatom assemblages referred that the sediment was deposited by a cyclone that were brought by both the storm surge into the bay and overbank river flooding to the coastal area. Heavy rainfall caused overbank flooding which

carried suspended sediment and river/bogs origin diatoms to the coring site. Such type of diatom assemblages was observed in a paleohuricane overwash deposit formed in 1772 AD at Weeks Bay of Alabama (Wang et al., 2019). Long duration of sedimentation (~5–7h) causes thicker overwash storm deposits mainly when storm is near to the coast. Several thousand waves formed during a tropical cyclone transported eroded sediment, and also help to sorted and formed laminae during deposition (Morton et al., 2007; Phantuwongraj et al., 2013; Watanabe et al., 2017).

The inherited sediment features are apparent in the storm deposit studied here. The Sidr overwash deposits found at Kuakata coast of the Bay of Bengal represent different sedimentary processes compared to modern overwash deposits (Table 5.2). It might have caused due to different geographic setup and sediment sourced characteristics of storm deposits. The depositional process involves during the storm event has been illustrated in Figure 5.10. The nearshore sediments, beach sand, and dunes were eroded due to the high energy of wind and large swell (more than 6 m above normal astronomical tide) during landfall of Sidr (Hasegawa et al., 2008; JSCE, 2008; Shibayama et al., 2009). The white to light gray sand (Unit B) shows a massive structure with mud clasts (burial soil clast or eroded from embankment) at the base and parallel laminae in the upper part of the unit. The unit grades into olive-gray sandy silt (Unit C) in the upper part of the deposits. High intense precipitation before/during the landfall of a storm, causes a large discharge of water to the bay through the adjacent river. Cyclone induced storm surge can increase water levels of the river downstream boundary that, in turn, cause severe flood during cyclone events (Teng et al., 2017). The Kuakata bay holds and carries the heavy suspended sediment. The waves generated by cyclones produce turbulence during passage over the inner shelf of the coast. The surging water transported the suspended sediment from the bay, and also reworked and eroded fine materials of nearshore, beach face, and dune. Suspended mud additionally carried by the rivers that flooded the area due to subsequent heavy rainfall during storm. Transported storm overwash sediments were sorted by storm waves showed normal graded sedimentary sequence and Unit B and C settled over the study area (Figure 5.10).

5.4. Conclusions

The deposits of Cyclone Sidr are strongly influenced by geomorphology and sediment characters around the depositional site on Kuakata coast of the GBM delta. The deposits present the hydrodynamics interaction of bay water and river/fluvial flood during a storm surge. The processes involved in sedimentation are summarized. Two distinct sedimentary assemblages (Unit B and C) have been formed due to flooding of the coast and storm overwash deposits overlaid the backshore bluish gray tidal mud (Unit A). Massive or parallel overwash normal graded sand (Unit B) that dominated at the base of the storm deposits overlies Unit A sharp to erosionally. The unit shows landward fining and thinning trends, and grain size distribution is similar to modern beach sand implies that the sediment sourced from seaward at the present geographical setup. The unimodal sand grades into bimodal sandy silt (Unit C) in the upper part of the deposits. The grain size distribution and diatom assemblages of storm deposits suggested that the sand (90–256 μm) was sourced from the beaches/dunes and mud (4–40 μm) carried from both the suspended and nearshore sediment of the bay and adjacent river. The combination of brackish–marine diatoms with freshwater river/bog origin suggested that inundation of storm surge occurred simultaneously with overbank river flooding due to intense precipitation during cyclones. Waves occurred due to stormwind sorted the overwash sediment and showed normal graded, massive to parallel laminated depositional sequence. Cyclone Sidr deposit represents extreme storm surge sediments that exhibited distinctive flooding characters on a global scale. The finding contributes to understand the complexity of the geomorphology of the low-lying riverine GBM delta and the hydrodynamic process that interacted with the fluvial and storm surge processes during cyclone flood events.

CHAPTER 6

Synthesis

The GBM rivers formed one of the largest delta systems in the world. The fluctuation of sea level influenced the depositional environment and sedimentation in the low-lying southwestern GBM delta of Bangladesh. Five sedimentary facies up to 250 cm thick have been identified in eight litho-sections along the north-south transect in the upper (landward) and lower (seaward) delta plain of Khulna district. Sedimentary facies, geochemical proxies, and diatom assemblages of these successions are discussed in Chapter 3. Generally, these analyses have been used to characterize the sources of organic matter and describe the depositional environment. The altitude of every sampling point, geometric position and radiocarbon age of selected samples have been represented the vertical and lateral variation of sedimentary facies and the effects of sea level on sedimentation over the area.

A noticeable effect of RSL change has been found on depositional environment and sedimentation in the low-lying delta basin during the last 1000 years of Holocene. After evaluating the result, records of global sea level and climate change (Abu-Zeid and Bantan, 2015; Mann et al., 2009; Nunn, 1998; Ota et al., 1990; Warrick and Ahmed, 1996), the sediments of these successions were deposited in three stages. Bioturbated light yellow to gray mud of deeper part at the upper delta plain was deposited under tidal influence during Stage I (850 AD – 1300 AD). The sea level is shown comparatively higher than the present level (up to 80 cm) in this stage. During Stage II (1300 AD – 1850 AD), the sea level descended up to 110 cm from the present, and the organic-rich bluish gray mud, brackish mangrove peat and terrestrial influenced yellowish-gray mud were deposited successively in seaward. The terrace or non-depositional surface was formed at landward due to the decline of base level in this stage. The rising trend of sea level was found after 1850 AD at Stage III (1850 AD to present). The influences of both terrestrial and coastal flood sedimentation increased due to newly formed inundation in this stage. The terrestrial flood sediment deposited over the tidal sediment in landward and tidal sediment from seaward gradually onlap upon it (Figures 3.6−3.7, 6.1). The sedimentation, subsidence, and eustatic sea level have influenced the RSL that shifted the depositional environment over the southwestern delta system of Bangladesh. Relative changes in sea level and way of sediment supply have influenced the sedimentation process over the study area.

The effect of present sea level rise, storms and sediment supply characteristics on coastal morphology and sedimentation at the river mouth in the lower delta plain of the southwestern GBM delta coast have been described in Chapter 4. Satellite images for four different vintages and geological cores from the Haringhata coastal region have been used to explain the sedimentation processes. The analyses of satellite images showed that the southern coastline (seawards) of the area permanently lost its landmass where the coastline advanced along the west and east (landward). The overall erosion and accretion ratio is 0.29 during the period 1977 to 1989, while the ratio is higher and ranges between 2.90 and 4.77 in the different intervals of Satellite images from 1989 to 2020. The morphological changes of the study are comparable to the overall southwestern coast of the GBM delta described by Rahman et al. (2011), Sarwar and Woodroffe (2013), Bandyopadhyay (2019), and Bhargava et al. (2020). The sedimentary facies and geochemical proxies of geological cores indicate that the bluish-gray mud facies deposited in a tidal environment and marine water is the source of the organic matter of the deposits. The increase of TOC, TOC/TN, and decrease of $\delta^{13}C$ values in the upper part of the mud facies reflected that the mangrove forest gradually covered the area. Parallel stratification to HCS, gray to white gray silty sand facies overlies the mud with sharp contact. The normal bedding is found in silty sand facies. Declined grain size from coast to inland and increased sorting value of the surficial sediment indicate that the beaches were the likely source of silty sand dominated facies. The relative abundance of marine–brackish diatoms in seaward gradually changed to fresh–brackish in landward indicate the sediments were probably sourced from seaward and the land-derived sources also incorporated with storm overwash deposits during deposition. Sedimentary structure and decrement value of TOC and TOC/TN and increment value of $\delta^{13}C$ in silty sand facies indicate the tropical storm surge events during deposition of the silty sand.

The coastal dynamics at the river mouth depend on accommodation space created due to RSL change and sediment supply ratio. Overall changes of the area were balanced from 1977 to 2020 but the area permanently lost its landmass during the last 30 years (1989–2020) and sedimentation took place towards land under marine influences. The sediment supply of the

GBM river system was significantly reduced up to 50% from the previous measurements (Rahman et al., 2018). The river flow connected to the mainstream of the Ganga gradually decreased following the construction by the Indian Government in 1975 of the 'Farakka' barrage (River dam) (Islam and Gnauck, 2009; Mirza, 1998, Winterwerp and Giardino, 2012). The wave height and direction over the coast did not change significantly for the last few decades. Hence, not only the wave and current energy, but the decreased upstream water flow and RSL rise also significantly controlled the coastal dynamics and sedimentation process of the area. The southwestern coast is accreted vertically due to storm events could maintain coastal elevation but decline inversely from the seaside due to RSL rise and deficit sediment supply from upstream (Figure 4.12). Coastal erosion and accretion of southwestern GBM delta coast get high water influences due to sea level rise, and waves, tides and storm surges which led to rework and redeposited the eroded sediment (Figures 4.12 and 6.1).

The characteristics, sediment sources, and depositional process of storm deposits formed by the 2007 Cyclone Sidr at Kuakata have been examined in Chapter 5. Fifteen geological cores at a distance of 135–277 m from the coastline along with three transects were analyzed to gain a better understanding of storm deposits in the southwestern GBM delta coast of Bangladesh. Three sedimentary units up to 70 cm thick were identified during field investigation. The massive or parallel, bluish-gray mud units underlies the storm overwash deposits. Geochemical proxies and presence of *Frafilaria brevistriata* and *Frafilaria fasciculata* diatoms in these units indicate a tidal mudflat environment and the presence of *Delphineis surirella* with silty sand laminae revealed that the area was flooded by ocean tide during the deposition of mud. Up to 17 cm thick normal graded unimodal white to light gray sand found at the bottom of the storm deposits overlies the mud sharp to erosionally. Declined the thickness and grain size of the units from coast to inland and increased the sorting value indicate that the sand was sourced from seaward. The negative shift of TOC and TOC/TN, the positive shift of $\delta^{13}C$ values, and the presence of *Raphoneis* cf. *rhomboides* and *Navicula ingrata* diatoms indicates a severe storm surge during deposition of sand. The grain size distribution of the sand unit is very similar to

modern beaches reveals that the beaches were the probable source of sand. Unimodal sand unit grades into bimodal olive gray sandy silt in the upper part of the storm overwash deposits. The unit also showed a fining upward sequence. Normal graded, landward fining and thinning trends and presence of multiple layers/parallel laminae in storm overwash deposits have appeared widely in various reports (e.g., Brill et al., 2016; Hawkes and Horton, 2012; Horton et al., 2009; Morton et al., 2007; Nott et al., 2013; Phantuwongraj et al., 2013; Shigeno and Nanayama, 2016; Soria et al., 2017; Switzer and Jones, 2008; Williams, 2009). The grain size distribution and presence of freshwater diatoms of *Eunotia subarcuatoides*, *Navicula cryptotenella*, *Navicula subminuscula* with brackish to marine diatoms demonstrate that the sand grained sediment sourced from beaches, and muddy sediment from the suspended and nearshore deposits of the bay, and adjacent rivers.

The storm overwash deposits of Cyclone Sidr are strongly influenced by geomorphology, and sediment characters around the depositional site of the area. The overwash deposits represent different sedimentary processes compared to modern overwash deposits due to the different geographic setup of the area and sediment source characteristics (Table 5.2). Cyclone-induced storm surge and subsequent heavy rainfall flooded low elevated adjacent coastal areas of the bay. The water level reached up to 6m above astronomical tide during landfall of Cyclone Sidr at the Kuakata coast and flooded behind the embankment of the area. The surging water carried suspended mud from the bay that also contained brackish to marine diatoms. Storm surge, especially during a tropical cyclone, eroded offshore muddy sediment, beach face and dunes, and transported to landward during landfall. The area was also flooded by the adjacent river that contained suspended mud with freshwater diatoms. Both high water level influenced sediments from the bay and river contributed depositional process during a storm surge (Figure 5.10). These sediments were sorted according to storm wave, and normal graded light gray to white sand and olive gray sandy silt settled over the area. The characteristics of the storm deposits along the delta coast are significantly induced by local geological factor and intensity of storm surge.

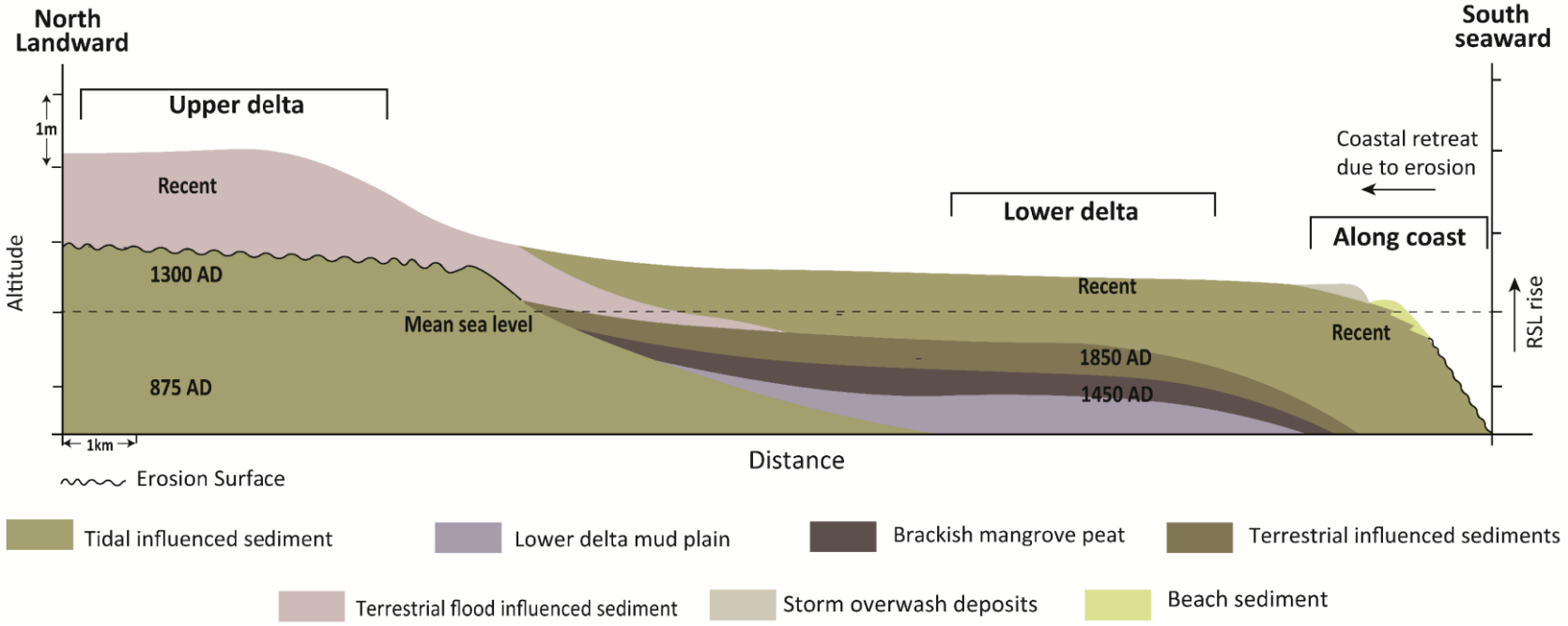

Figure 6.1: Schematic diagrams of depositional process from the upper delta plain to the coast during the last 1000 years in the southwestern GBM delta, Bangladesh.

The above summary of the analyses is sufficient to describe the effect of RSL and sediment supply on the sedimentation and coastal dynamics of the study areas. Chapter 3 shows that the depositional environment and sedimentation process in the southwestern upper and lower delta plain areas has been shifted laterally as well as vertically by the influence of RSL. Sea level and sediment supply characteristics have influenced the sedimentation processes. The rise of sea level at present has increased inundation that influences the sedimentation. The modern aged terrestrial flood sediment deposited at the upper part in the upper delta plain, tidal sediment in the lower delta plain (Chapter 3), and storm overwash deposits overlies the tidal mud found along with the coast (Chapter 4 and 5) (Figure 6.1). The stability of deltaic coastlines at lower delta plain depends on accretional fluvial inputs, erosional wave and tidal force. The rising sea level and anthropogenic activities at the upstream Ganges River influenced the coastal morphology and modern sedimentation at the river mouth of the area that has been demonstrated in Chapter 4. The southwestern coast of Bangladesh permanently lost its landmass, consequently, the marine-influenced deposits progressively thickened towards land. Sea level rise and decreased sediment supply in the southwestern delta coast caused the coastal evolution, tidal and storm overwash sedimentation increases at the low-lying deltaic region of the area (Figure 6.1).

Storm overwash deposit of tropical cyclone events along the coast represents distinctive flooding characters on a global scale (Chapter 5, Table 5.2). Both coastal and fluvial sediments contributed to the sources of storm overwash deposits. High water levels in both the bay and rivers during the cyclone, played important roles in the formation of storm overwash deposits along the GBM delta coast.

Overall, the research will give an idea about depositional environment, sedimentation process, and coastal morphology with fluctuation of the sea during the late Holocene. Factors such as upstream morphology, surface runoff, hydrology, and anthropogenic activities including increased urbanization and land use may induce change to coastal morphology and sedimentation. These factors need to be incorporated into future research for a clearer view concerning climate change. Investigation of geological data extended over longer periods would expand our understanding of delta evolution, particularly in the context of climate change.

Acknowledgements

This work would not have been possible without the financial support from Mitsubishi Corporation International Scholarship (MITSU 1925) during my study in Japan. The research is partly supported by Grant-in-Aid for scientific research (no. 18K03778 for KH) from the Japan Society for Promotion of Science (JSPS). Additionally, field survey costs were covered by the student research grant from Shinshu University.

First and foremost, I would like to express my special appreciation and thanks to my advisor, Professor Dr. Koichi Hoyanagi for taking a chance on me four years ago and for introducing me to this exciting field of science. Since the day I started the program, he offered extensive professional guidance, dedicated support, and encouragement until the very last day of my Ph.D. I consider it a great opportunity to learn from his research expertise. I am also grateful to him for providing me a research assistantship over these years. A big thank you, Prof. Hoyanagi, I could not have imagined having a better mentor for my Ph.D. I'm looking forward to collaborating with you in coming years.

I would also like to express my gratitude to the rest of the team. I thank Drs. Kohki Yoshida, Naomi Murakoshi, Katsura Yamada, and Masaki Yamada of Shinshu University, and Dr. Toru Tamura, Geological Survey of Japan, National Institute of Advanced Industrial Science and Technology (AIST) for serving in my Ph.D. committee. Without their remarkable support and expertise, it would not have been possible to finish my doctorate. I would particularly like to acknowledge Dr. Masaki Yamada, Department of Geology at Shinshu University for his endless patience to identify storm overwash deposits during fieldwork. I am grateful to Dr. A.K.M. Khorshed Alam, Geological Survey of Bangladesh (GSB), and Dr. Manoj Kumer Ghosh, Department of Geography and Environmental Studies at the University of Rajshahi, Bangladesh for constructive discussions, suggestions during the research, and satellite image processing. I am thankful to Shiori Uchiyama of Shinshu University for all the insightful discussions and advice during geochemical analyses and knowledge in fossil diatoms studies. I thank her very much. I am grateful to Dr. Craig S Fulthorpe, Institute for Geophysics, the University of Texas at Austin, and Dr. M. Shafiqul Alam, Department of Geology and Mining, University of Rajshahi for their valuable suggestions during editing the manuscripts.

I would like to thank my friends for providing the support and friendship that I needed throughout these years: Lalit Rai, Hiromi Sashi, Junichi Machida, Kodai Kondo, and Natsumi Kasai. A special mention of thanks to my respected teachers and now colleagues, Drs. M. Habibur Rahman, Md. Badrul Islam, Mushfique Ahmed, Chowdhury Sarwar Jahan, Golam Shabbir Sattar, Md. Sultan–Ul–Islam, Khondaker Emamul Haque, Sohail Kabir, Younus Ahmed Khan, A.H.M. Selim Reza, Ismail Hossain, and Fazal Md. Mohi Shine, Md. Abdur Rahman, Md. Abdul Malek, Md. Ibrahim Adham at the Department of Geology and Mining, University of Rajshahi for encouraging me to finish the program during these challenging global times.

This last word of acknowledgment I have saved for my dear family for always believing in me and being there for me. I am deeply thankful for my wife's faithful support, encouragement, and patience. Words cannot express how grateful I am to my parents for all of the sacrifices that they have made on my behalf. Their love and unconditional support have always been my strength. I am lucky enough to have the most supportive and loving siblings. I am grateful to my mother-in-law and also, my father-in-law who, I know, will be very proud of me for reaching this milestone. I sincerely thanks to all who assisted directly and indirectly with my dissertation. Finally, I am grateful to almighty Allah.

References

Abu-Zied, R.H. and Bantan, R.A., 2015. Palaeoenvironment, palaeoclimate, and sea-level changes in the Shuaiba Lagoon during the late Holocene (last 3.6 ka), eastern Red Sea coast, Saudi Arabia. *The Holocene*, **25 (8)**, pp. 1301–1312.

Acharyya, S., 2007. Collisional emplacement history of the Naga-Andaman ophiolites and the position of the eastern Indian suture. *Journal of Asian Earth Science*, **29 (2–3)**, pp. 229–242.

Ahmed, G.U., 1999. Decision analysis for Bangladesh coastal afforestation. Master thesis, *University of Toronto*, Canada.

Akter, J., Sarker, M.H., Popescu, I. and Roelvink, D., 2016. Evolution of the Bengal Delta and its prevailing processes. *Journal of Coastal Research*, **32 (5**), pp. 1212–1226.

Alam, M., 1996. Subsidence of the Ganges–Brahmaputra Delta of Bangladesh and associated drainage, sedimentation and salinity. In: Milliman, J.D. and Haq, B.U. (eds.), *Sea-Level Rise and Coastal Subsidence.* Dordrecht, The Netherlands: Kluwer Academic Publishers, pp. 169–192.

Alam, M., Alam, M.M., Curray, J.R., Chowdhury, M.L.R. and Gani, M.R., 2003. An overview of the sedimentary geology of the Bengal Basin in relation to the regional tectonic framework and basin-fill history. *Sedimentary Geology*, **155 (3–4)**, pp. 179–208.

Alam, M.K., Hasan, A.K.M.S., Khan, M.R. and Whitney, J.W., 1990. Geological map of Bangladesh. Geological Survey of Bangladesh, Dhaka, Scale 1: 1 000 000.

Ali, A., 1996. Vulnerability of Bangladesh to Climate Change and Sea Level Rise Through Tropical Cyclones and Storm Surges. *Water, Air, and Soil Pollution*, **92**, pp. 171–179.

Allison, M. and Kepple, E., 2001. Modern sediment supply to the lower delta plain of the Ganges-Brahmaputra River in Bangladesh. *Geo-Marine Letters*, **21**, pp. 66–74.

Allison, M.A., 1998. Historical changes in the Ganges-Brahmaputra Delta Front. *Journal of Coastal Research*, **14**, pp. 1269–1275.

Allison, M.A., Khan, S.R., Goodbred Jr, S.L. and Kuehl, S.A., 2003. Stratigraphic evolution of the late Holocene Ganges–Brahmaputra lower delta plain. *Sedimentary Geology*, **155 (3–4)**, pp. 317–342.

Alongi, D.M., 2015. The Impact of Climate Change on Mangrove Forests. *Current Climate Change Report,* **1**, pp. 30–39.

Antony, C., Testut, L., Unnikrishnan, A.S., 2014. Observing storm surges in the Bay of Bengal from satellite altimetry. *Estuarine, Coastal and Shelf Science,* **151**, pp. 131–140.

Auerbach, L.W., Goodbred Jr, S.L., Mondal, D.R., Wilson, C.A., Ahmed, K.R., Roy, K., Steckler, M.S., Small, C., Gilligan, J.M. and Ackerly, B.A., 2015. Flood risk of natural and embanked landscapes on the Ganges–Brahmaputra tidal delta plain. *Nature Climate Change,* **5 (2),** pp. 153–157.

Bagchi, K., 1944. The Ganges Delta. *University of Calcutta*, Calcutta, 157p.

Balaguru, K., Taraphdar, S., Leung, L.R. Foltz, G.R., 2014. Increase in the intensity of postmonsoon Bay of Bengal tropical cyclones. *Geophysical Research Letters*, **41 (10)**, pp. 3594–3601.

Bandyopadhyay, S., 2019. Sundarban: A Review of Evolution & Geomorphology. *World Bank Group*. Washington DC, 36p.

Barua, D.K., 1990. Suspended sediment movement in the estuary of the Ganges-Brahmaputra-Meghna river system. *Marine Geology,* **91 (3)**, pp. 243–253.

Barua, D.K., Kuehl, S.A., Miller, R.L. and Moore, W.S., 1994. Suspended sediment distribution and residual transport in the coastal ocean off the Ganges-Brahmaputra river mouth. *Marine Geology*, **120 (1–2)**, pp. 41–61.

Basilici, G., de Luca, P.H.V. and Oliveira, E.P., 2012. A depositional model for a wave-dominated open-coast tidal flat, based on analyses of the Cambrian–Ordovician Lagarto and Palmares formations, north-eastern Brazil. *Sedimentology*, **59 (5)**, pp. 1613–1639.

Beck, R., Burbank, D., Sercombe, W., Riley, G., Barndt, J., Berry, J., Afzal, F., Khan, A., Jurgen, H., Metje, J., Cheema, A., Sha-figue, N., Lawrence, R. and Asif Khan, M., 1995. Stratigraphicevidence for an early collision between north–west India and Asia. *Nature*, **373**, pp. 55–58.

Behara, A., Vinayachandran, P.N., 2016. An OGCM study of the impact of rain and river water forcing on the Bay of Bengal. *Journal of Geophysical Research: Oceans,* **121 (4)**, pp. 2425–2446.

Benshila, R., Durand, F., Masson, S., Bourdalle-Badie, R., Montegut, C.D.B., Papa, F. and Madec, G., 2014. The upper Bay of Bengal salinity structure in a high-resolution model. *Ocean Modelling,* **74**, pp. 36–52.

Bhargava, R., Sarkar, D. and Friess, D.A., 2021. A cloud computing-based approach to mapping mangrove erosion and progradation: Case studies from the Sundarbans and French Guiana. *Estuarine, Coastal and Shelf Science*, **248**:106798.

Bird, E., 1960. The formation of sand beach ridges. *Australian Journal of Science*, **22**, pp. 349–350.

Blair, N.E. and Carter Jr, W.D., 1992. The carbon isotope biogeochemistry of acetate from a methanogenic marine sediment. *Geochimica et Cosmochimica Acta*, ***56* (3)**, pp. 1247–1258.

Blott, S.J. and Pye, K., 2001. GRADISTAT: a grain size distribution and statistics package for the analysis of unconsolidated sediments. *Earth surface processes and Landforms*, ***26* (11)**, pp. 1237–1248.

Bouillon, S., Dahdouh-Guebas, F., Rao, A.V.V.S., Koedam, N. and Dehairs, F., 2003. Sources of organic carbon in mangrove sediments: variability and possible ecological implications. *Hydrobiologia*, ***495* (1)**, pp. 33–39.

Brammer, H., 2014. Bangladesh's dynamic coastal regions and sea-level rise. *Climate Risk Management,* **1**, pp. 51–62.

Breithaupt, J.L., Smoak, J.M., Smith III, T.J. and Sanders, C.J., 2014. Temporal variability of carbon and nutrient burial, sediment accretion, and mass accumulation over the past century in a carbonate platform mangrove forest of the Florida Everglades. *Journal of Geophysical Research: Biogeosciences*, ***119* (10)**, pp. 2032–2048.

Brill, D., May, S.M., Engel, M., Reyes, M., Pint, A., Opitz, S., Dierick, M., Gonzalo, L.A., Esser, S. and Brückner, H., 2016. Typhoon Haiyan's sedimentary record in coastal environments of the Philippines and its palaeotempestological implications. *Natural Hazards and Earth System Sciences*, **16 (12)**, pp. 2799–2822.

Brill, D., Pint, A., Jankaew, K., Frenzel, P., Schwarzer, K., Vött, A. and Brückner, H., 2014. Sediment transport and hydrodynamic parameters of tsunami waves recorded in onshore geoarchives. *Journal of Coastal Research*, ***30* (5)**, pp. 922–941.

Bristow, C.S., 1999. Avulsion, river metamorphosis and reworking by under-fit stream: a modern example from the Brahmaputra River in Bangladesh and a possible ancient example in the Spanish Pyreness. In: Smith, N.D. and Rogers, J. (eds.), *Fluvial Sedimentology VI. International Association of Sedmentologists*, Special Publication **No. 28**, pp. 221–230.

Bronk Ramsey, C., 2009. Bayesian Analysis of Radiocarbon Dates. *Radiocarbon,* **51 (1)**, pp. 337–360.

Brown, S. and Nicholls, R.J., 2015. Subsidence and human influences in mega deltas: the case of the Ganges–Brahmaputra–Meghna. *Science of the Total Environment*, **527**, pp. 362–374.

Bruun, P., 1962. Sea level rise as a cause of shore erosion. *American Society of Civil Engineers Proccding, Journal of the Waterways and Harbours Division*, **88**, pp. 117–130.

Buynevich, I.V., FitzGerald, D.M. and van Heteren, S., 2004. Sedimentary records of intense storms in Holocene barrier sequences, Maine, USA. *Marine Geology,* **210**, pp. 135−148.

Cahoon, D.R., 2006. A review of major storm impacts on coastal wetland elevations. *Estuaries and Coasts*, **29 (6)**, pp. 889–898.

Chamberlain, E.L., Wallinga, J., Reimann, T., Goodbred Jr, S.L., Steckler, M.S., Shen, Z. and Sincavage, R., 2017. Luminescence dating of delta sediments: Novel approaches explored for the Ganges-Brahmaputra-Meghna Delta. *Quaternary Geochronology*, **41**, pp. 97–111.

Chander, G. and Markham, B., 2003. Revised Landsat-5 TM radiometric calibration procedures and postcalibration dynamic ranges. *IEEE Transactions on geoscience and remote sensing,* **41 (11)**, pp. 2674–2677.

Chang, G.C., Dickey, T.D., Williams, A.J., 2001. Sediment resuspension over a continental shelf during hurricanes Edouard and Hortense. *Journal of Geophysical Research: Oceans*, **106 (C5)**, pp. 9517–9531.

Chaturvedi, S. and Sakhuja, V., 2015. Climate Change and The Bay of Bengal: Evolving Geographic of Fear and Hope. 1st publication, ISEAS-Yusof Ishak Institute, Singapore.

Chavez, P.S., 1996., Image-based atmospheric corrections-revisited and improved. *Photogrammetric engineering and remote sensing,* **62 (9)**, pp. 1025–1035.

Climate Change Cell (CCC), 2016. Assessment of sea level change on Bangladesh Coast through trend analysis. Department of Environment Ministry of Environment and Forests, Bangladesh.

Cohen, M.C., Souza Filho, P.W., Lara, R.J., Behling, H. and Angulo, R.J., 2005. A model of Holocene mangrove development and relative sea-level changes on the Bragança Peninsula (northern Brazil). *Wetlands Ecology and Management*, ***13*** **(4)**, pp. 433–443.

Coleman, J.A., 1969. Brahmaputra River: channel processes and sedimentation. *Sedimentary Geology,* **3**, pp. 129–239.

Congalton, R.G. and Green, K., 2019. Assessing the accuracy of remotely sensed data: principles and practices, 3rd Ed. CRC Press, Boca Raton.

Congalton, R.G., 1991. A review of assessing the accuracy of classifications of remotely sensed data. *Remote sensing of environment,* **37 (1)**, pp. 35–46.

Congalton, R.G., Oderwald, R.G. and Mead, R.A., 1983. Assessing Landsat classification accuracy using discrete multivariate analysis statistical techniques. *Photogrammetric engineering and remote sensing*, **49 (12)**, pp. 1671–1678.

Coppin, P., Jonckheere, I., Nackaerts, K., Muys, B. and Lambin, E., 2004. Review article digital change detection methods in ecosystem monitoring: a review. *International journal of remote sensing*, **25 (9)**, pp. 1565–1596.

Curray, J., Emmel, F. and Crampton, P., 1969. Holocene history of a strand plain, lagoonal coast, Nayarit, Mexico. In: Ayala-Castanares A., editors. *Coastal Lagoons: A Symposium.* Mexico City: Universidad Nacional Autonoma de Mexico, pp. 63–100.

Curray, J.R., 1994. Sediment volume and mass beneath the Bay of Bengal. *Earth and Planetary Science Letters*, **125**, pp. 371–383.

Curray, J.R., 2014. The Bengal depositional system: from rift to orogeny. *Marine Geology*, **352**, pp. 59–69.

Dai, A. And Trenberth, K.E., 2002. Estimates of freshwater discharge from continents: Latitudinal and seasonal variations. *Journal of hydrometeorology*, ***3*****(6)**, pp. 660–687.

Daidu, F., Yuan, W. and Min, L., 2013. Classifications, sedimentary features and facies associations of tidal flats. *Journal of Palaeogeography*, **2 (1)**, pp. 66–80.

Darby, S.E., Hackney, C.R., Leyland, J., Kummu, M., Lauri, H., Parsons, D.R., Best, J.L., Nicholas, A.P. and Aalto, R., 2016. Fluvial sediment supply to a mega-delta reduced by shifting tropical-cyclone activity. *Nature*, **539 (7628)**, pp. 276–279.

Das, O., Wang, W., Donoghue, J., Xu, X., Coor, J., Elsner, J., Xu, Y., 2013. Reconstruction of paleostorms and paleoenvironment using geochemical proxies archived in the sediments of two coastal lakes in northwest Florida. *Quaternary Science Reviews*, **68**, pp. 142–153.

Datta, D.K., Subramanian, V., 1997. Texture and mineralogy of sediments from the Ganges-Brahmaputra-Meghna River System in the Bengal Basin, Bangladesh and their environmental implications. *Environmental Geology,* **30 (3–4)**, pp. 181–188.

Degeai, J.P., Devillers, B., Dezileau, L., Oueslati, H., Bony, G., 2015. Major storm periods and climate forcing in the Western Mediterranean during the Late Holocene. *Quaternary Science Review*, **129**, pp. 37–56.

Deines, P., 1980. The isotopic composition of reduced organic carbon. In: Fritz P, Fontes JC (eds) *Handbook of Environmental Isotope Geochemistry, vol 1, The Terrestrial Environment. A*. Elsevier, Amsterdam, pp. 329–406.

Disaster Management Bureau (DMB), 2010. National Plan for Disaster Management 2010-2015. Government of the People's Republic of Bangladesh.

Donnelly, J.P. Butler, J., Roll, S., Wengren, M. and Webb III T., 2004. A backbarrier overwash record of intense storms from Brigantine, New Jersey. *Marine Geology*, **210**, pp. 107−121.

Duff, P.Mcl.D., 1993. Holmes' Principles of Physical Geology (14th ed). Stanley Thornes (Publishers) Ltd.

Dunn, F.E., Nicholls, R.J., Darby, S.E., Cohen, S., Zarfl, C. and Fekete, B.M., 2018. Projections of historical and 21st century fluvial sediment delivery to the Ganges-Brahmaputra-Meghna, Mahanadi, and Volta deltas. *Science of the total environment*, **642**, pp. 105–116.

EGIS, 2000. Environmental Baseline of Gorai River Restoration Project, EGIS-II. Bangladesh Water Development Board, Ministry of Water Resources, Government of Bangladesh, Delft, the Netherlands.

Elsey-Quirk, T., 2016. Impact of Hurricane Sandy on salt marshes of New Jersey. *Estuarine, Coastal and Shelf Science*, ***183***, pp. 235–248.

Elsner, J.B., Kocher, B., 2000. Global tropical cyclone activity: a link to the North Atlantic Oscillation. *Geophysical Research Letters*, **27 (1)**, pp. 129–132.

Felton, C.S., Subrahmanyam, B., Murty, V.S.N., Shriver, J.F., 2014. Estimation of the barrier layer thickness in the Indian Ocean using Aquarius salinity. *Journal of Geophysical Research: Oceans,* **119 (7)**, pp. 4200–4213.

Fergusson, J., 1863. On recent changes in the delta of the Ganges. *Quarterly Journal of the Geological Society*, **19**, pp. 321–353.

Folk, R.L. and Ward, W.C., 1957. Brazos River bar: a study in the significance of grain size parameters. *Journal of Sedimentary Research*, **27 (1)**, pp. 3–26.

Folk, R.L., 1966. A review of grain-size parameters. *Sedimentology*, **6 (2)**, pp. 73–93.

Food and Agriculture Organization (FAO), 2007. Food and Agriculture Organization of the United Nations. *The world's Mangroves 1980–2005*. Forest Resources Division, FAO, Rome.

Foster, I.D., Albon, A.J., Bardell, K.M., Fletcher, J.L., Jardine, T.C., Mothers, R.J., Pritchard, M.A., Truner, S.E., 1991. High energy coastal sedimentary deposits; an evaluation of depositional processes in southwest England. *Earth Surface Processes and Landforms*, **16 (4)**, pp. 341–356.

Frappier, A.B., 2009. A stepwise screening system to select storm sensitive stalag-mites: Taking a targeted approach to speleothem sample methodology. *Quaternary International, Quaternary International*, ***187*** **(1)**, pp. 25–39.

Gao, X., Yang, Y. and Wang, C., 2012. Geochemistry of organic carbon and nitrogen in surface sediments of coastal Bohai Bay inferred from their ratios and stable isotopic signatures. *Marine Pollution Bulletin*, **64**, pp. 1148–1155.

Ghosh, A., Schmidt, S., Fickert, T. and Nüsser, M., 2015. The Indian Sundarban mangrove forests: history, utilization, conservation strategies and local perception. *Diversity*, *7* **(2)**, pp. 149–169.

Ghosh, M.K., Kumar, L. and Roy, C. 2015. Monitoring the coastline change of Hatiya Island in Bangladesh using remote sensing techniques. *ISPRS Journal of Photogrammetry and Remote Sensing*, **101**, pp. 137–144.

Ghosh, M.K., Kumar. L. and Roy, C., 2016. Mapping long-term changes in mangrove species composition and distribution in the Sundarbans. *Forests,* **7 (12)**, 305.

Goff, J., Crozier, M., Sutherland, V., Cochran, U. and Shane, P., 1998. Possible tsunami deposits from the 1855 earthquake, North Island, New Zealand. *Geological Society, London, Special Publications*, **146 (1)**, pp. 353–374.

Gonneea, M.E., Paytan, A. and Herrera-Silveira, J.A., 2004. Tracing organic matter sources and carbon burial in mangrove sediments over the past 160 years. *Estuarine, Coastal and Shelf Science*, **61 (2)**, pp. 211–227.

Goodbred Jr, S.L. and Kuehl, S.A., 1998. Floodplain Processes in the Bengal Basin and the storage of Ganges-Brahmaputra river sediment: An accretion study using ^{137}Cs and ^{210}Pb geochronology. *Sedimentary Geology*, **121**, pp. 239–258.

Goodbred Jr, S.L. and Kuehl, S.A., 1999. Holocene and modern sediment budgets for the Ganges-Brahmaputra river system: Evidence for highstand dispersal to flood-plain, shelf, and deep-sea depocenters. *Geology*, **27 (6)**, pp. 559–563.

Goodbred Jr, S.L. and Kuehl, S.A., 2000a. Enormous Ganges-Brahmaputra sediment discharge during strengthened early Holocene monsoon. *Geology*, **28**, pp. 1083–1086.

Goodbred Jr, S.L. and Kuehl, S.A., 2000b. The significance of large sediment supply, active tectonism, and eustasy on sequence development: Late Quaternary Stratigraphy and evolution of the Ganges-Brahmaputra delta. *Sedimentary Geology*, **133**, pp. 227–248.

Goodbred Jr, S.L., Kuehl, S.A., Steckler, M.S. and Sarker, M.H., 2003. Controls on facies distribution and stratigraphic preservation in the Ganges–Brahmaputra delta sequence. *Sedimentary Geology*, **155 (3–4)**, pp. 301–316.

Goodbred Jr, S.L., Paolo, P.M., Ullah, M.S., Pate, R.D., Khan, S.R., Kuehl, S.A., Singh, S.K. and Rahaman, W., 2014. Piecing together the Ganges-Brahmaputra-Meghna River delta: Use of sediment provenance to reconstruct the history and interaction of multiple fluvial systems during Holocene delta evolution. *Bulletin*, ***126*** **(11–12)**, pp. 1495–1510.

Goto, T., Satake, K., Sugai, T., Ishibe, T., Harada, T. and Murotani, S., 2015. Historical tsunami and storm deposits during the last five centuries on the Sanriku coast, Japan. *Marine Geology*, **367**, pp. 105–117.

Graham, M.C., Eaves, M.A., Farmer, J.G., Dobson, J. and Fallick, A.E., 2001. A study of carbon and nitrogen stable isotope and elemental ratios as potential indicators of source and fate of organic matter in sediments of the Forth Estuary, Scotland. *Estuarine, Coastal and Shelf Science*, ***52*** **(3)**, pp. 375–380.

Grall, C., Steckler, M.S., Pickering, J., Goodbred Jr, S.L., Sincavage, R., Paola, C., Akhter, S.H. and Spiess, V., 2018. A base-level stratigraphic approach to determining Holocene subsidence of the Ganges–Meghna–Brahmaputra Delta plain. *Earth and Planetary Science Letters*, **499**, pp. 23–36.

Gray, W.M., 1985. Tropical Cyclone Global Climatology, WMO Technical Document WMO/TD No. 72, Vol. I, WMO, Geneva, Switzerland, pp. 3–19.

Greb, S.F. and Archer, A.W., 1998. Annual sedimentation cycles in rhythmites of Carboniferous tidal channels. In: Tidalites: Processes and Products, Alexander, C.R., Davis, R.A., Hemry, V.J. (Eds). Soc. Econ. Paleontol. Mineral. Spec. Pub. **61**, pp. 75–82.

Griffiths, J.A., Zhu, F., Chan, F.K.S. and Higgitt, D.L., 2019. Modelling the impact of sea-level rise on urban flood probability in SE China. *Geoscience Frontiers*, **10 (2)**, pp. 363–372.

Grinsted, A., Moore, J.C. and Jevrejeva, S., 2010 Reconstructing sea level from paleo and projected temperatures 200 to 2100 AD. *Climate Dynamics,* **34**, pp. 461–472.

Guntenspergen, G., Cahoon, D., Grace, J., Steyer, G., Fournet, S., Townson, M., Foote, A., 1995. Disturbance and recovery of the Louisiana coastal marsh landscape from the impacts of Hurricane Andrew. *Journal of Coastal Research*, **21**, pp. 324–339.

Hanebuth, T.J.J., Kudrass, H.R., Linstädter, J., Islam, B. And Zander, A.M., 2013. Rapid coastal subsidence in the Central Ganges–Brahmaputra Delta (Bangladesh) since the 17th century deduced from submerged salt-producing kilns. *Geology*, **41**, pp. 987–990.

Haque, M.M. and Hoyanagi, K., 2021. Influences of sea level on depositional environment during the last 1000 years in the southwestern Bengal delta, Bangladesh. *The Holocene*, **31 (6)**, pp. 915–925.

Haque, A. and Jahan, S., 2016. Regional impact of cyclone Sidr in Bangladesh: A multi-sector analysis. *International Journal of Disaster Risk Science*, **7 (3)**, pp. 312–327.

Haque, M.M., Ghosh, M.K. and Hoyanagi, K., 2021a. Coastal development in southwestern Bangladesh: understanding the interplay between storms and sea level rise. *Progress in Physical Geography*, Doi: 10.1177/03091333211046189 (online first).

Haque, M.M., Yamada, M., Uchiyama, S. and Hoyanagi, K., 2021b. Depositional setup and characteristics of the storm deposit by the 2007 Cyclone Sidr on Kuakata Coast, Bangladesh. *Marine Geology*, **442**, 106652.

Harris, D.L., 1963. Characteristics of the Hurricane Storm Surge, Technical Paper No. **48** (Washington, D.C.: U.S. Dept. of Commerce, Weather Bureau), 1–139p.

Hasegawa, K., 2008. Features of super cyclone Sidr to hit Bangladesh in Nov 07 and measures for disaster from results of JSCE investigation, Proc. WFEO-JFES-JSCE Joint Int. Symp. on Disaster Risk Management, Sendai, Japan. Science council of Japan, pp. 51–58.

Hawkes, A.D. and Horton, B.P., 2012. Sedimentary record of storm deposits from Hurricane Ike, Galveston and San Luis Islands, Texas. *Geomorphology,* **171**, pp. 180−189.

Hay, C.C., Morrow, E., Kopp, R.E. and Mitrovica, J.X., 2015. Probabilistic reanalysis of twentieth-century sea-level rise. *Nature*, **517**, pp. 481–484.

He, B., Dai, M., Huang, W., Liu, Q., Chen, H. and Xu, L., 2010. Sources and accumulation of organic carbon in the Pearl River Estuary surface sediment as indicated by elemental, stable carbon isotopic, and carbohydrate compositions. *Biogeosciences*, **7 (10)**, pp. 3343–3362.

Heroy, D.C., Kuehl, S.A. and Goodbred Jr, S.L., 2003. Mineralogy of the Ganges and Brahmaputra Rivers: implications for river switching and Late Quaternary climate change. *Sedimentary Geology*, **155 (3–4)**, pp. 343–359.

Hesp, P., 2006. Sand beach ridges: definitions and re-definition. *Journal of Coastal Research*, **39**, pp. 72–75.

Higgins, S.A., Overeem, I., Steckler, M.S., Syvitski, J.P., Seeber, L. and Akhter, S.H., 2014. InSAR measurements of compaction and subsidence in the Ganges-Brahmaputra Delta, Bangladesh. *Journal of Geophysical Research: Earth Surface*, **119 (8)**, pp. 1768–1781.

Hoefs. J., 2009., *Stable isotope geochemistry*, 6th edn. Berlin, Heidelberg, New York: Springer.

Hong, I., Pilarczyk, J.E., Horton, B.P., Fritz, H.M., Kosciuch, T.J., Wallace, D.J., Dike, C., Rarai, A., Harrison, M.J. and Jockley, F.R., 2018. Sedimentological characteristics of the 2015 tropical cyclone pam overwash sediments from Vanuatu, South Pacific. *Marine Geology,* ***396***, pp. 205−214.

Hoque, M. and Alam, M., 1997. Subsidence of Lower deltaic area of Bangladesh. *Marine Geology,* **20 (1)**, pp. 105–120.

Hori, K., Saito, Y., Zhao, Q. and Wang, P., 2002. Architecture and evolution of the tide-dominated Changjiang (Yangtze) River delta, China. *Sedimentary Geology,* **146 (3–4),** pp. 249–264.

Hori, K., Saito, Y., Zhao, Q., Cheng, X., Wang, P., Sato, Y. and Li, C. 2001. Sedimentary facies of the tide-dominated paleo-Changjiang (Yangtze) estuary during the last transgression. *Marine Geology*, **177 (3–4)**, pp. 331–351.

Horton, B.P., Rossi, V. and Hawkes, A.D., 2009. The sedimentary record of the 2005 hurricane season from the Mississippi and Alabama coastlines. *Quaternary International,* **195,** pp. 15−30.

Hossain, M.L., Hossain, M.K. and Das, S. R., 2010. Vulnerability of Bangladesh to Natural and Anthropogenic Disasters. Vision Publication, Dhaka, Bangladesh.

Hossain, M.M., 2012. Storm Surges and Coastal Erosion in Bangladesh—State of the System, Climate Change Impacts and "Low Regret" Adaptation Measures. *Master Thesis*, Leibniz Universität Hannover, Germany.

Hossain, M.S., Khan, M.S.H., Chowdhury, K.R. and Abdullah, R., 2019. Synthesis of the Tectonic and Structural Elements of the Bengal Basin and Its Surroundings. In: Mukherjee S. (Eds) *Tectonics and Structural Geology: Indian Context*. Springer Geology. Springer, Cham, pp. 135–218.

Howa, H.L. and Stanley, D.J., 1991. Plant-Rich Holocene Sequences in the Northern Nile Delta Plain, Egypt: Petrology, Distribution, and Depositional Environments. *Journal of Coastal Research,* **7 (4)**, pp. 1077–1096.

Howard, A.D., Fairbridge, R.W. and Quinn, J.H., 1968. Terraces, fluvial introduction. In: *Geomorphology: Encyclopedia of Earth Science*., Berlin, Heidelberg: Springer.

Intergovernmental Panel on Climate Change (IPCC), 2007. Climate Change 2007: Synthesis Report. Contribution of Working Groups I, II and III to the Fourth Assessment Report of the Intergovernmental Panel on Climate Change, Geneva, Switzerland.

Islam, M.S. and Tooley, M.J., 1999. Coastal and sea-level changes during the Holocene in Bangladesh. *Quaternary International*, **55**, pp. 61–75.

Islam, M.S., 2001. *Sea-level changes in Bangladesh: the last ten thousand years*, Asiatic Society of Bangladesh.

Islam, S.N. and Gnauck, A., 2008. Mangrove wetland ecosystems in Ganges–Brahmaputra delta in Bangladesh. *Front Earth Science China,* **2 (4)**, pp. 439–448.

Islam, S.N. and Gnauck, A., 2009. Threats to the Sundarbans mangrove wetland ecosystems from transboundary water allocation in the Ganges basin: A preliminary problem analysis. *International Journal Ecological Economics Statistic*, **13 (W09)**, pp. 64−78.

Japan Society of Civil Engineers (JSCE), 2008. Investigation Report on the Storm Surge Disaster by Cyclone Sidr in Nov 2007 in Bangladesh (Transient Translation). Investigation Team of JSCE.

Jasper, J.P. and Gagosian, R.B., 1990. The source of the deposition of organic matter in the Late Quaternary Pigmy Basin, Gulf of Mexico. *Geochimica et Cosmo-Chemica Acta*, **54**, pp. 1117–1132.

Jones, V.J., 2007. Diatom introduction S. Elias (Ed.), Encyclopedia of Quaternary Science. Oxford: Elsevier, pp. 476–484.

Karim, M.F. and Mimura, N., 2008. Impacts of climate change and sea-level rise on cyclonic storm surge floods in Bangladesh. *Global environmental change –Human Policy Dimen*, **18 (3),** pp. 490–500.

Karpytchev, M., Ballu, V., Krien, Y., Becker, M., Goodbred Jr, S.L., Spada, G., Calmant, S., Shum, C.K. and Khan, Z., 2018. Contributions of a strengthened early Holocene monsoon and sediment loading to present-day subsidence of the Ganges-Brahmaputra delta. *Geophysical Research Letters*, ***45*** **(3)**, pp. 1433–1442.

Kay, S., Caesar, J. and Janes, T., 2018. Marine Dynamics and Productivity in the Bay of Bengal. In: Nicholls R., Hutton C., Adger W., Hanson S., Rahman M., Salehin M. (eds) *Ecosystem Services for Well-Being in Deltas*. Palgrave Macmillan, Cham.

Kim, K.O., Yamashita, T. and Choi, B.H., 2008. Coupled process-based cyclone surge simulation for the Bay of Bengal. *Ocean Modelling*, ***25*** **(3-4)**, pp.132–143.

Knapp, K.R., Kruk, M.C., Levinson, D.H., Diamond, H.J. and Neumann, C.J., 2010. The international best track archive for climate stewardship (IBTrACS) unifying tropical cyclone data. *Bulletin of the American Meteorological Society*, **91 (3)**, pp. 363–376.

Kortekaas, S. and Dawson, A.G., 2007. Distinguishing tsunami and storm deposits: an example from Martinhal, SW Portugal. *Sedimentary Geology*, **200**, pp. 208–221.

Krammer, K., 2000. Diatoms of Europe: Diatoms of European inland water and comparable habitats. In: Lange-Bertalot H (ed.) *The Genus Pinnularia, vol. 1*. Ruggell: Gantner.

Krammer, K., 2002. Diatoms of Europe: diatoms of European inland water and comparable habitats. H. Lange-Bertalot (Ed.), *The Genus Cymbella, vol. 3*. Gantner, Ruggell.

Krammer, K., 2003. Diatoms of Europe: Diatoms of European inland water and comparable habitats. In: Lange Bertalot H (ed.) *Cymbopleura, Delicata, Navicymbula, Gomphocymbellopsis, Afrocymel*l, vol. 4. Ruggell: Gantner.

Krien, Y., Karpytchev, M., Ballu, V., Becker, M., Grall, C., Goodbred Jr, S.L., Calmant, S., Shum, C.K. and Khan, Z., 2019. Present-day subsidence in the Ganges-Brahmaputra-Meghna Delta: Eastern amplification of the Holocene sediment loading contribution. *Geophysical Research Letters*, ***46*** **(19)**, pp. 10764–10772.

Krien, Y., Testut, L., Islam, A.K.M.S., Bertin, X., Durand, F., Mayet, C., Tazkia, A.R., Becker, M., Calmant, S., Papa, F., Ballu, V., Shum, C.K. and Khan, Z.H., 2017. Towards improved storm surge models in the northern Bay of Bengal. *Continental Shelf Research,* **135**, pp. 58–73.

Kristensen, E., Bouillon, S., Dittmar, T. and Marchand, C., 2008. Organic carbon dynamics in mangrove ecosystems: a review. *Aquatic botany*, ***89*** **(2)**, pp. 201–219.

Kudrass, H.R., Machalett, B., Palamenghi, L., Meyer, I. and Zhang, W., 2018. Sediment transport by tropical cyclones recorded in a submarine canyon off Bangladesh. *Geo-Marine Letters*, ***38*** **(6)**, pp. 481–496.

Kudrass, H.R., Michels, K.H., Wiedicke, M. and Suckow, A., 1998. Cyclones and tides as feeders of a submarine canyon off Bangladesh. *Geology*, ***26*** **(8)**, pp. 715–718.

Kuehl, S.A., Allison, M.A., Goodbred, Jr.S.L. and Kudrass, H.R., 2005. The Ganges-Brahmaputra delta. In: Gosian, L., Bhattacharya, J. (Eds) *River Deltas: Concepts, Models, and Examples*. vol. 83. SEPM Special Publication, Tulsa, Oklahoma, pp. 413–434.

Kuehl, S.A., Hariu, T.M. and Moore, W.S., 1989. Shelf sedimentation off the Ganges-Brahmaputra river system: evidence for sediment bypassing to the Bengal fan. *Geology*, **17**, pp. 1132–1135.

Kuehl, S.A., Levy, B.M., Moore, W.S. and Allison, M.A., 1997. Subaqueous delta of the Ganges-Brahmaputra river system. *Marine Geology*, ***144*** **(1-3)**, pp. 81–96.

La Touché, T.H.D., 1910. The Journals of Major James Rennell: Written for the Information of the Governors of Bengal During His Surveys of the Ganges and Brahmaputra Rivers 1764 to 1767, *The Asiatic Society*, Calcutta.

Lamb, A.L., Wilson, G.P., Leng, M.J., 2006. A review of coastal palaeoclimate and relative sea-level reconstructions using $\delta^{13}C$ and C/N ratios in organic material. *Earth-Science Reviews*, **75**, pp. 29–57.

Lambert, W.J., Aharon, P. and Rodriguez, A.B., 2008. Catastrophic hurricane history revealed by organic geochemical proxies in coastal lake sediments: a case study of Lake Shelby, Alabama (USA). *Journal of Paleolimnology*, **39 (1)**, pp. 117–131.

Landsea, C., 2013. "How do tropical cyclones form?" Frequently Asked Questions. Atlantic Oceanographic and Meteorological Laboratory, Hurricane Research Division. https://www.aoml.noaa.gov/hrd/tcfaq/TCFAQ_A.txt (Accessed 25 December, 2020).

Langat, P.K., Kumar, L., Koech, R. and Ghosh, M.K., 2019. Hydro-morphological characteristics using flow duration curve, Historical data and remote sensing: Effects of land use and climate. *Water*, **11 (2): 309**.

Lange-Bertalot, H., 2000. Iconographia Diatomologica Annotated Diatom Micrographs—*Diatom Flora of Marine Coasts I*, vol. 7. Koeltz Scientific Books, Königstein, Germany. (Copyright: A.R.G. Gantner Verlag K.G. by Andrzej Witkowiski, Horst Lange-Bertalot and Ditmar Metzeltin).

Lange-Bertalot, H., 2001. Diatoms of Europe: Diatoms of European inland water and comparable habitats. In: Lange-Bertalot H (ed.) *Navicula sensustricto, 10 Genera Separated from Navicula sensu stricto, Frustulia, vol. 2*. Ruggell: Gantner.

Leatherman, S.P., 1981. Overwash processes. *Benchmark Papers in Geology,* Vol. 58. Hutchinson Ross Publishing Co., USA.

Levkov, Z., 2009. Diatoms of Europe: Diatoms of European inland water and comparable habitats. In: Lange-Bertalot H (ed.) *Amphora sensulato*, vol. 5. Ruggell: Gantner.

Lindsay, J.F., Holiday, D.W. and Hulbert, A.G., 1991. Sequence stratigraphy and the evolution of the Ganges–Brahmaputra complex. *American Association of Petroleum Geologists Bulletin*, **75,** pp. 1233–1254.

Liu, K.B. and Fearn M.L., 1993. Lake-sediment record of late Holocene hurricane activities from coastal Alabama. *Geology*, **21 (9)**, pp. 793–796.

Ma, M., Wang, X., Veroustraete, F. and Dong, L., 2007. Change in area of Ebinur Lake during the 1998–2005 period. *International Journal of Remote Sensing*, **28 (24)**, pp. 5523–5533.

Mann, M.E., Zhang, Z., Rutherford, S., Bradley, R.S., Hughes, M.K., Shindell, D., Ammann, C., Faluvegi, G. and Ni, F., 2009. Global signatures and dynamical origins of the Little Ice Age and Medieval Climate Anomaly. *Science*, ***326*** **(5957)**, pp. 1256–1260.

Marchand, C., Disnar, J.R., Lallier-Vergès, E. and Lottier, N., 2005. Early diagenesis of carbohydrates and lignin in mangrove sediments subject to variable redox conditions (French Guiana). *Geochimica et Cosmochimica Acta*, **69 (1)**, pp. 131–142.

Mas, J.F., 1999. Monitoring land-cover changes: a comparison of change detection techniques. *International journal of remote sensing*, **20 (1)**, pp. 139–152.

Matias, A., Ferreira, Ó., Vila-Concejo, A., Garcia, T. and Dias, J.A., 2008. Classification of washover dynamics in barrier islands. *Geomorphology*, **97 (3-4)**, pp. 655–674.

MES II, 2001. *Hydro-morphological dynamics of the Meghna Estuary, Meghna Estuary Study (MES II)*. Prepared for BWDB, Dhaka, Bangladesh.

Meyers, P.A., 1994. Preservation of elemental and isotopic source identification of sedimentary organic matter. *Chemical Geology*, **144**, pp. 289–302.

Meyers, P.A., 1997. Organic geochemical proxies of paleoceanographic, paleolimnologic, and paleoclimatic processes. *Organic Geochemistry*, **27**, pp. 213–250.

Mikhailov, V. and Dotsenko, M., 2007. Processes of delta formation in the mouth area of the Ganges and Brahmaputra Rivers. *Water Resources*, **34 (4)**, pp. 385–400.

Miles, T., Seroka, G., Kohut, J., Schofield, O. and Glenn, S., 2015. Glider observations and modeling of sediment transport in Hurricane Sandy. *Journal of Geophysical Research: Oceans*, **120 (3)**, pp. 1771–1791.

Miller, D.L., Mora, C.I., Grissino-Mayer, H.D., Mock, C.J., Uhle, M.E. and Sharp, Z., 2006. Tree-ring isotope records of tropical cyclone activity. *Proceedings of the National Academy of Sciences*, **103 (39)**, pp. 14294–14297.

Milliman, J.D. and Farnsworth, K.L., 2013. *River Discharge to the Coastal Ocean: A Global Synthesis*. Cambridge, MA: Cambridge University Press.

Milliman, J.D. and Meade, R.H., 1983. World-wide delivery of river sediment to the oceans. *The Journal of Geology,* **91(1)**, pp. 1–21.

Milliman, J.D. and Syvitski, J.P., 1992. Geomorphic/tectonic control of sediment discharge to the ocean: the importance of small mountainous rivers. *The Journal of Geology*, **100 (5)**, pp. 525–544.

Ministry of Water Resources (MoWR), 2005. Coastal Zone Policy, Government of the People's Republic of Bangladesh.

Mirza, M.M.Q., 1998. Diversion of the Ganges water at Farakka and its effects on salinity in Bangladesh. *Environmental Management,* **22 (5)**, pp. 711–722.

Morgan, J.P. and McIntire, W.G., 1959. Quaternary geology of the Bengal basin, East Pakistan and India. *Geological Society of America Bulletin*, **70 (3)**, pp. 319–342.

Morton, R.A. and Sallenger Jr, A.H., 2003. Morphological impacts of extreme storms on sandy beaches and barriers. *Journal of Coastal Research*, pp. 560–573.

Morton, R.A., Gelfenbaum, G. and Jaffe, B.E., 2007. Physical criteria for distinguishing sandy tsunami and storm deposits using modern examples. *Sedimentary Geology*, **200 (3–4)**, pp. 184–207.

Mouyen, M., Longuevergne, L., Steer, P., Crave, A., Lemoine, J.M., Save, H. and Robin, C., 2018. Assessing modern river sediment discharge to the ocean using satellite gravimetry. *Nature communications*, **9 (1)**, 3384.

Mukherjee, A., Fryar, A.E. and Thomas, W.A., 2009. Geologic, geomorphic and hydrologic framework and evolution of the Bengal basin, India and Bangladesh. *Journal of Asian Earth Sciences*, **34 (3)**, pp. 227–244.

Mukherjee, B.B., 1972. Pollen analysis of a few Quaternary deposits of Lower Bengal basin. In *Proceedings of the Seminar on Palaeopalynology and Indian Stratigraphy.* Calcutta University, Calcutta, pp. 357–374.

Najman, Y., Allen, R., Willett, E.A.F., Carter, A., Barfod, D., Garzanti, E., Wijbrans, J., Bickle, M.J., Vezzoli, G., Ando, S. and Oliver, G., 2012. The record of Himalayan erosion preserved in the sedimentary rocks of the Hatia Trough of the Bengal Basin and the Chittagong Hill Tracts, Bangladesh. *Basin Research*, **24 (5)**, pp. 499–519.

Najman, Y.M.R., Pringle, M.S., Johnson, M.R.W., Robertson, A.H.F., 1997. Laser 40Ar/39Ar dating of single detrital muscovite grains from early foreland-basin sedimentary deposits in India: implications for early Himalayan evolution. *Geology*, **25 (6)**, pp. 535–538.

Needs Assessment Working Group (NAWG), 2019. *Cyclone Bulbul 2019 Joint Rapid Assessment, Bangladesh*. Needs Assessment Working Group, Bangladesh.

Neidhardt, H., Biswas, A., Freikowski, D., Majumder, S., Chatterjee, D. and Berner, Z.A., 2013. Reconstructing the sedimentation history of the Bengal Delta Plain by means of geochemical and stable isotopic data. *Applied Geochemistry*, **36**, pp. 70–82.

Nicholls, R.J. and Wilson, T., 2001. Chapter 5: Integrated impacts on coastal areas and river flooding. In: Holman I.P., Loveland P.J. (Eds.), *Regional Climate Change Impact and Response Studies in East Anglia and North West England (RegIS)*. Oxford: UK Climate Impacts Programme (UKCIP), pp. 54–103.

Nicholls, R.J., Hutton, C.W., Lázár, A.N., Allan, A., Adger, W.N., Adams, H., Wolf, J., Rahman, M. and Salehin, M., 2016. Integrated assessment of social and environmental sustainability dynamics in the Ganges-Brahmaputra-Meghna delta, Bangladesh. *Estuarine, Coastal and Shelf Science*, **183**, pp. 370–381.

Niedoroda, A.W., Swift, D.J. and Thorne, J.A., 1989. Modeling shelf storm beds: Controls of bed thickness and bedding sequence. In: *Shelf sandstone, shelf depositional sequence and petroleum accumulation: a symposium*, SEPM, Tulsa, Oklahoma, pp. 15–39.

Nio, S.D. and Yang, C.S., 1991. Diagnostic attributes of clastic tidal deposits: A review. In: Smith, D. G., Reinson, G. E., Zaitlin, B. A., Rahmani, R. A., (Eds.). *Clastic Tidal Sedimentology*. Canadian Society of Petroleum Geologists, Memoir **16**, pp. 3–27.

Nott, J., Chague-Goff, C., Goff, J., Sloss, C. and Riggs, N., 2013. Anatomy of sand beach ridges: evidence from severe Tropical Cyclone Yasi and its predecessors, northeast Queensland, Austra. *Journal of Geophysical Research: Earth Surface*, **118 (3)**, pp. 1710–1719.

Nunn, P.D., 1998. Sea-Level Changes over the Past 1,000 Years in the Pacific. *Journal of Coastal Research*, **14 (1)**, pp. 23–30.

Omura, A. and Hoyanagi, K., 2004. Relationships between composition of organic matter, depositional environments, and sea-level changes in backarc basins, central Japan. *Journal of Sedimentary Research*, **74**, pp. 620–30.

Omura, A., Hoyanagi, K. and Ishikawa, S., 2006. Effect of depositional processes on the origin and composition of organic matter: Examples from the Pleistocene sediments in the Choshi core, Boso Peninsula. *Island Arc*, **15**, pp. 355–365.

Ota, Y., Umitsu, M. and Matsushima, Y., 1990. Recent Japanese Research on Relative Sea Level Changes in the Holocene and Related Problems. *The Quaternary Research*, **29 (1)**, pp. 31–48.

Patrick, R.M. and Reimer, C.W., 1966. *The diatoms of the United States exclusive of Alaska and Hawaii*. vol. 1. Philadelphia, PA: Academy of Natural Sciences of Philadelphia.

Patrick, R.M. and Reimer, C.W., 1975. The diatoms of the United States exclusive of Alaska and Hawaii. vol. 2, Part 1. Philadelphia, PA: Academy of Natural Sciences of Philadelphia.

Pethick, J. and Orford, J.D., 2013. Rapid rise in effective sea-level in southwest Bangladesh: Its causes and Contemporary rates. *Global and Planetary Change*, **111**, pp. 237–245.

Pethick, J., 2012. *Assessing Changes in the Landform and Geomorphology Due to Sea-Level Rise in the Bangladesh Sundarbans*. Report to the World Bank. Mimeo.

Phantuwongraj, S. and Choowong, M., 2012. Tsunamis versus storm deposits from Thailand. *Natural Hazards*, **63**, pp. 31–50.

Phantuwongraj, S., Choowong, M., Nanayama, F., Hisada, K.I., Charusiri, P., Chutakositkanon, V., Pailoplee, S. and Chabangbo, A., 2013. Coastal geomorphic conditions and styles of storm surge washover deposits from Southern Thailand. *Geomorphology*, **192**, pp. 43−58.

Pickering, J.L., Goodbred Jr, S.L., Beam, J.C., Ayers, J.C., Covery, A., Rajapara, H.M. and Singhvi, A.K., 2018. Terrace development in the upper Bengal Basin since the middle Pleistocene: History of Brahmaputra-Jamuna delta construction during multiple highstands. *Basin Resear*ch, **30**, pp. 550–567.

Pickering, J.L., Goodbred Jr, S.L., Reitz, M., Hartzog, T.R., Mondal, D.R. and Hossain, M.S., 2013. Holocene channel avulsions inferred from the Late Quaternary sedimentary record of the Jamuna and Old Brahmaputra river valleys in the upper Bengal delta plain. *Geomorphology*, **227**, pp. 123–136.

Pickering, M.D., Horsburgh, K.J., Blundell, J.R., Hirschi, J.M., Nicholls, R.J., Verlaan, M. and Wells, N.C., 2017. The impact of future sea-level rise on the global tides. *Continental Shelf Research*, **142**, pp. 50–68.

Pilarczyk, J.E., Horton, B.P., Soria, J.L.A., Switzer, A.D., Siringan, F., Fritz, H.M., Khan, N.S., Ildefonso, S., Doctor, A.A. and Garcia, M.L., 2016. Micropaleontology of the 2013 Typhoon Haiyan overwash sediments from the Leyte Gulf, Philippines. *Sedimentary Geology*, **339**, pp. 104-114.

Prasad, M.B.K. and Ramanathan, A.L., 2009. Organic matter characterization in a tropical estuarine-mangrove ecosystem of India: preliminary assessment by using stable isotopes and lignin phenols. *Estuarine, Coastal and Shelf Science*, ***84*** **(4)**, pp. 617–624.

Prasad, M.B.K., Dittmer, T. and Ramathan, A.L., 2010. Organic matter and mangrove productivity. In: Ramanathan, A.L., Bhattacharya, P., Dittmar T., Prasad, M.B.K, Nepaune, B. (eds) *Management and Sustainable Development of the Coastal Zone Environments*. New Dordrecht, Springer, pp. 175–193.

Prasad, M.B.K., Kumar, A., Ramanathan, A.L. and Datta, D.K., 2017. Sources and dynamics of sedimentary organic matter in Sundarban mangrove estuary from Indo-Gangetic delta. *Ecological Processes*, ***6:***8.

Rahman, A.F., Dragoni, D. and El-Masri, B., 2011. Response of the Sundarbans coastline to sea level rise and decreased sediment flow: A remote sensing assessment. *Remote Sensing of Environment*, ***115***, pp. 3121–3128.

Rahman, M., Dustegir, M., Karim, R., Haque, A., Nicholls, R.J., Darby, S.E., Nakagawa, H., Hossain, M., Dunn, F.E. and Akter, M., 2018. Recent sediment flux to the Ganges-Brahmaputra-Meghna delta system. *Science of the total environment,* **643**, pp. 1054–1064.

Rahman, M.A., Mitra, M.C. and Akter, A., 2013. Investigation on erosion of Kuakata sea beach and its protection design by artificial beach nourishment. *Journal of Civil Engineering (IEB)*, **41 (1)**, pp. 1–12.

Ranjan, R.K., Routh, J., Ramanathan, A.L. and Klump, J.V., 2011. Elemental and stable isotope records of organic matter input and its fate in the Pichavaram mangrove–estuarine sediments (Tamil Nadu, India). *Marine Chemistry*, **126 (1-4)**, pp. 163–172.

Rashid, T., Suzuki, S., Sato, H., Monsur, M.H. and Saha, S.K., 2013. Relative sea-level changes during the Holocene in Bangladesh. *Journal of Asian Earth Sciences*, **64**, pp. 136–150.

Ray, R. and Shahraki, M., 2016, Multiple sources driving the organic matter dynamics in two contrasting tropical mangroves. *Science of Total Environment*, **571**, pp. 218–227.

Ray, R. and Shahraki, M., 2016. Multiple sources driving the organic matter dynamics in two contrasting tropical mangroves. *Science of the Total Environment*, ***571***, pp. 218–227.

Ray, R., Rixen, T., Baum, A., Malik, A., Gleixner, G. and Jana, T.K., 2015. Distribution, sources and biogeochemistry of organic matter in a mangrove dominated estuarine system (Indian Sundarbans) during the pre-monsoon. *Estuarine, Coastal and Shelf Science*, **167**, pp. 404–413.

Rennel, J., 1809. An Account of the Ganges and Burrampooter Rivers (Anno 1781, vol. LXXI), *The Philosophical Transactions of the Royal Society of London*, XV, pp. 39–50.

Rice, S.K., 2007. Suspended sediment transport in the Ganges-Brahmaputra River System, Bangladesh. College Station: Texas A&M University.

Rogers, K.G., Goodbred Jr, S.L. and Mondal, D.R., 2013. Monsoon sedimentation on the 'abandoned'tide-influenced Ganges–Brahmaputra delta plain. *Estuarine, Coastal and Shelf Science*, ***131***, pp. 297–309.

Rokni, K., Ahmad, A., Selamat, A. and Hazini, S., 2014. Water feature extraction and change detection using multitemporal Landsat imagery. *Remote sensing*, ***6* (5)**, pp. 4173–4189.

Rossi, V.M., Paterson, N.W., Helland-Hansen, W., Klausen, T.G. and Eide, C.H., 2019. Mud-rich delta-scale compound clinoforms in the Triassic shelf of northern Pangea (Havert Formation, south-western Barents Sea). *Sedimentology*, ***66* (6)**, pp. 2234–2267.

Round, F.E., Crawford, R.M. and Mann D.G., 1990. T*he Diatoms: Biology and Morphology of the Genera*. Cambridge University Press.

Roy, A.B. and Chatterjee, A., 2015. Tectonic framework and evolutionary history of the Bengal Basin in the Indian subcontinent. *Current Science*, **109 (2)**, pp. 271–279.

Rudra, K., 1981. Identification of the ancient mouths of the Ganga as described by Ptolemy. *Geographical Review India*, **43 (2)**, pp. 97–104.

Saintilan, N., Rogers, K., Mazumder, D. and Woodroffe, C., 2013. Allochthonous and autochthonous contributions to carbon accumulation and carbon store in southeastern Australian coastal wetlands. *Estuarine, Coastal and Shelf Science*, **128**, pp. 84–92.

Sarkar, A., Sengupta, S., McArthur, J.M., Ravenscroft, P., Bera, M.k., Bhushan, R., Samanta, A., Agrawal, S., 2009. Evolution of Ganges–Brahmaputra western delta plain: Clues from sedimentology and carbon isotopes. *Quaternary Science Reviews*, **28**, 2564–2581.

Sarwar, M.G.M. and Woodroffe, C.D., 2013. Rates of shoreline change along the coast of Bangladesh. *Journal of coastal conservation*, **17 (3)**, pp. 515–526.

Sedgwick, P.E. and Davis Jr, R.A., 2003, Stratigraphy of washover deposits in Florida: implications for recognition in the stratigraphic record. *Marine Geology,* **200,** pp. 31−48.

Sesoren, A., 1984. Geological Interpretation on Landsat Imagery of the Bangladesh Ganges Delta. *ITC Journal, The Netherlands*, **3**, pp. 229–232.

Shaha, D.C. and Cho, Y.K., 2016. Salt plug formation caused by decreased river discharge in a multi-channel estuary. *Scientific Reports*, ***6*** **(1)**, pp.1–11.

Shibayama, T., Tajima, Y., Kakinuma, T., Nobuoka, H., Yasuda, T., Hsan, R.A., Rahman, M., Islam, M.S., 2009. Field survey of storm surge disaster due to Cyclone Sidr in Bangladesh. Proc. of Coastal, Dynamics Conference, Tokyo, 7–11, September 2009.

Shibly, A.M. and Takewaka, S., 2012. Morphological changes along Bangladesh coast derived from satellite images. *Proceedings of Coastal Engineering*, **3**, pp. 41–45.

Shigeno, K. and Nanayama. F., 2016. Sedimentary Process of a Small Sandy Event Deposit due to a Storm Surge and Storm Waves Generated by a Typhoon: An Example from the Hirahama Coastal Lowland along the Western Example from the Hirahama Coastal Lowland along the Western Coast of the Oshima Peninsula between 09: 00 September 18 and 01: 00 September 19, 1959. *Journal of Geography (chigaku zasshi)*, **125 (5),** pp. 747-762.

Sincavage, R., Goodbred Jr, S.L., and Pickering, J., 2018. Holocene Brahmaputra River path selection and variable sediment bypass as indicators of fluctuating hydrologic and climate conditions in Sylhet Basin, Bangladesh. *Basin Research*, ***30*** **(2)**, pp. 302–320.

Singh, O., 2007. Long-term trends in the frequency of severe cyclones of Bay of Bengal: Observations and Simulations. *Mausam*, **58 (1)**, pp. 59–66.

Soria, J.L., Switzer, A.D., Pilarczky, J.E., Siringan, F.P., Khan, N.S. and Fritz, H.M., 2017. Typhoon Haiyan overwash sediments from Leyte Gulf coastlines show local spatial variations with hybrid storm and tsunami signatures. *Sedimentary Geology,* **358**, pp. 121–138.

Soria, J.L.A., Switzer, A.D., Pilarczyk, J.E., Tang, H., Weiss, R., Siringan, F., Manglicmot, M., Gallentes, A., Lau, A.A., Cheong, A.Y.L. and Koh, T.W.L., 2018. Surf beat-induced overwash during Typhoon Haiyan deposited two distinct sediment assemblages on the carbonate coast of Hernani, Samar, central Philippines. *Marine Geology,* ***396***, pp. 215−230.

Spalding, M., 2010. World atlas of mangroves. Abingdon: Routledge.

Stanley, D.J., Hait, A.K., 2000. Holocene depositional patterns, neotectonics and Sundarban mangroves in the western Ganges-Brahmaputra delta. *Journal of Coastal Research,* **16**, **(1)**, pp. 26–39.

Steckler, M.S., Akhter, S.H. and Seeber, L., 2008. Collision of the Ganges–Brahmaputra Delta with the Burma Arc: implications for earthquake hazard. *Earth and Planetary Science Letters*, **273 (3–4),** pp. 367–378.

Steckler, M.S., Nooner, S.L., Akhter, S.H., Chowdhure, S.K., Bettadpur, S., Seeber, L., Kogan, M.G., 2010. Modeling Earth deformation from monsoonal flooding in Bangladesh using hydrographic, GPS, and Gravity Recovery and Climate Experiment (GRACE) data. *Journal of Geophysical Research,* **115**, B08407.

Sunder, S., Ramsankaran, R. and Ramakrishnan, B. 2017. Inter-comparison of remote sensing sensing-based shoreline mapping techniques at different coastal stretches of India. *Environmental monitoring and assessment*, **189 (6)**, 290.

Swift, D.J.P. and Thorne, J.A., 1991. Sedimentation on Continental Margins, I: General Model for Shelf Sedimentation. In: Swift, D.J.P., Oertel, G.F., Tillman, R.W., Thorne, J.A.A. (eds) *Shelf sand and sandstone bodies: geometry, facies and sequence stratigraphy*. Spec. Publs, Int. Ass. Sediment. **14**, 3–31.

Switzer, A.D. Jones, B.G., 2008. Setup, deposition, and sedimentary characteristics of two storm overwash deposits, Abrahams Bosom Beach, Southeastern Australia. *Journal of Coastal Research*, **24**, pp. 189−200.

Switzer, A.D., 2013. Measuring and analyzing particle size in a geomorphic context. In: Shroder, J. (Ed. in Chief), Switzer, A.D., Kennedy, D.M. (Eds.), Treatise on Geomorphology. *Academic Press, San Diego, CA*, Methods in Geomorphology, **14**, pp. 224–242.

Switzer, A.D., Pucillo, K., Haredy, R.A., Jones, B.G. and Bryant, E.A., 2005. Sea level, storm, or tsunami: enigmatic sand sheet deposits in a sheltered coastal embayment from southeastern New South Wales, Australia. *Journal of Coastal Research*, **21**, pp.655−663.

Switzer, A.D. and Pile J., 2015. Grain Size Analysis. In: Handbook of Sea-Level Research. John Wiley and Sons, Ltd, Chichester, UK, pp. 331−346.

Syvitski, J.P. and Saito, Y., 2007. Morphodynamics of deltas under the influence of humans. *Global and Planetary Change*, **57 (3–4)**, pp. 261–282.

Syvitski, J.P., Kettner, A.J., Overeem, I., Hutton, E.W., Hannon, M.T., Brakenridge, G.R., Day, J., Vörösmarty, C., Saito, Y., Giosan, L. and Nicholls, R.J., 2009. Sinking deltas due to human activities. *Nature Geoscience*, ***2*(10),** pp. 681–686.

Syvitski, J.P.M. and Kettner, A., 2011. Sediment flux and the Anthropocene. *Philosophical Transactions of the Royal Society A: Mathematical, Physical and Engineering Sciences*, **369 (1938)**, pp. 957–975.

Takagi, H., Thao, N.D. and Anh, L.T., 2016. Sea-level rise and land subsidence: impacts on flood projections for the Mekong Delta's largest city. *Sustainability*, ***8* (9)**, 959.

Tanner, W.F., 1995. Origin of beach ridges and swales. Marine Geology, **129 (1–2),** pp. 149–161.

Teng, F., Shen, Q., Huang, W., Ginis, I. and Cai, Y., 2017. Characteristics of river flood and storm surge interactions in a tidal river in Rhode Island, USA. *Procedia IUTAM*, **25**, pp. 60–64.

Tessier, B., 1998. Tidal cycles: annual versus semi-lunar records. Tidalites: Processes & Products, Clark R. Alexander, Richard A. Davis, Vernon J. Henry. Vol. 61, SEPM Soc. Sed. Geol. Tulsa, Oklahoma.

Thimdee, W., Deein, G., Sangrungruang, C., Nishioka, J. and Matsunaga, K., 2003. Sources and fate of organic matter in Khung Krabaen Bay (Thailand) as traced by $\delta^{13}C$ and C/N atomic ratios. *Wetlands*, **23 (4)**, pp. 729–738.

Turner, R.E., Baustian, J.J., Swenson, E.M. and Spicer, J.S., 2006. Wetland sedimentation from Hurricanes Katrina and Rita. *Science*, **314 (5798)**, pp. 449–452.

Uddin A. and Lundberg, N., 1999. A paleo-Brahmaputra? Subsurface lithofacies analysis of Miocene deltaic sediments in the Himalayan–Bengal system, Bangladesh. *Sedimentary Geology*, **123,** pp. 239–254.

Umitsu, M., 1985. Natural levees and landform evolutions in the Bengal lowland. *Geographical Review of Japan*, **58, Series B, (2)**, pp. 149-164.

Umitsu, M., 1987. Late Quaternary sedimentary environments and landform evolution in the Bengal lowland, *Geographical Review of Japan*, **60, Series B, (2)**, pp. 164-178.

Umitsu, M., 1993. Late Quaternary Sedimentary Environments and Landforms in the Ganges Delta. *Sedimentary Geology*, **83**, pp. 177–186.

Unger Holtz, T.S., 2007. Introductory digital image processing: A remote sensing perspective. *Association of Environmental & Engineering Geologists*, **13**, pp. 89–90.

Vinayachandran, P.N., Murty, V.S.N., Babu, V.R., 2002. Observations of barrier layer formation in the Bay of Bengal during summer monsoon. *Journal of Geophysical Research: Oceans,* **107 (C12).**

Walker, R.G., 1984. Shelf and shallow marine sands, Facies models. *Geoscience Canada*, **1**, pp. 141–170.

Wang, L., Bianchette, T.A. and Liu, K., 2019. Diatom Evidence of a Paleohurricane-Induced Coastal Flooding Event in Weeks Bay, Alabama, USA. *Journal of Coastal Research*, ***35* (3)**, pp. 499–508.

Warrick, R.A. and Ahmed, Q.K., 1996. *The Implications of Climate and Sea-level Change for Bangladesh.* The Netherlands: Kluwer Academic Publications.

Watanabe, M., Bricker, J.D., Goto, K. And Imamura, F., 2017. Factors responsible for the limited inland extent of sand deposits on Leyte Island during 2013 Typhoon Haiyan. *Journal of Geophysical Research, Oceans*, **122(4)**, pp. 2795−2812.

Watson, A.J. and Whitfield, M., 1985. Composition of particles in the global ocean. *Deep-Sea Research*, **32**, pp. 1023–1039.

Wheeler, H.E., 1964. Base-level, Lithosphere Surface, and Time Stratigraphy. *Geological Society of America Bulletin*, **75**, pp. 599–610.

Williams, H. and Flanagan, W., 2009. Contribution of Hurricane Rita storm surge deposition to long-term sedimentation in Louisiana coastal woodlands and marshes. *Journal of Coastal Research*, **56**, pp. 1671–1675.

Williams, H.F., 2009, Stratigraphy, sedimentology, and microfossil content of Hurricane Rita storm surge deposits in southwest Louisiana. *Journal Coastal Researh, **25**,* pp. 1041−1051.

Williams, H.F., 2010. Storm surge deposition by Hurricane Ike on the McFaddin National Wildlife Refuge, Texas: implications for paleotempestology studies. *Journal of Foraminiferal Research, **40***, pp. 210−219.

Wilson, C.A. and Goodbred Jr, S.L., 2015. Construction and Maintenance of the Ganges-Brahmaputra-Meghna Delta: Linking Process, Morphology, and Stratigraphy. *The Annual Review of Marine Science,* **7**, pp. 67–88.

Winterwerp, J. and Giardino, A., 2012. Assessment of increasing freshwater input on salinity and sedimentation in the Gorai river system. World Bank Project, Deltares, Netherlands.

Woodroffe, C.D., Thom, B.G., Chappell, J., 1985. Development of widespread mangrove swamps in mid-Holocene times in northern Australia. *Nature,* **317**, pp. 711–713.

Xiong, H., Huang, G., Fu, S. and Qian, P., 2018. Progress in the Study of Coastal Storm Deposits. *Ocean Science Journal*, **53 (2)**, pp. 149–164.

Yang, B., Dalrymple, R. and Chun, S., 2005. Sedimentation on a wave-dominated, open-coast tidal flat, south-western Korea: summer tidal flat–winter shoreface. *Sedimentology,* **52 (2)**, pp. 235–252.

Yang, C.S. and Nio, S.D., 1985. The estimation of palaeo hydrodynamic processes from subtidal deposits using time series analysis methods. *Sedimentology*, **32 (1)**, pp. 41–57.

Appendix I A: Supplementary results of laboratory analyses for Chapter 3

Results of TN, TOC, TOC/TN, TS, and $\delta^{13}C$ values against the depth of sedimentary samples at Dhigholia and Batiaghata sites of Khulna district.

Sl No	Sample ID	Log depth (in cm)	TN (%)	TOC (%)	TOC/TN	TS	$\delta^{13}C$ (‰)
Dhigholia D-1-1 (Location: 89°33′48.7″E ; 22°54′13.5″N)							
1	D-1/L-1/96	6	0.03	0.41	12.63	0.04	-22.55
2	D-1/L-1/90	22	0.03	0.26	11.23	0.03	
3	D-1/L-1/87	29	0.04	0.36	9.63	0.02	-20.26
4	D-1/L-1/80	47	0.03	0.31	9.31	0.02	
5	D-1/L-1/77	54	0.03	0.31	9.10	0.02	-18.22
6	D-1/L-1/72	67	0.03	0.22	8.69	0.03	
7	D-1/L-1/70	73	0.03	0.25	9.76	0.02	
8	D-1/L-1/68	77	0.02	0.13	8.52	0.02	-19.92
9	D-1/L-1/64	87	0.03	0.31	8.97	0.02	
10	D-1/L-1/60	98	0.03	0.32	9.43	0.02	-19.59
11	D-1/L-1/56	108	0.03	0.32	9.40	0.02	
12	D-1/L-1/52	118	0.05	0.53	10.04	0.03	-20.77
13	D-1/L-1/48	129	0.03	0.31	9.24	0.03	
14	D-1/L-1/44	139	0.03	0.26	8.74	0.02	-19.00
15	D-1/L-1/36	159	0.03	0.32	9.38	0.02	-18.70
16	D-1/L-1/32	169	0.03	0.31	8.91	0.02	
17	D-1/L-1/28	179	0.03	0.33	9.66	0.03	-18.57
18	D-1/L-1/24	190	0.04	0.31	8.74	0.03	
19	D-1/L-1/20	200	0.03	0.33	9.58	0.03	-18.09
20	D-1/L-1/16	210	0.03	0.23	8.47	0.02	
21	D-1/L-1/12	220	0.05	0.40	8.20	0.02	-19.63
22	D-1/L-1/8	230	0.02	0.16	8.88	0.02	
23	D-1/L-1/5	237	0.02	0.21	9.23	0.02	-20.33
24	D-1/L-1/2	245	0.02	0.17	7.16	0.03	-20.86
Dhigholia D-1-2 (Location: 89°34′10.5″E; 22°53′11.1″N)							
1	D-1/L-2/34	5	0.03	0.39	12.07	0.03	
2	D-1/L-2/30	14	0.03	0.37	11.31	0.03	-18.30
3	D-1/L-2/27	21	0.03	0.31	9.86	0.02	
4	D-1/L-2/24	32	0.04	0.42	10.94	0.03	-20.47
5	D-1/L-2/21	37	0.04	0.41	11.34	0.03	
6	D-1/L-2/18	44	0.05	0.43	9.32	0.04	-20.45
7	D-1/L-2/16	49	0.05	0.47	10.23	0.07	
8	D-1/L-2/12	60	0.05	0.55	10.78	0.05	-22.06
9	D-1/L-2/09	67	0.03	0.29	9.95	0.02	
10	D-1/L-2/06	75	0.03	0.25	9.15	0.02	
11	D-1/L-2/1	87	0.03	0.33	9.37	0.02	-19.57
Dhigholia D-1-3 (Location: 89°34′04.8″E; 22°52′24.4″N)							
1	D-1/L-3/15	0	0.04	0.45	12.42	0.03	-17.84
2	D-1/L-3/12	8	0.04	0.43	11.67	0.02	
3	D-1/L-3/8	18	0.04	0.54	13.23	0.03	-19.20
4	D-1/L-3/4	28	0.05	0.51	9.94	0.03	
5	D-1/L-3/0	38	0.04	0.41	9.75	0.02	
6	D-1/L-3/55	55	0.03	0.29	9.48	0.02	
7	D-1/L-3/58	58	0.03	0.28	8.93	0.02	
8	D-1/L-3/63	63	0.03	0.26	8.99	0.03	-18.97
9	D-1/L-3/67	67	0.03	0.29	8.75	0.02	
10	D-1/L-3/72	72	0.03	0.26	8.59	0.02	-19.10

Sl No	Sample ID	Log depth (in cm)	TN (%)	TOC (%)	TOC/TN	TS	$\delta^{13}C$ (‰)
11	D-1/L-3/76	76	0.03	0.26	9.34	0.02	
12	D-1/L-3/82	82	0.03	0.25	9.13	0.02	
13	D-1/L-3/85	85	0.02	0.17	8.21	0.02	
14	D-1/L-3/96	96	0.03	0.23	8.10	0.02	-19.50
15	D-1/L-3/102	102	0.03	0.22	8.44	0.02	
Dhigholia D-1-4 (Location: 89°33′37.1″E; 22°51′05.2 ″N)							
1	D-1/L-4/36	3	0.05	0.61	12.78	0.07	-15.61
2	D-1/L-4/32	14	0.04	0.50	11.55	0.03	
3	D-1/L-4/30	19	0.04	0.38	9.07	0.04	
4	D-1/L-4/28	24	0.03	0.26	8.13	0.04	-21.14
5	D-1/L-4/24	34	0.03	0.25	9.69		
6	D-1/L-4/22	39	0.04	0.36	9.60	0.01	
7	D-1/L-4/20	44	0.04	0.51	11.24	0.09	-22.07
8	D-1/L-4/18	49	0.03	0.30	9.04	0.05	
9	D-1/L-4/15	57	0.06	0.63	9.88	0.09	
10	D-1/L-4/12	65	0.04	0.33	8.38	0.04	-21.37
11	D-1/L-4/9	72	0.04	0.38	9.21	0.06	
12	D-1/L-4/6	80	0.05	0.43	8.77	0.05	-20.89
13	D-1/L-4/3	87	0.05	0.40	8.35	0.05	
14	D-1/L-4/0	95	0.03	0.25	7.96	0.03	-20.83
Dhigholia D-1-5 (Location: 89°33′41″E; 22°50′45 ″N)							
1	D-1/L-5-2/25	6	0.06	0.78	13.38	0.03	
2	D-1/L-5-2/22	14	0.06	1.13	17.97	0.03	-24.18
3	D-1/L-5-2/19	22	0.07	0.88	13.30	0.03	
4	D-1/L-5-2/16	29	0.06	0.91	14.63	0.03	-23.34
5	D-1/L-5-2/13	37	0.07	0.79	11.88	0.03	
6	D-1/L-5-2/06	55	0.05	0.42	8.70	0.02	
7	D-1/L-5-2/04	60	0.06	0.48	8.69	0.02	-21.50
8	D-1/L-5-2/0	68	0.04	0.42	9.67	0.02	
9	D-1/L-5-1/23	92	0.04	0.28	7.90	0.02	
10	D-1/L-5-1/18	104	0.02	0.17	7.94	0.03	-18.94
11	D-1/L-5-1/16	110	0.02	0.19	7.99	0.02	
12	D-1/L-5-1/12	119	0.02	0.17	8.65	0.02	
13	D-1/L-5-1/09	127	0.02	0.20	8.40	0.02	-18.44
14	D-1/L-5-1/06	135	0.03	0.21	7.38	0.02	
15	D-1/L-5-1/04	140	0.04	0.29	7.53	0.02	-19.59
16	D-1/L-5-1/0	150	0.04	0.27	7.24	0.03	-19.22
Batiaghata B-2-1 (Location: 89°31′28.7″E; 22°44′46 ″N)							
1	B-2/L-1/10	10	0.04	0.52	11.72	0.11	-22.25
2	B-2/L-1/22	22	0.05	0.51	10.64	0.09	-22.31
3	B-2/L-1/40	40	0.08	0.54	6.57	0.09	-22.12
4	B-2/L-1/47	47	0.07	0.69	9.33	0.16	
5	B-2/L-1/57	57	0.07	0.71	10.42	0.18	
6	B-2/L-1/65	65	0.06	0.67	11.25	0.17	-21.35
7	B-2/L-1/80	80	0.08	0.79	10.49	0.21	
8	B-2/L-1/92	92	0.09	0.99	11.31	0.26	
9	B-2/L-1/105	105	0.10	1.39	14.06	0.29	-23.01
10	B-2/L-1/111	111	0.07	0.73	10.52	0.16	

Sl No	Sample ID	Log depth (in cm)	TN (%)	TOC (%)	TOC/TN	TS	$\delta^{13}C$ (‰)
11	B-2/L-1/124	124	0.05	0.49	9.09	0.07	
12	B-2/L-1/133	133	0.04	0.40	8.98	0.10	-21.35
13	B-2/L-1/145	145	0.06	0.57	10.24	0.11	
14	B-2/L-1/153	153	0.08	0.97	11.80	0.11	-22.96
15	B-2/L-1/163	163	0.11	1.71	15.99	0.24	
16	B-2/L-1/173	173	0.16	2.98	18.37	0.35	-26.29
Batiaghata B-2-2 (Location: 89˚31´05.3˝E; 22˚41´23.7 ˝N)							
1	B-2/L-2/5	5	0.06	0.47	8.04	0.03	
2	B-2/L-2/18	18	0.05	0.49	9.02	0.03	-19.90
3	B-2/L-2/28	28	0.06	0.50	8.52	0.03	
4	B-2/L-2/38	38	0.07	0.61	8.76	0.03	
5	B-2/L-2/48	48	0.08	0.85	10.11	0.05	-21.79
6	B-2/L-2/58	58	0.16	2.20	13.37	0.14	
7	B-2/L-2/68	68	0.25	4.59	18.25	0.41	-24.04
8	B-2/L-2/78	78	0.29	6.67	23.11	0.97	-26.83
9	B-2/L-2/88	88	0.23	4.84	20.80	1.10	
10	B-2/L-2/98	98	0.19	4.14	21.30	1.72	-26.54
11	B-2/L-2/106	106	0.26	4.16	16.12	1.54	-24.92
12	B-2/L-2/112	112	0.39	5.78	14.84	1.69	
13	B-2/L-2/123	123	0.21	2.93	14.00	1.06	
14	B-2/L-2/138	138	0.22	2.92	13.44	0.79	-26.07
15	B-2/L-2/148	148	0.13	3.01	13.92	0.80	
16	B-2/L-2/158	158	0.04	3.11	14.40	0.56	-22.72
17	B-2/L-2/166	166	0.16	2.20	13.65	0.44	
Batiaghata B-1-3 (Location: 89˚31´28.7˝E; 22˚44´46 ˝N)							
1	B-2/L-3/5	5	0.09	0.75	8.78	0.19	-20.88
2	B-2/L-3/13	13	0.10	1.07	11.04	0.33	
3	B-2/L-3/23	23	0.08	0.68	8.60	0.06	
4	B-2/L-3/33	33	0.08	0.67	8.96	0.05	-19.09
5	B-2/L-3/43	43	0.08	0.70	9.38	0.05	
6	B-2/L-3/53	53	0.09	0.91	9.89	0.04	
7	B-2/L-3/63	63	0.09	0.87	10.17	0.04	-21.44
8	B-2/L-3/73	73	0.13	1.38	11.04	0.07	
9	B-2/L-3/83	83	0.09	1.20	13.14	0.07	-24.22
10	B-2/L-3/93	93	0.12	1.90	16.46	0.16	
11	B-2/L-3/103	103	0.14	2.16	15.44	0.21	
12	B-2/L-3/113	113	0.16	2.49	15.79	0.50	-25.21
13	B-2/L-3/123	123	0.18	2.61	14.38	0.71	
14	B-2/L-3/133	133	1.09	13.39	12.30	3.67	
15	B-2/L-3/143	143	0.76	10.64	14.03	3.19	
16	B-2/L-3/153	153	0.82	11.25	13.71	2.72	-25.55
17	B-2/L-3/163	163	0.38	5.31	13.91	1.00	
18	B-2/L-3/173	173	0.38	4.82	12.64	1.72	-24.19
19	B-2/L-3/183	183	0.25	3.16	12.73	0.87	
20	B-2/L-3/193	193	0.18	2.26	12.63	0.63	-25.04

Appendix I B: Supplementary results of laboratory analyses for Chapter 4

Results of mean grain size, TOC, TN, TOC/TN, and $\delta^{13}C$ values against the depth of geological core at Haringhata coastal region of Barguna district.

Sl. No.	Sample ID	Depth (cm)	Mean grain size (µm)	TOC (%)	TN (%)	TOC/TN	$\delta^{13}C$ (‰)
Site 1 (Latitude: 21°57'40.62"N; Longitude: 89°58'56.10"E)							
1	D2L1-01	0	131.50	0.422	0.035	12.057	
2	D2L1-02	3	84.18	0.556	0.040	13.900	-23.456
3	D2L1-03	8	76.89	0.419	0.031	13.516	
4	D2L1-04	13	102.70	0.581	0.037	15.703	-22.671
5	D2L1-05	18	101.20	0.744	0.044	16.909	
6	D2L1-06	23	91.64	0.733	0.050	14.660	
7	D2L1-07	28	111.30	0.495	0.046	10.761	-20.739
8	D2L1-08	33	109.50	0.362	0.034	10.647	-20.183
9	D2L1-09	38	87.08	0.431	0.039	11.051	
10	D2L1-10	43	66.82	0.513	0.034	15.088	-22.532
11	D2L1-11	48	92.97	0.865	0.037	18.804	-24.351
12	D2L1-12	53	51.78	0.567	0.047	12.064	
13	D2L1-13	58	70.21	0.463	0.039	11.872	-18.816
14	D2L1-14	63	44.88	0.476	0.040	11.900	
15	D2L1-15	68	59.88	0.436	0.041	10.634	-20.096
16	D2L1-16	73	48.39	0.437	0.041	10.659	
17	D2L1-17	78	38.54	0.278	0.029	9.586	-19.691
18	D2L1-18	93	29.22	0.256	0.029	8.828	
19	D2L1-19	97	29.63	0.359	0.035	10.257	-22.147
Site 2 (Latitude: 21°57'44.03"N; Longitude: 89°58'55.89"E)							
1	D2L2-01	0	81.37	0.689	0.061	11.295	
2	D2L2-02	3	63.38	0.253	0.025	10.120	-20.761
3	D2L2-03	6	58.74	0.465	0.036	12.917	
4	D2L2-04	10	58.94	0.355	0.033	10.758	-19.893
5	D2L2-05	13	49.50	0.387	0.032	12.094	
6	D2L2-06	16	58.55	0.313	0.025	12.520	
7	D2L2-07	20	53.32	0.292	0.026	11.231	-19.046
8	D2L2-08	23	44.46	0.322	0.026	12.385	
9	D2L2-09	26	63.41	0.183	0.020	9.150	
10	D2L2-10	30	44.55	0.231	0.026	8.885	-20.803
11	D2L2-11	36	48.19	0.222	0.023	9.652	
12	D2L2-12	40	35.99	0.388	0.032	12.125	-19.248
13	D2L2-13	43	37.20	0.219	0.021	10.429	
14	D2L2-14	48	67.71	0.289	0.029	9.966	-18.806
15	D2L2-15	53	52.99	0.339	0.033	10.273	
16	D2L2-16	63	35.83	0.332	0.030	11.067	
17	D2L2-17	68	43.40	0.418	0.037	11.297	-23.545
18	D2L2-18	78	32.05	0.251	0.027	9.296	
19	D2L2-19	83	42.61	0.325	0.030	10.833	-23.004
20	D2L2-20	88	37.39	0.217	0.019	11.421	
21	D2L2-21	93	41.60	0.209	0.021	9.952	
22	D2L2-22	98	34.54	0.191	0.020	9.550	-22.102

Sl. No.	Sample ID	Depth (cm)	Mean grain size (µm)	TOC (%)	TN (%)	TOC/TN	$\delta^{13}C$ (‰)
Site 3 (Latitude: 21°57'47.21"N; Longitude: 89°58'55.89"E)							
1	D2L3-01	0	84.12	0.226	0.021	10.762	
2	D2L3-02	4	78.60	0.340	0.032	10.625	-19.242
3	D2L3-03	7	56.53	0.240	0.024	10.000	
4	D2L3-04	10	60.88	0.329	0.028	11.750	
5	D2L3-05	14	63.37	0.198	0.020	9.900	-19.155
6	D2L3-06	17	63.47	0.574	0.043	13.349	
7	D2L3-07	20	50.95	0.247	0.026	9.500	
8	D2L3-08	24	56.12	0.148	0.020	7.400	-18.955
9	D2L3-09	27	61.20	0.234	0.026	9.000	
10	D2L3-10	30	67.11	0.197	0.022	8.955	
11	D2L3-11	34	67.36	0.213	0.023	9.261	-19.804
12	D2L3-12	37	68.11	0.250	0.026	9.615	
13	D2L3-13	40	70.40	0.305	0.031	9.839	-18.839
14	D2L3-14	44	41.83	0.188	0.022	8.545	
15	D2L3-15	47	46.82	0.148	0.019	7.789	
16	D2L3-16	50	83.37	0.135	0.016	8.438	
17	D2L3-17	54	50.29	0.200	0.023	8.696	-21.479
18	D2L3-18	57	48.90	0.211	0.023	9.174	
19	D2L3-19	60	47.54	0.148	0.021	7.048	
20	D2L3-20	64	51.80	0.177	0.020	8.850	-21.889
21	D2L3-21	67	40.16	0.355	0.026	13.654	
22	D2L3-22	70	53.35	0.214	0.023	9.304	
23	D2L3-23	74	81.41	0.300	0.032	9.375	-23.107
24	D2L3-24	77	60.93	0.376	0.033	11.394	
25	D2L3-25	80	48.92	0.389	0.035	11.114	
26	D2L3-26	83	38.40	0.325	0.030	10.833	-22.602
27	D2L3-27	90	44.91	0.282	0.024	11.750	
28	D2L3-28	95	33.03	0.287	0.028	10.250	
29	D2L3-29	100	45.57	0.174	0.019	9.158	-22.628
30	D2L3-30	105	36.56	0.243	0.024	10.125	
31	D2L3-31	110	35.14	0.221	0.022	10.045	
32	D2L3-32	115	37.25	0.233	0.025	9.320	-23.123
33	D2L3-33	120	41.28	0.152	0.017	8.941	
34	D2L3-34	125	51.85	0.239	0.024	9.958	
35	D2L3-35	130	44.47	0.159	0.019	8.368	-22.386

Appendix I C: Supplementary results of laboratory analyses for Chapter 5

Results of mean grain size, sorting, standard deviation, TOC, TN, TOC/TN, and $\delta^{13}C$ values of sedimentary samples collected from Kuakata coast, Patuakhali.

Sample ID	Avg. Depth	Mean grain size (µm)	Sorting (φ)	Std. Dev. (µm)	TOC (%)	TN (%)	TOC/TN	$\delta^{13}C$ (‰)
A-1-1	1	37.06	2.48	60.99	1.126	0.107	10.52	
A-1-2	5	39.09	2.50	66.68	0.955	0.082	11.65	
A-1-3	10	35.84	2.11	61.44	0.551	0.057	9.67	
A-1-4	15	81.06	1.89	82.56	0.478	0.059	8.10	
A-1-5	18	129.00	1.55	98.78	-	-	-	
A-1-6	19	130.70	1.43	102.00	-	-	-	
A-1-7	20	140.10	1.26	95.55	0.172	0.027	6.370	
A-1-8	21	129.90	1.01	71.74	-	-	-	
A-1-9	22	143.50	0.73	73.20	-	-	-	
A-1-10	23	141.50	0.95	80.80	-	-	-	
A-1-11	25	34.05	1.67	47.79	0.254	0.035	7.26	
A-1-12	30	28.29	2.20	40.64	0.284	0.035	8.11	
A-1-13	35	16.27	1.68	14.54	0.273	0.032	8.53	
A-1-14	40	17.65	1.70	20.55	0.228	0.025	9.12	
A-5-1	1	70.54	2.45	72.60	0.570	0.057	10.000	
A-5-2	5	69.70	2.43	100.90	0.615	0.063	9.762	
A-5-3	10	109.80	2.24	187.70	0.506	0.054	9.370	
A-5-4	15	14.74	1.66	13.59	0.264	0.033	8.000	
A-5-5	20	12.01	1.63	11.77	0.396	0.046	8.609	
A-5-6	25	12.38	1.65	11.88	0.377	0.046	8.196	
A-5-7	30	19.63	1.61	25.08	0.326	0.034	9.588	
B-1-1	1	47.08	2.48	60.99	0.529	0.061	8.672	
B-1-2	5	66.57	2.51	95.67	0.669	0.069	9.696	-20.664
B-1-3	7	95.72	2.11	86.94				
B-1-4	8	95.35	1.96	70.63	0.334	0.037	9.027	-19.457
B-1-5	9	100.90	1.89	70.84	0.272	0.033	8.242	
B-1-6	10	86.46	2.19	107.00	0.295	0.035	8.429	
B-1-7	11	96.04	1.94	72.00	0.239	0.029	8.241	-19.427
B-1-8	12	131.90	1.01	57.19	-	-	-	
B-1-9	13	129.80	1.07	58.65	-	-	-	
B-1-10	14	123.00	1.32	67.64	-	-	-	
B-1-11	15	148.00	0.73	56.08	0.154	0.028	5.500	-18.806
B-1-12	16	151.90	0.70	55.49	-	-	-	
B-1-13	17	153.20	0.63	53.73	-	-	-	
B-1-14	18	149.50	0.99	87.34	-	-	-	
B-1-15	19	165.20	0.62	79.27	-	-	-	
B-1-16	20	221.80	1.04	275.10	-	-	-	
B-1-17	21	43.82	2.36	60.71	0.237	0.034	6.971	-19.523
B-1-18	25	14.31	1.61	13.03	0.248	0.036	6.889	
B-1-19	30	13.84	1.64	11.99	0.230	0.033	6.970	-20.331
B-1-20	35	14.37	1.68	13.63	0.272	0.035	7.771	
B-1-21	40	14.69	1.65	13.49	0.241	0.028	8.607	-21.003
B-1-22	45	17.60	1.65	20.05	0.261	0.032	8.156	

Sample ID	Avg. Depth	Mean grain size (µm)	Sorting (φ)	Std. Dev. (µm)	TOC (%)	TN (%)	TOC/TN	$\delta^{13}C$ (‰)
B-5-1	1	68.05	2.33	69.55	1.089	0.111	9.811	
B-5-2	5	75.70	2.24	203.60	0.379	0.042	9.024	-22.072
B-5-3	10	95.33	1.76	66.29	0.498	0.060	8.300	
B-5-4	15	108.30	1.85	92.86	0.135	0.026	5.192	-19.816
B-5-5	16	121.70	1.69	91.89				
B-5-6	17	76.74	2.24	92.57	0.185	0.034	5.441	
B-5-7	18	99.64	2.05	93.66	0.225	0.039	5.769	-19.000
B-5-8	19	110.40	1.90	93.45	-	-	-	
B-5-9	20	127.80	1.85	98.07	-	-	-	
B-5-10	21	118.40	1.85	93.64	-	-	-	
B-5-11	22	115.70	1.66	68.81	-	-	-	
B-5-12	25	14.75	1.69	13.56	0.247	0.031	7.968	-21.006
B-5-13	30	16.22	1.63	14.49	0.264	0.031	8.516	
B-5-14	35	17.29	1.68	17.53	0.283	0.034	8.324	-20.749
C-1-1	1	84.02	2.450	133.10	0.380	0.035	10.857	
C-1-2	5	85.97	2.390	85.53	0.380	0.035	10.857	-21.537
C-1-3	7	90.13	2.420	88.79	0.489	0.049	9.980	
C-1-4	10	96.68	2.300	71.59	0.338	0.036	9.389	-20.324
C-1-5	11	106.80	1.643	66.53	-	-	-	
C-1-6	12	112.90	1.575	68.96	-	-	-	
C-1-7	13	144.10	0.858	74.78	-	-	-	
C-1-8	14	136.70	1.015	76.14	-	-	-	
C-1-9	15	73.13	1.550	89.53	-	-	-	
C-1-10	16	93.74	1.750	70.42	0.174	0.034	5.103	-18.055
C-1-11	17	139.20	1.498	77.78	-	-	-	
C-1-12	18	156.20	0.639	56.87	-	-	-	
C-1-13	19	126.40	1.395	71.67	-	-	-	
C-1-14	20	131.10	1.211	74.10	0.177	0.031	5.710	
C-1-15	21	129.50	1.381	92.18	-	-	-	
C-1-16	22	135.00	1.268	70.27	-	-	-	
C-1-17	23	125.10	1.422	71.71	-	-	-	
C-1-18	24	117.00	1.327	61.80	-	-	-	
C-1-19	25	15.26	1.650	17.91	0.259	0.036	7.262	-19.616
C-1-20	30	17.86	1.690	22.45	0.257	0.032	8.038	
C-1-21	35	17.00	1.610	16.41	0.179	0.022	8.126	-21.186
C-1-22	40	18.55	1.650	17.82	0.171	0.021	8.006	
C-1-23	45	17.38	1.600	16.26	0.205	0.028	7.398	-20.413
C-1-24	50	19.02	1.630	18.10	0.178	0.022	7.954	
C-3-1	5	112.70	2.22	123.80	0.282	0.031	9.097	-22.816
C-3-2	10	115.50	2.29	90.03	0.202	0.023	8.783	-22.095
C-3-3	15	111.90	2.15	92.91	-	-	-	
C-3-4	16	116.10	1.409	82.66	-	-	-	
C-3-5	17	131.50	1.568	71.98	-	-	-	
C-3-6	18	151.90	0.920	75.56	-	-	-	
C-3-7	19	157.40	0.721	74.94	-	-	-	
C-3-8	20	152.40	0.825	75.46	0.194	0.031	6.258	-18.606
C-3-9	21	158.50	0.686	71.14	-	-	-	
C-3-10	22	150.80	1.018	86.82	-	-	-	
C-3-11	25	12.97	1.620	11.09	0.232	0.025	9.280	-22.207

Sample ID	Avg. Depth	Mean grain size (µm)	Sorting (φ)	Std. Dev. (µm)	TOC (%)	TN (%)	TOC/TN	$\delta^{13}C$ (‰)
C-3-12	30	13.14	1.670	11.23	0.242	0.026	9.308	
C-3-13	35	14.25	1.650	13.27	0.288	0.031	9.290	-21.171
C-5-1	1	90.35	2.06	127.70	0.389	0.042	9.262	-22.828
C-5-2	5	100.20	1.83	68.30	0.277	0.030	9.233	
C-5-3	8	135.10	1.35	72.76	-	-	-	
C-5-4	9	137.60	1.17	83.86	-	-	-	
C-5-5	10	138.00	1.06	76.39	0.210	0.033	6.364	-20.060
C-5-6	11	145.40	1.02	83.97	-	-	-	
C-5-7	12	28.24	2.15	40.61	0.288	0.030	9.600	-20.544
C-5-8	15	13.71	1.65	12.71	0.310	0.039	7.949	
C-5-9	20	13.10	1.64	11.75	0.264	0.032	8.250	-20.541
C-7-1	1	59.31	2.35	91.76	0.957	0.111	8.622	-21.473
C-7-2	5	84.15	2.20	98.52	0.753	0.090	8.367	
C-7-3	6	123.00	1.13	57.35	0.461	0.070	6.586	-21.037
C-7-4	7	46.45	2.05	55.84	0.329	0.047	7.000	
C-7-5	8	34.01	1.66	47.70	0.318	0.047	6.766	-21.035
C-7-6	9	20.21	1.69	23.76	0.318	0.040	7.950	
C-7-7	15	18.47	1.68	18.39	0.218	0.027	8.074	-21.203
C-7-8	20	23.47	1.65	29.63	0.197	0.025	7.880	
BS-1	-	159.50	0.42	46.87	-	-	-	
BS-1L	-	161.30		48.94	-	-	-	
BS-2	-	221.60	0.96	137.60	-	-	-	
BS-2L	-	243.60		147.00	-	-	-	
BS-3L	-	185.70	0.72	118.40	-	-	-	
BS-3	-	183.00		108.30	-	-	-	

Appendix II A: Supplementary results of diatom analysis for Chapter 3

Diatoms count in sedimentary core D-1-5 and B-2-3 with species and ecological groups of Dhigholia and Batiaghata site.

Dhigholia (Core D-1-5)

Sl. No.	Species	**Ecology**	D-1/L-5-2-0	D-1/L-5-2-4	D-1/L-5-2-8	D-1/L-5-2-13	D-1/L-5-2-16	D-1/L-5-2-19	D-1/L-5-2-22	D-1/L-5-2-25	D-1/L-5-1-0	D-1/L-5-1-4	D-1/L-5-1-6	D-1/L-5-1-9	D-1/L-5-1-12	D-1/L-5-1-16	D-1/L-5-1-18	D-1/L-5-1-23
	Log Depth (cm)		**6**	**14**	**22**	**29**	**37**	**55**	**60**	**68**	**92**	**104**	**110**	**119**	**127**	**135**	**140**	**150**
1	*Pinnularia lagerstedtii*	F	3	1	3	4	2	2	0	0	0	0	0	-	0	1	-	-
2	*Nitzschia angustata*	F	7	5	3	5	11	5	4	0	2	1	2	-	2	1	-	-
3	*Nitzschia perminuta*	F	6	7	1	3	8	3	4	3	1	2		-	2	1	-	-
4	*Achnanthes lanceolate*	F	4	3	3	4	4	0	0	1	1	1	0	-	0	1	-	-
5	*Gomphonema exiguum*	F	2	4	2	4	3	8	0	0	3	2	2	-	0	0	-	-
6	*Epithemia sorex*	F	6	7	5	5	7	4	3	3	0	0	1	-	0	0	-	-
7	*Fragilaria construens*	F	0	3	3	8	0	0	5	0	2	0	2	-	0	1	-	-
8	*Aulacoseira granulata*	F	5	7	2	3	3	1	0	0	0	0	0	-	1	0	-	-
9	*Pinnularia lagerstedtii*	F	3	3	1	0	0	0	0	0	0	0	1	-	0	0	-	-
10	*Diploneis smithii*	B	1	0	1	2	4	3	6	1	4	3	5	-	4	3	-	-
11	*Nitzschia frustulum*	B	3	1	1	4	0	0	7	2	2	2	3	-	2	1	-	-
12	*Amphora salina*	B	0	1	1	4	2	2	2	0	3	3	1	-	5	2	-	-
13	*Thalassionema nitzschioides*	M	1	0	0	0	0	0	3	1	2	3	5	-	3	3	-	-
14	*Tabularia fasciculata*	M	0	0	0	0	0	0	0	1	1	2	3	-	2	1	-	-
15	*Rhopalodia gibba*	M	0	0	0	0	0	0	5	1	2	2	3	-	3	3	-	-

F=Freshwater, B=Brackish, M=Marine

Batiaghata (Core B-1-3)

Sl. No.	Species	Ecology	B-2/L-3/3	B-2/L-3/13	B-2/L-3/23	B-2/L-3/33	B-2/L-3/43	B-2/L-3/53	B-2/L-3/63	B-2/L-3/73	B-2/L-3/83	B-2/L-3/93	B-2/L-3/103	B-2/L-3/113	B-2/L-3/123	B-2/L-3/133	B-2/L-3/143	B-2/L-3/153	B-2/L-3/163	B-2/L-3/173	B-2/L-3/183	B-2/L-3/193
	Log Depth (cm)		5	13	23	33	43	53	63	73	83	93	103	113	123	133	143	153	163	173	183	193
1	*Cyclotella caspia*	M	0	2	0	2	0	1	0	1	2	0	0	0	0	0	1	0	0	0	0	1
2	*Coscinodiscus radiatus*	M	2	2	2	10	3	3	4	4	10	3	2	2	6	4	1	3	2	2	2	3
3	*Nitzschia compressa*	M	2	4	3	10	2	2	3	5	4	2	2	1	2	3	2	2	1	4	1	5
4	*Parlia sulcata*	M	2	3	3	7	2	5	3	5	8	2	1	2	6	4	3	5	2	4	5	5
5	*Probicia barboi*	M	0	0	0	1	1	0	1	1	0	1	0	1	2	2	0	2	2	1	1	0
6	*Rhizosolenia* Sp	M	1	0	0	2	1	1	1	0	0	1	0	1	4	2	2	2	1	2	1	1
7	*Nitzschia constricta*	M	2	1	1	1	1	2	0	2	2	1	1	0	1	1	2	0	2	0	1	2
8	*Thalassiosira oestrupiihasle*	M	1	0	2	2	0	0	2	1	1	1	0	0	1	1	1	0	0	0	0	1
9	*Thalassiosira eccentricus*	M	3	2	4	9	3	2	2	3	5	1	2	3	9	6	3	4	2	4	2	5
10	*Actinocyclus normanii*	B	1	2	2	2	1	1	1	1	1	2	0	0	2	3	0	1	0	1	2	2
11	*Amphora holsatica*	B	1	2	2	5	1	1	2	3	3	1	2	2	6	7	4	3	1	3	2	3
12	*Cyclotella stylorum* Brightwell mutica	B	3	2	3	6	3	1	3	5	8	2	1	2	8	9	4	6	2	2	3	3
13	*Cylotella atomus*	B	0	1	1	3	1	1	1	1	0	2	0	1	4	2	2	1	1	1	1	2
14	*Diplonesis smiththii*	B	2	2	2	4	3	2	4	4	6	2	2	1	3	11	4	6	3	4	2	5
15	*Fragilaria brevistrata*	B	1	0	0	1	0	1	1	0	1	2	2	1	2	1	2	1	1	3	0	1
16	*Navicula cocconeiformis*	B	0	1	1	1	1	1	0	1	1	3	1	1	2	3	1	2	1	0	1	1
17	*Navicula mutica*	B	2	1	4	6	0	2	2	3	3	1	2	3	9	7	5	7	4	3	4	4
18	*Thalassiosira bramaputrae*	B	2	1	1	3	1	1	2	2	4	2	2	2	8	8	4	5	3	4	3	5
19	*Aulocosira granulata*	F	3	2	0	3	2	2	2	2	3	1	2	2	7	9	4	4	2	4	2	4
20	*Aulocosira ambigua*	F	2	0	1	1	1	1	1	1	1	3	0	0	3	4	2	1	0	1	2	2
21	*Eunotia* Spp	F	2	1	2	2	1	3	2	2	5	1	4	3	9	23	4	4	1	2	3	2
22	*Gomphonema gracile*	F	2	2	2	4	1	1	2	2	6	3	5	3	12	16	4	5	1	3	2	3
23	*Melosira ambigas* raft	F	0	0	1	1	1	2	0	0	1	1	1	2	2	4	1	1	2	2	0	2
24	*Nitzschia furstullum*	F	0	1	0	2	0	0	1	1	2	3	1	1	4	3	2	2	2	1	2	3
25	*Navicula elginesis*	F	1	2	1	3	1	1	2	3	9	4	3	5	12	3	4	4	4	4	4	6

F=Freshwater, B=Brackish, M=Marine

Appendix II B: Supplementary results of diatom analysis for Chapter 4

Diatoms count in surface and beach sediment with species and ecological groups at Haringhata coastal region of Barguna districts.

Name/sample	Ecology	Site-1	Site-2	Site-3	Beach Sand
Achnanthes delicatula (Kütz.) Grun.	BM	1	0	0	4
Amphora normannii Rabenhorst	F	0	0	0	1
Aulacoseira granulata (Ehr.) Simonsen	F	0	0	1	0
Aulacoseira subarcta (O.Müller) Haworth	F	0	0	0	2
Bacterosira fragilis (Gran) Gran	M	2	0	0	0
Caloneis permagna (Bailey) Cleve	B	0	1	0	0
Campylodiscus sp. 1	B	0	0	1	1
Cyclotella caspia	B	0	1	0	0
Cyclotella meneghiniana Kütz.	BF	1	0	0	0
Cyclotella stylorum Brightwell	M	3	0	1	0
Cyclotella striata (Kütz.) Grun.	BM	5	7	2	2
Cymbella perpusilla A. Cleve	F	0	0	0	1
Cymbella pusilla Grun.	F	2	0	4	0
Cymbella sinuata Greg.	F	0	0	0	1
Cymbella silesiaca Bleisch.	F	0	0	0	1
Delphineis surirella (Eer.) Andrews	M	1	1	0	1
Diploneis smithii var. rhombica Mereschkowsky	M	0	0	0	1
Frafilaria brevistriata Gurn.	BF	0	3	0	0
Frafilaria fasciculata	BM	2	1	0	3
Fragilaria zeilleri Héribaud var. zeilleri	F	1	0	0	0
Gomphonema minutum (C. Agardh) C. Agardh	F	0	0	0	2
Gomphonema parvulum Kütz.	F	0	0	0	1
Gyrosigma acuminatum (Kütz.) Rabenhorst	F	0	2	0	0
Hemidiscus cuneiformis	M	0	1	0	2
Hemidiscus ovalis Lohman	F	1	0	1	1
Navicula clementis Grun.	FB	0	0	0	4
Navicula cryptotenella	F	1	0	10	57
Navicula fossalis Krasske var. fossalis	F	0	0	0	1
Navicula halophila (Grun.) Cleve	BM	0	0	3	0
Navicula meniscus Schumann	B	0	0	0	1
Navicula modica Hust.	F	0	0	0	1
Navicula paucivisitata Patrick	F	0	2	0	0
Navicula perminuta Grun.	B	0	0	5	0
Navicula phyllepta Kütz.	B	1	0	0	2
Navicula pseudoscutiformis Hust.	F	0	0	0	1
Navicula pygmaea	BF	0	0	4	2
Navicula lapidosa Krasske	F	0	0	0	6
Navicula reinhardtii (Grun.) Grun.	F	0	1	1	0
Navicula schoenfeldii Hust.	F	0	0	1	0
Navicula subminuscula Manguin	F	0	0	0	2
Nitzschia clausii	BF	0	2	1	8
Nitzschia constricta	M	0	0	0	1
Nitzschia epithemoides var. disputata (Carter) Lange-Bertalot	B	0	0	0	2
Nitzschia fonticola Grun.	F	0	0	0	2
Nitzschia granulata	B	1	0	0	0

Name/sample	Ecology	Site-1	Site-2	Site-3	Beach Sand
Nitzschia hantzschiana Rabenhorst	F	0	0	1	1
Nitzschia littoralis Grun.	B	1	0	2	1
Nitzscia recta	F	0	2	3	6
Paralia sulcata (Eer.) Cleve	M	1	0	0	0
Raphoneis amphicerous Eer.	M	0	2	0	0
Raphoneis cf. *rhomboides* Hendrey	M	1	0	0	1
Rhopalodia gibberula (Eer.) O. Müller	BF	0	0	0	2
Stauroneis borrichii (Peterson) Lund.	F	1	0	0	0
Stephanodiscus hiagare Eer.	F	1	0	0	0
Thalassiosira excentrica (Eer.) Cleve	M	1	0	0	0
Thalassiosira miocenica Schrader	M	1	0	0	0
Thalassiosira oestrupii	M	5	3	0	1
*Thalassiosira trifult*a Fryxell	M	0	0	0	1
Thalassiosira sp. 1	BF	0	0	0	1

F=Freshwater, BF=Brackish-Freshwater, B=Brackish, BM=Brackish-Marine, M=Marine

Appendix II C: Supplementary results of diatom analysis for Chapter 5

Diatoms count in sedimentary core B-1 at Kuakata coast, Patuakhali with species and ecological groups.

Name/sample	Depth in cm / Ecology	B1 2	B1 4	B1 6	B1 17	B1 19	B1 20	B1 21
		5	8	10	21	30	35	40
Achnanthes delicatula (Kütz.) Grun.	BM	0	0	0	1	0	0	0
Amphora normannii Rabenhorst	F	0	0	0	1	0	0	0
Aulacoseira granulata (Ehr.) Simonsen	F	0	1	1	0	0	0	0
Caloneis permagna (Bailey) Cleve.	B	0	0	0	0	1	1	0
Campylodiscus sp. 1		0	0	0	1	0	0	0
Cyclotella caspia	B					1	1	
Cyclotella meneghiniana Kütz.	BF	3	1	2	0	0	0	0
Cyclotella striata (Kütz.) Grun.	BM	0	0	0	0	2	4	0
Cymbella pusilla Grun.	F	0	1	0	0	0	0	0
Cymbella silesiaca Bleisch	F	0	0	0	1			
Delphineis surirella (Eer.) Andrews	M	0	0	2	2	1	3	2
Eunotia subarcuatoides Norpel & Lange-Bertalot	F	4	3	3	0	0	0	0
Frafilaria brevistriata Gurn.	BF	1	0	0	0	3	4	4
Frafilaria fasciculata	BM	1	0	0	0	2		8
Gomphonema clavatum (Eer.)	F	14	0	0	0	0	3	
Gomphonema gracile Ehr.	F	2	0	0	0	0	0	0
Gomphonema minutum (C. Agardh) C. Agardh	F	0	0	2	0	0	0	2
Gomphonema parvulum Kütz.	F	12	0	1	0	0	2	1
Gyrosigma acuminatum (Kütz.) Rabenhorst	F	0	0	0	0	2	2	0
Hemidiscus cuneiformis	M	0	0	0	1	1	1	0
Hemidiscus ovalis Lohman	F	0	0	1	0	0	0	1
Navicula absoluta Hust.	F	1	0	0	0	0	0	0
Navicula agrestis Hust.	F	1	0	0	0	0	0	0
Navicula cryptotenella	F	4	2	11	14	1	3	8
Navicula eidrigiana Carter	B	0	1	0	0	0	0	0
Navicula halophila (Grun.) Cleve	BM	6	3	0	0	0	0	0
Navicula ingrata Krasske	M	1	4	0	4	0	0	0
Navicula paucivisitata Patrick	F	0	0	0	0	2	2	
Navicula phyllepta Kütz.	B	62	7		2	0	0	0
Navicula laevissima Kütz. var. laevissima	F	10	6	0	0	0	0	0
Navicula lapidosa Krasske	F	3	3	2	3	1		2
Navicula reinhardtii (Grun.) Grun.	F	0	0	0	0	1	1	
Navicula subminuscula Manguin	F	36	7	0	2	0	2	0
Navicula weinzierlii Schimanski	F	9	0	0	0	0	0	0

Name/sample	Depth in cm / Ecology	B1 2	B1 4	B1 6	B1 17	B1 19	B1 20	B1 21
		5	8	10	21	30	35	40
Neidium alpinum Hust.	F	1	0	0	0	0	0	0
Nitzschia clausii	BF	6	0	4	3	2	2	4
Nitzschia constricta	M	9	0	1	3	2		1
Nitzschia epithemoides var. disputata (Carter) Lange-Bertalot	B	0	0	2		1	0	2
Nitzschia fonticola Grun.	F	2	0	1	0	0	0	1
Nitzschia hantzschiana Rabenhorst	F	2	0	0	0	0	0	0
Nitzschia littoralis Grun.	B	0	0	1	0	0	0	1
Nitzscia recta	F	0	0	0	0	0	2	0
Pinnularia subcapitata Greg.	F	2	5	0	0	0	0	0
Pinnularia subrostrata (A. Cleve) Cleve-Euler.	F	3	0	0	0	1	0	0
Pinnularia viridis (Nitzschi) Eer.	F	1	3	0	0	0	2	0
Raphoneis amphicerous Eer.	M	0	0	0	0	2	2	0
Raphoneis cf. *rhomboides* Hendrey	M	1	2	2	4	2	2	2
Rhopalodia gibberula (Ehrenberg O. Müller	BF	0	0	0	2	0	0	0
Stauroneis anceps (Eer.)	F	1	0	0	0	0	0	0
Stauroneis tackei (Hust.) Krammer & Lange-Bertalot	F	2	0	0	0	0	0	0
Thalassiosira oestrupii	M	0	0	0	0	3	3	0
Thalassiosira bramaputrae	BF	0	0	0	0	2	0	3

F=Freshwater, BF=Brackish-Freshwater, B=Brackish, BM=Brackish-Marine, M=Marine